

Submillimetre Observations of the Subaru Deep Field

by

Kristen Erin Kathryn Coppin

B.Sc. (Physics and Astronomy) University of Victoria, 2000

A THESIS SUBMITTED IN PARTIAL FULFILMENT OF
THE REQUIREMENTS FOR THE DEGREE OF

MASTER OF SCIENCE

in

THE FACULTY OF GRADUATE STUDIES

(Department of Physics and Astronomy)

We accept this thesis as conforming
to the required standard

THE UNIVERSITY OF BRITISH COLUMBIA

October 10, 2003

© Kristen Erin Kathryn Coppin, 2003

In presenting this thesis in partial fulfilment of the requirements for an advanced degree at the University of British Columbia, I agree that the Library shall make it freely available for reference and study. I further agree that permission for extensive copying of this thesis for scholarly purposes may be granted by the head of my department or by his or her representatives. It is understood that copying or publication of this thesis for financial gain shall not be allowed without my written permission.

Department of Physics and Astronomy

The University Of British Columbia
Vancouver, Canada

Date Oct. 10/03

ABSTRACT

We have measured the submillimetre wavelength continuum emission from the Subaru Deep Field (SDF) at 450 and 850 μm with the Submillimetre Common-User Bolometer Array (SCUBA) detector on the James Clerk Maxwell Telescope (JCMT). The SDF is as deep a near-IR image as is available and contains four ‘hyper extremely red objects’ (HEROs). These data have allowed us to test the connection between ‘extremely red objects’ (EROs) found in IR surveys and the population of bright submillimetre sources found with SCUBA. This is an important building block in our understanding of the star formation history of the universe. We examine the entire submillimetre map of the SDF region and perform correlation analyses of a K' -selected catalogue of galaxies in the SDF with our submillimetre SDF map. We find that there is no clear correlation between the near-Infrared positions and submillimetre flux. We also present upper limits to the fluxes of the four HEROs, or a weak measurement of the average flux for the four of them. Our data are consistent with the HEROs being Arp220-like objects out to $z \simeq 1.6$. However, they would need to be one and a half times as luminous as Arp220 and extinguished in the J -band by about 1 magnitude; a plausible scenario since only modest adjustments are made to Arp220’s luminosity and dust content.

CONTENTS

Abstract	ii
Contents	iii
List of Tables	v
List of Figures	vi
1 Introduction	1
1.1 Galaxy Formation and Evolution	1
1.2 Submillimetre Galaxies	2
1.2.1 The Origin of Submillimetre Emission	2
1.2.2 Inhabitants of the High-Redshift Universe	3
1.2.3 Submillimetre Emission as a High-Redshift Probe	3
1.2.4 EROS	7
1.2.5 Hyper-Extremely Red Objects	8
1.3 The Subaru Deep Field	10
1.4 Guide to This Thesis	15
2 The Instrument and Data	17
2.1 The JCMT and SCUBA	17
2.1.1 Observing Modes	18
2.2 Observations	21
2.2.1 Added Noise in the 2003 Data	24
2.3 Data Reduction	30
2.3.1 Preliminary Reduction with SURF	30

2.3.2	Making the Maps	31
2.3.3	Calibration	34
2.3.4	Flux Measurements	35
3	HEROs	40
3.1	Cirrus Contribution	40
3.2	HERO IR Colours and 850 μm Fluxes	41
3.3	Using Arp220 as a Template	41
3.4	Using a NGC3938 as a Template	51
3.5	Results	51
3.6	Are the Models Feasible?	51
3.6.1	Number Counts of Submillimetre Sources	54
3.6.2	Could the HEROs be Starburst Galaxies?	54
3.6.3	Could the HEROs be Normal Spiral Galaxies?	61
4	SDF Sources	68
4.1	Correlating the IR Galaxies with the Submillimetre Data	68
4.1.1	Detections	91
5	Conclusions	96
5.1	Future Work	98
	Bibliography	99

LIST OF TABLES

1.1	Summary of IR information on the HEROs	13
2.1	Summary of SCUBA observations	23
2.2	Summary of Flux Conversion Factors	36
2.3	Summary of SCUBA data for the HEROs with upper limit flux estimates and photometric redshifts	39
3.1	Submillimetre sources with red IR colours and known redshifts	49
3.2	Summary of SCUBA data for the HEROs with upper limit flux estimates and photometric redshifts	53
4.1	Detected sources	95

LIST OF FIGURES

1.1	The extragalactic background	4
1.2	Negative K-correction	6
1.3	$I - K_{AB}$ versus K_{AB}	9
1.4	The Subaru Deep Field K' -band image	11
1.5	J and K' -band images of the HEROs	12
1.6	The $850\ \mu\text{m}$ cumulative source counts	16
2.1	SCUBA wideband filter profiles	19
2.2	The SCUBA bolometer arrays	20
2.3	FFTs of jiggle map data	25
2.4	FFT of the average of 2003 jiggle map data	27
2.5	Standard deviation of 10 integrations for 64 positions of the central bolometer	28
2.6	Contour plots of the standard deviation of 10 integrations for 64 positions of the central bolometer	29
2.7	Chopping strategy for photometry observations of the SDF	33
2.8	$850\ \mu\text{m}$ SDF SNR map	37
2.9	$450\ \mu\text{m}$ SDF SNR map	38
3.1	Is there a colour-flux correlation for the HEROs?	42
3.2	SED of Arp220	44
3.3	Comparison of 3 different luminosity SEDs	45
3.4	Effective wavelengths and relative extinction values from Schlegel, Finkbeiner & Davis [53]	46
3.5	Creating an extinction law	47
3.6	Testing our model against sources with known redshifts	50

3.7	SED of NGC3938	52
3.8	Expected 850 μm versus redshift using Arp220	55
3.9	K' -band brightness versus redshift using Arp220	56
3.10	Required J and K' -band dust extinction using Arp220	58
3.11	The Totani et al. [63] model of a typical elliptical galaxy	60
3.12	Model of HR10 based on an Arp220 SED	62
3.13	Expected 850 μm versus redshift using NGC3938	63
3.14	K' -band brightness versus redshift using NGC3938	64
3.15	Required J and K' -band dust extinction using NGC3938	65
4.1	Histogram of number of pixels at each flux level for the 850 μm map	69
4.2	The difference of the flux bins and the flux bins reflected about 0 mJy for the 850 μm map	70
4.3	Histogram of number of pixels at each flux level for the 450 μm map	71
4.4	The difference of the flux bins and the flux bins reflected about 0 mJy for the 450 μm map	72
4.5	Histogram of the mean of the 20 brightest K' -band objects per redshift bin	74
4.6	Histogram of observed average 850 μm flux per redshift bin	75
4.7	Histogram of observed average 450 μm flux per redshift bin	76
4.8	Distribution of correlation coefficients obtained from a set of Monte Carlo simulations of stacked 850 μm flux in redshift bins	78
4.9	Frequency of obtaining a certain correlation coefficient from a set of Monte Carlo simulations of stacked 850 μm flux in redshift bins	79
4.10	Distribution of correlation coefficients obtained from a set of Monte Carlo simulations of stacked 450 μm flux in redshift bins	80
4.11	Frequency of obtaining a certain correlation coefficient from a set of Monte Carlo simulations of stacked 450 μm flux in redshift bins	81
4.12	Average 850 μm flux per redshift bin with an equal number of objects per bin	83

4.13	A plot of observed average $450\ \mu\text{m}$ flux per redshift bin with an equal number of objects per bin	84
4.14	Distribution of correlation coefficients obtained from a set of Monte Carlo simulations of stacked $850\ \mu\text{m}$ flux with an equal number of objects per redshift bin	85
4.15	Frequency of obtaining a certain correlation coefficient from a set of Monte Carlo simulations of stacked $850\ \mu\text{m}$ flux with an equal number of objects per redshift bin	86
4.16	Distribution of correlation coefficients obtained from a set of Monte Carlo simulations of stacked $450\ \mu\text{m}$ flux with an equal number of objects per redshift bin	87
4.17	Frequency of obtaining a certain correlation coefficient from a set of Monte Carlo simulations of stacked $450\ \mu\text{m}$ flux with an equal number of objects per redshift bin	88
4.18	Stacked $850\ \mu\text{m}$ flux measured in K magnitude bins	89
4.19	Stacked $450\ \mu\text{m}$ flux measured in K magnitude bins	90
4.20	Scatter-plots of $850\ \mu\text{m}$ flux for V -band detected objects	92
4.21	Stacked $850\ \mu\text{m}$ flux measured in M_V bins	93
4.22	Stacked $850\ \mu\text{m}$ flux measured in M_V bins for objects with $z > 2$ and $z > 4$	94

Acknowledgements

I would like to thank my research supervisor, Dr. Mark Halpern, for his expertise, guidance, patience, enthusiasm and financial support through NSERC. Additional funding was received from the National Research Council of Canada and was used for trips to the JCMT to collect data for this project. Much thanks also goes out to the staff of the JCMT for their assistance with the SCUBA observations. The James Clerk Maxwell Telescope is operated on behalf of the Particle Physics and Astronomy Research Council of the United Kingdom, the Netherlands Organisation for Scientific Research, and the National Research Council of Canada. This research has made use of the NASA/IPAC Extragalactic Database (NED) which is operated by the Jet Propulsion Laboratory, California Institute of Technology, under contract with the National Aeronautics and Space Administration. We acknowledge the use of NASA's *SkyView* facility (<http://skyview.gsfc.nasa.gov>) located at NASA Goddard Space Flight Center. In addition, Guillaine Lagache supplied her group's starburst and normal galaxy templates and an unpublished version of a paper describing these galaxy templates which was much appreciated. I would also like to thank Anna Sajina for help using the templates and for getting me started with IDL. My gratitude goes out to Colin Borys who helped me with using his map-making codes and for generally useful advice. Douglas Scott and James Dunlop also provided many useful suggestions and comments about the work contained in this thesis.

CHAPTER 1

INTRODUCTION

1.1 Galaxy Formation and Evolution

Two fundamental unsolved problems in modern cosmology are: *how and when did the first galaxies form; and how long did their initial starbursts last?* There are mainly two theories depicting how galaxies may have formed: the monolithic collapse and hierarchical merging scenarios. The current consensus is that massive galaxies formed via hierarchical structure formation, but there is possible contrary evidence suggesting that a monolithic collapse scenario may still play a role in some instances. Based on the motions of old stars in our Galaxy, Eggen, Lynden-Bell & Sandage [27] conceived the monolithic collapse scenario as a theory of galaxy formation, involving a single rapid collapse of stars at high redshift, producing a violent and short-duration burst of star-formation followed by a quiescent evolution of the stellar population. This theory was questioned by Searle & Zinn [54] as new and better data became available and they suggested that star formation in our Galaxy was a more prolonged chaotic process. New theories were subsequently developed (see Davis et al. [16]) describing galaxy formation as a “bottom-up” process, i.e. hierarchical merging, or the gradual formation of a galaxy by the merging of smaller collections of stars at moderate redshifts of $z < 1.5$ producing moderate and continuous star-formation (e.g. White & Frenk [66], Kauffmann [44]). We see evidence of hierarchical merging as our neighbouring satellite, the Sagittarius dwarf galaxy, is being tidally disrupted by our Galaxy’s gravitational field (see Ibata, Gilmore & Irwin [39]). But older stellar populations of galactic spheroids seem to be better explained by a monolithic collapse scenario. So we see evidence of both processes throughout the history of the Universe but we do not know how much each process plays into the entire galaxy formation picture.

1.2 Submillimetre Galaxies

Very luminous high-redshift galaxies have recently been discovered at submillimetre wavelengths and may be significant players in deducing the history of galaxy formation and evolution. Far-Infrared and submillimetre galaxies are responsible for approximately 2/3 of the total power output of all known galaxies and they are excellent tracers of massive regions of star-formation at high redshifts (Gispert, Lagache & Puget [33]). Most of the star formation history of the Universe is “hidden” from optical sight, but remains transparent in the Infrared (IR) and submillimetre regimes. Careful submillimetre surveys of distant galaxies should be able to shed some light on the relative importance of each formation process since submillimetre emission can indicate galaxies undergoing heightened rates of star-formation. (Blain et al. [3]).

1.2.1 The Origin of Submillimetre Emission

There are two different mechanisms responsible for submillimetre emission from galaxies: continuum thermal emission and line emission. Supernovae are thought to be the most likely dominant mechanism of dust production at high redshifts (Dunne et al. [25]). These micron-sized interstellar dust grains, primarily composed of silicates and polycyclic aromatic hydrocarbons (PAHs), absorb hard-UV photons from regions of intense high mass star-formation or from Active Galactic Nuclei (AGN) accretion disks and are heated to temperatures between 20–200 K. The obscuring dust grains re-radiate this absorbed radiation as thermal continuum emission, peaking in the Far-Infrared (FIR). This emission becomes visible at submillimetre wavelengths when the cosmological expansion of the Universe redshifts the FIR peak into this regime. The other mechanism involves atomic and molecular transitions in the interstellar gas resulting in line emission. Approximately 99 per cent of the power output of galaxies at submillimetre and far-IR wavelengths is produced by continuum thermal emission and the rest comes from line emission. (Blain et al. [3]).

1.2.2 Inhabitants of the High-Redshift Universe

In the 1980's, a ~ 1 Jy sensitive all-sky survey at 12, 25, 60 and $100\ \mu\text{m}$ by the Infrared Astronomical Satellite (*IRAS*), revealed a population of previously unseen optically-faint galaxies out to a redshift of $\simeq 0.3$ and that the amount dust reprocessing increases with star production and cannot be measured solely with optical or UV data (see Sanders & Mirabel [52]). After the dominant CMB emission is accounted for, about half of the remaining energy budget of the extragalactic background is contained in the Far-Infrared Background (FIRB) (see Fig. 1.1). The Infrared Space Observatory (ISO), sensitive only to the low redshift region, resolved about 10 per cent of the FIRB into discrete galaxies lying at redshifts less than about 1 (Dole et al. [20]).

The discovery of a submillimetre extragalactic background by *COBE* (COsmic Background Explorer) was an amazing find and requires the existence of far-IR emitting galaxies in the early throes of their evolution or elliptical galaxies bursting with star formation. This submillimetre background implies a strong cosmological evolution, or that early type galaxies in the distant Universe must be very different from galaxies in the local Universe which we know to be predominantly composed of relatively old stars. This progression greatly affects the star formation history, as a large part of the stars being formed are most likely hidden in dust-enshrouded galaxies, eluding optical surveys. *What are the objects responsible for producing this background emission and what is their role in galaxy formation?* The SCUBA camera on the JCMT is able to detect rest-frame far-IR radiation from high-redshift galaxies and has revealed a galaxy population with star-formation rates of $100\ M_{\odot}\text{yr}^{-1}$, similar to that expected from dusty protogalaxies (Steidel [60]). There are relatively few secure identifications and redshifts unfortunately, but most SCUBA galaxies are thought to be at redshifts greater than 1.

1.2.3 Submillimetre Emission as a High-Redshift Probe

Submillimetre emission may be used as a probe of the high-redshift Universe since it can penetrate dust, and because of another powerful effect called the negative K-correction

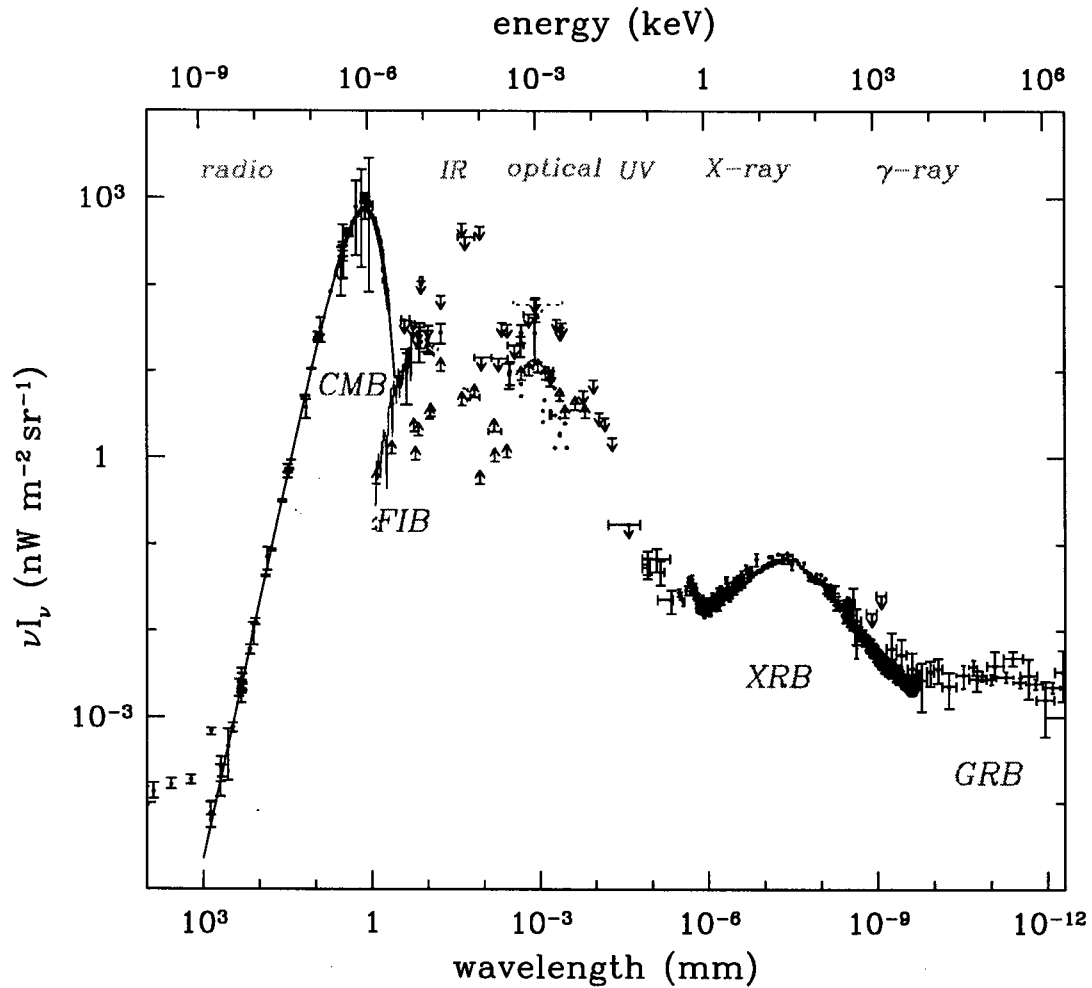


Figure 1.1: This figure depicts the energetics of the extragalactic background which is comprised of six main components: the Cosmic Microwave Background (CMB), the Cosmic Infrared Background (CIB) or Far-Infrared Background (FIB), the Near-Infrared (NIR), the Optical-UV, the X-Ray Background (XRB) and the Gamma-Ray Background (GRB). Use of this figure courtesy of Scott et al. [55].

which facilitates submillimetre observations of galaxies out to the distant reaches of the Universe. The negative K-correction is strongest for wavelengths longer than about $250 \mu\text{m}$, being the most pronounced at millimetre wavelengths as seen in Fig. 1.2, and causes a galaxy's flux density to remain about constant as it is moved to higher redshifts (between $1 \lesssim z \lesssim 10$).

Resolved submillimetre-wave observations exist only for the lowest redshift galaxies and it is usual practice to use the results of these observations as templates for galaxies of the more distant Universe (which may or may not be a reasonable assumption given the lack of understanding of high-redshift galaxies and of the feedback processes involved in star formation). *IRAS* uncovered a distinct class of extremely luminous objects of $10^{11} L_{\odot}$, dubbed Luminous Infrared Galaxies or LIRGs. Not-so-distant cousins to LIRGs, Ultra Luminous Infrared Galaxies (ULIRGs) are probably more similar to galaxies in the high-redshift world with respect to their luminosities and physical properties. ULIRGs are a small class of special objects, believed to be interacting or merging pairs of spiral galaxies. They make up less than 0.1 per cent of galaxies in the local Universe but were more important in the past (Sanders [51]). They represent the most luminous of galaxies in the local Universe with bolometric luminosities in excess of $10^{12} L_{\odot}$ and the dust emission dominated peak of their spectral energy distribution (SED) lies in the FIR region of the spectrum. This peak gets redshifted into the submillimetre regime, making submillimetre observations an ideal way to see the highest redshift dusty ULIRGs. ULIRGs have irregular morphologies and are bursting with star-formation, most likely indicating recent galaxy mergers. ULIRGs predominantly display elliptical galaxy surface brightness profiles (e.g. Zheng et al. [69]), hinting that ULIRG formation could be just the way to form elliptical galaxies at high redshifts.

Submillimetre-selected galaxies are an important piece of the galaxy formation and evolution puzzle but are difficult to study, as they are usually very faint in the complementary wavelength regimes. Limited progress has been made in determining the relationship of the submillimetre population to other high-redshift galaxy populations. Of all the classes of galaxies, Extremely Red Objects (EROs) have emerged to be one

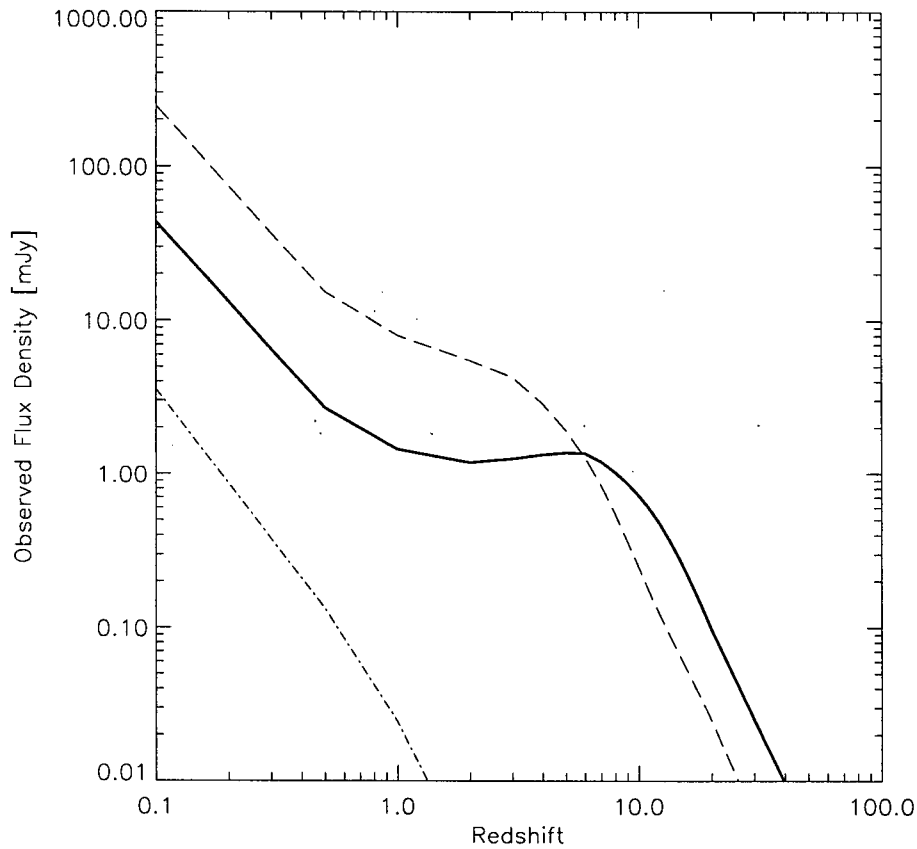


Figure 1.2: This figure depicts the effect of negative K-correction on the predicted flux density of Arp220, a dusty ULIRG galaxy, as a function of redshift. Note the powerful K-correction at submillimetre wavelengths of $850 \mu\text{m}$ (solid line) and $450 \mu\text{m}$ (dashed line), where the flux density is almost independent of redshift past $z \approx 1$. The sudden drop in flux at high redshift occurs because we begin to sample the SED on the other side of the thermal FIR peak. The K-band does not benefit from this effect and is shown for comparison (dot-dashed line).

of the most promising and important tools for studying the history of galaxy formation and star formation in the universe (Dickinson et al. [18], Yahata et al. [68]), since dusty objects at high redshifts are expected to be strongly reddened.

1.2.4 EROS

The recent development of large near-IR imaging cameras led to the discovery of a faint class of extremely red objects, or EROs. The ERO class contains objects with very red optical to near-IR colours, typically $R - K > 5$ to 6 or $I - K > 4$. Suggested explanations for the very red spectra include the possibility that they might be dusty galaxies at $z < 1$, extraordinarily high-redshift ‘ J -dropout’ galaxies, or that they are old elliptical galaxies containing low-mass cool stars seen at $z \approx 1$ or 2, passively evolving after their initial burst of star formation, and that line emission might be involved. The ERO class may very well contain several types of object. Dickinson et al. [18].

This selection criterion was originally designed to pick out old (> 1 Gyr) passively evolving elliptical galaxies at redshifts between 1 and 2. But a small fraction of all EROs selected this way seem to be very dusty ellipticals undergoing their initial burst of star formation. It is important to find the dominant population amongst the EROs since the high-redshift old ellipticals would indicate a “monolithic collapse” scenario of galaxy formation whereas the “hierarchical” scenario would be better supported by evidence of many dusty starbursts living at intermediate redshifts.

Many of the most luminous submillimetre sources discovered have been identified as convincing counterparts to EROs. For example, CUDSS14A (Gear et al. [32]), SMM J00266+1708 (Frayser et al. [31]), W-MMD11 (Chapman et al. [12]), SMM J09429+4658, and SMM J04431+0210 (Smail et al. [58]) have all been identified with EROs. These submillimetre sources have fluxes in the range of 7 to 20 mJy. Because of the high frequency with which very bright submillimetre sources are identified with EROs, Smail et al. [58] suggest that submillimetre sources comprise the majority of the reddest EROs.

Totani et al. [63] discovered four objects in the Subaru Deep Field that were even more

red than the reddest known EROs. So the UBC submillimetre group collaborated with the Subaru team and applied for time to search for these rare objects at submillimetre wavelengths, to test the conjecture that very red objects are submillimetre-bright. The search for dusty starbursts at high redshifts is a key step to unraveling the mystery of galaxy formation at early epochs.

1.2.5 Hyper-Extremely Red Objects

Among the EROs which are faintest in K -band, $K > 22$, an increasing fraction are extraordinarily red, even compared to other EROs, with $J - K > 3$ or 4. K -band sources which are very faint or undetected in optical data hold a strong possibility of being SCUBA bright. Fig. 1.3 is the near-IR colour-magnitude diagram for the CFRS (Canada-France Redshift Survey) and demonstrates that ULIRGs make up a large fraction of the reddest objects in this field. But does a redder colour necessarily guarantee that an object will be bright in the submillimetre?

Totani et al. [63] cleverly dubbed this very distinct population of galaxies Hyper-Extremely Red Objects, or HEROs, and in detailed modeling find that they are much too red to be passively evolving elliptical galaxies at $z < 2$. These objects are most likely to be either very dusty elliptical galaxies which formed at redshift $z \approx 4 - 7$ and are still undergoing rapid star formation when seen at redshift $z > 2$, or they are clean, Lyman break galaxies seen at extraordinary redshifts of $z > 10$. Red optical colours sometimes suggest that dust extinction is present, and this is precisely what submillimetre instruments can see. Knowing the submillimetre flux of these HEROs would distinguish between the galaxy formation models and could provide very valuable information for understanding when galaxies first formed and how long their initial starbursts lasted.

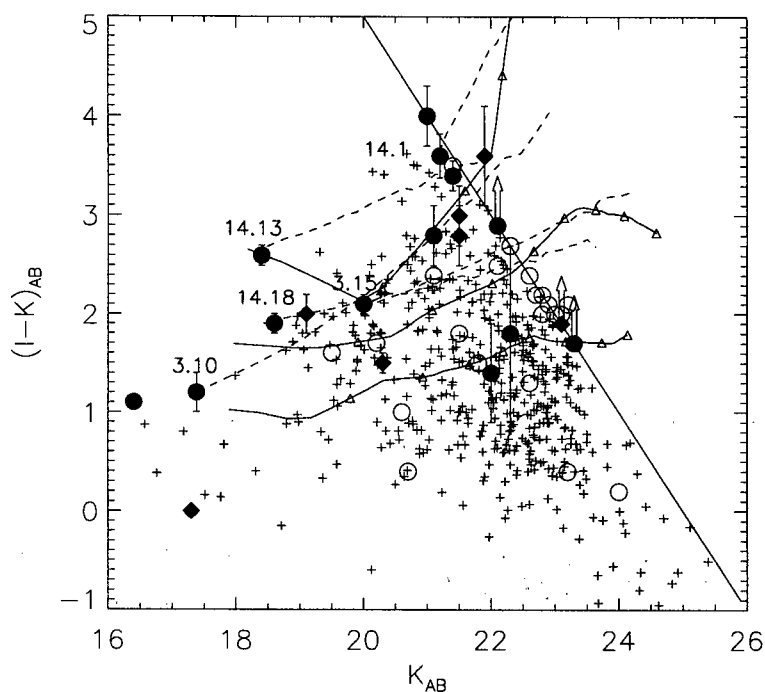


Figure 1.3: The near-IR colour-magnitude diagram for the identifications the CFRS 14h and 3h fields (see Clements et al., in preparation). The solid circles correspond to radio-detected objects, and the solid diamonds denote radio non-detections. The open circles show the best identification for the remaining objects. For comparison, the magnitudes and colours of all the galaxies in the CFHTIR CUDSS+14 image are also shown (plus signs). Not included in this plot are the possible LBG identifications (whose colors are in the grz filter system). The solid, diagonal black line denotes the I detection limit of the CFRS. The dashed lines are tracks of $I - K_{AB}$, K_{AB} with redshift for sources 14.1, 14.3, 14.18, 3.10, and 3.15. The three solid lines show the predicted colors for the three ULIRGs studied by Trentham, Kormendy & Sanders [64]. These have been scaled to $M_{K_{AB}} = 24.4$ (approximately $M^* - 2$). The tracks begin at $z = 0.5$ and are marked (small triangles) every 0.5 step in redshift. This plot illustrates that ULIRGs comprise most of the reddest populations. Use of this plot and caption courtesy of Webb et al. [65].

1.3 The Subaru Deep Field

The Subaru Telescope, atop Mauna Kea, has been used to produce deep images in J -band $\lambda = 1.16 - 1.32 \mu\text{m}$ and in K' -band¹ $\lambda = 1.96 - 2.30 \mu\text{m}$ of a ‘blank’ $2 \text{ arcmin} \times 2 \text{ arcmin}$ field near the north Galactic pole (Maihara et al. [46]) (see Fig. 1.4). The Subaru Deep Field (SDF) is a blank survey region and was chosen according to the following criteria:

1. to be in a different location than the Hubble Deep Field (HDF) since the Universe may have different characteristics depending on the direction you look (the HDF also has a higher airmass than the SDF from Mauna Kea),
2. to have a reference star nearby for future adaptive optics (AO) observations,
3. to have low Galactic HI column density, no close-by stars (except for the AO guide star), galaxies or clusters of galaxies.

Subaru’s large aperture and $\approx 0.3 \text{ arcsec}$ seeing have allowed extremely deep images which rival any other images at these wavelengths ($5\sigma = 25.1$ and 23.5 in J and K' respectively). These images are providing us with vital information for understanding physical conditions during the earliest epochs of galaxy formation, just as studying the Hubble Deep Field has done². Near-IR observations measure the starlight directly from older stellar populations or redshifted optical-UV emission. The K -band is about 10 times less obscured than optical bands and is therefore a good measure of intrinsic luminosity. So deep near-IR imaging has the potential to reveal a significant population of galaxies at high redshifts.

Among the ~ 350 galaxies detected in the K' -band ($K' < 23.5$) in the SDF, there are four HEROs whose K' magnitudes and $J - K'$ colours are derived in Maihara et al. [46] and are given in Table 1.1. This sample of objects has a weighted average K' magnitude and $J - K'$ colour of 21.57 and 2.99, respectively.

¹The K' -band is centred at a wavelength of $2.13 \mu\text{m}$ compared to the K -band being centred at a wavelength of $2.2 \mu\text{m}$.

²The Hubble Deep Field (HDF) revealed that faint, irregular and smaller galaxies are more abundant, perhaps a characteristic of the infant high-redshift Universe (Ferguson, Dickinson & Williams [29]).

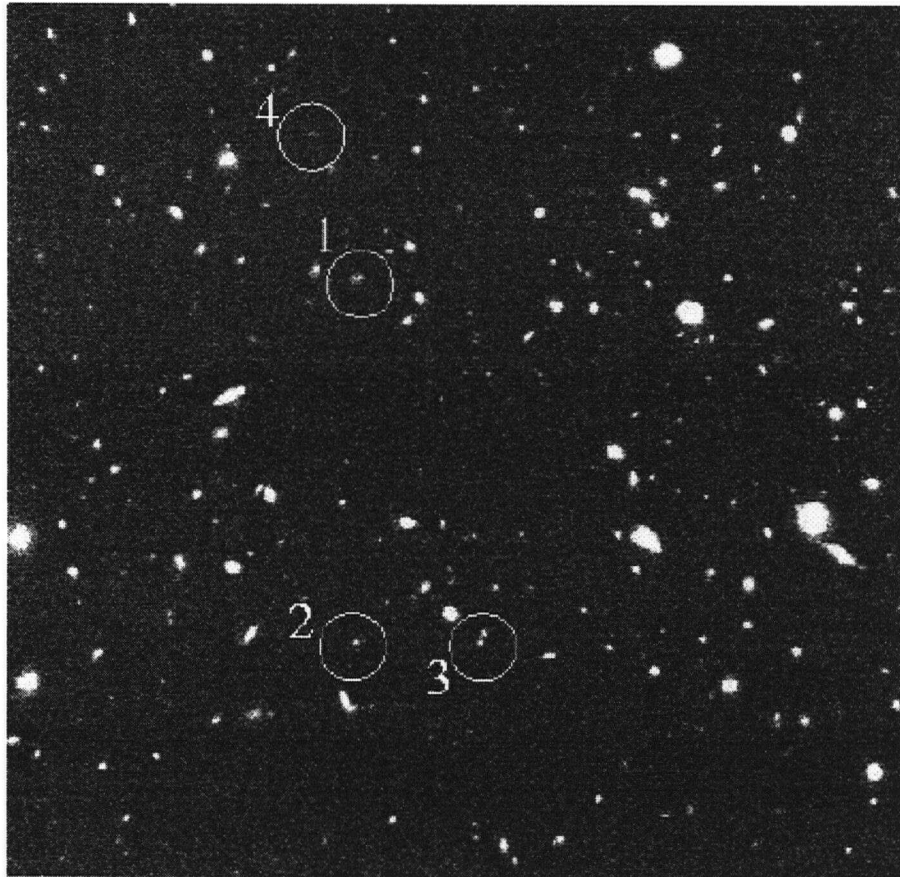


Figure 1.4: The Subaru Deep Field K' -band image. Circles are drawn around the four HEROs shown in more detail in Fig. 1.5. The numbers simply indicate the order of presentation in Fig. 1.5. The circles, drawn to guide the eye, are roughly 10 arcsec in diameter, $\simeq 2/3$ of the SCUBA $850\ \mu\text{m}$ full-width half-maximum (FWHM) beam size.

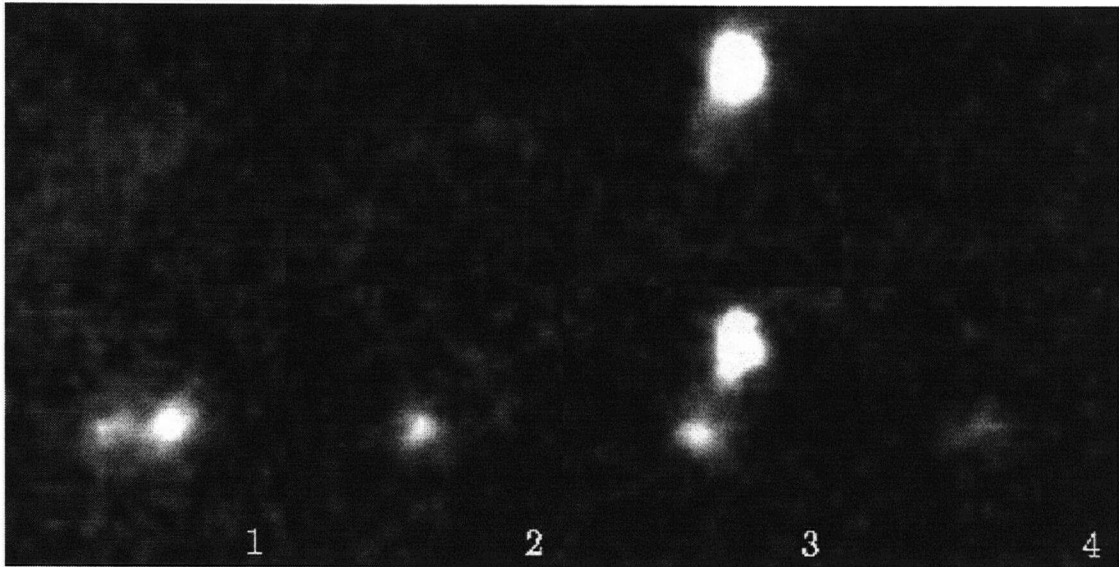


Figure 1.5: The four HEROs identified in the SDF survey are shown in the J -band (upper row of images) and in K' -band (lower row). Notice that SDF1 appears to be a merging system and SDF3 appears to be an interacting pair of galaxies (although they could just appear to be close neighbours through projection effects – see text).

ID	Position (2000.0)		K'	$J - K'$
SDF1	13 ^h 24 ^m 22 ^s 38	+27°29'49".5	20.91 (\pm 0.05)	2.97 (\pm 0.14)
SDF2	13 ^h 24 ^m 22 ^s 39	+27°29'01".9	22.03 (\pm 0.09)	3.65 (\pm 0.40)
SDF3	13 ^h 24 ^m 21 ^s 16	+27°29'01".9	21.99 (\pm 0.05)	2.81 (\pm 0.20)
SDF4	13 ^h 24 ^m 22 ^s 84	+27°30'08".4	22.31 (\pm 0.14)	4.12 (\pm 1.04)
Mean			21.57	2.99

Table 1.1: The positions, K' magnitude, and colour of the HEROs from Maihara et al. [46]. Astrometry is derived from the coordinates of a Hubble Space Telescope (HST) guide star in the flanking field. The estimated positional accuracy is $\pm 0''.15$.

One of the bright SDF HEROs may be a merging system and another may be part of an apparent interacting pair of galaxies (see Fig. 1.5), which could be exciting since mergers have been known to play a role in models of ULIRGs. To evaluate the likelihood of these objects appearing as close neighbours via chance projection effects, we use the P-statistic (see Downes et al. [22]). For a given surface density of objects N , the probability that an object lies within a distance d of another object at random is given by:

$$P = 1 - e^{-\pi d^2 N}. \quad (1.1)$$

Using $N = 10^5 \text{ deg}^{-2}$ down to $K \approx 22 - 23$ (Maihara et al. [46]) as the total galaxy counts in SDF, and an estimate that one of the HEROs lies within 1.5 arcsec of another galaxy, we calculate that there is only a 5.3 per cent chance that two galaxies would appear this close together at random. Using simple Poisson statistics and the previous result, we determine that there is an 80 per cent chance $((1.0 - 0.053)^4)$ of not seeing one galaxy pair (within 1.5 arcsec) among four galaxies. We consider how unlikely it would be to see a galaxy pair amongst the rare HEROs using a surface density of $3.5 \times 10^{-4} \text{ arcsec}^{-2}$

(5 HEROs in the $2 \text{ arcmin} \times 2 \text{ arcmin}$ SDF image³). The chance that two HEROs in the SDF lie within 1.5 arcsec of each other at random is 0.25 per cent. It is therefore extremely unlikely to see a pair of HEROs 1.5 arcsec apart if they were not interacting. Presumably, at least SDF1 could be an interacting pair and be well-described by a ULIRG-type galaxy.

Since we see one pair of HEROs in the SDF, the surface density of paired interacting HEROs is $1/(4 \text{ arcmin}^2)$ or 900 deg^{-2} . How bright do we expect a pair of HEROs be in the submillimetre? Assuming that we can select bright submillimetre objects by finding HEROs at IR wavelengths first, and supposing that we will be lucky to see a bright submillimetre source only 10 per cent of time, the surface density SCUBA-bright paired HEROs becomes 90 deg^{-2} . We locate this surface density on the $850 \mu\text{m}$ number counts plot (c.f. Fig. 1.6), and we find that this surface density predicts that the interacting pair of SCUBA-bright HEROs could have a flux level anywhere from 11 – 19 mJy, depending on how “lucky” we are to see bright submillimetre sources.

Given the high frequency with which SCUBA sources with luminosity in the range of 5 to 20 mJy are identified with very red EROs, and the number densities of both types of sources, it is reasonable to expect that these four sources might have measurable submillimetre flux. Totani et al. [63] deduced that SCUBA sources are likely to have the same origin as the HEROs in the SDF by comparing the surface density of HEROs to SCUBA sources. By estimating that HEROs make up 3 per cent of the total galaxy counts in the SDF, they estimate the surface density of HEROs to be $\approx 3 \times 10^3 \text{ deg}^{-2}$. This is similar to the surface density of 2 mJy SCUBA sources found by Borys [6] (see Fig. 1.6 for the $850 \mu\text{m}$ source count model).

The hypothesis that SCUBA sources are likely to have the same origin as HEROs is reasonable, and a submillimetre detection would strongly suggest that they are dusty starburst galaxies at reasonably high redshifts.

³For these purposes, we consider SDF1 to be a merger of two HEROs since they appear to be 2 separate objects in the K' -band.

1.4 Guide to This Thesis

In this thesis, fluxes for the four HEROs are determined from submillimetre observations, and we compare them to a model based on redshifting a galaxy template, and varying the overall luminosity and amount of dust reddening in the Infrared. We investigate 2 templates: Arp220 (a starburst galaxy) and NGC3938 (a normal cold spiral galaxy).

Chapter 2 describes the instrument and data reduction, Chapter 3 addresses the HEROs, Chapter 4 examines all of the SDF sources, and Chapter 5 states the conclusions that have been drawn from this work.

Standard cosmological parameter values of $H_0 = 75 \text{ km s}^{-1} \text{ Mpc}^{-1}$, $\Omega_\Lambda = 0.7$, and $\Omega_M = 0.3$ are assumed for this work.

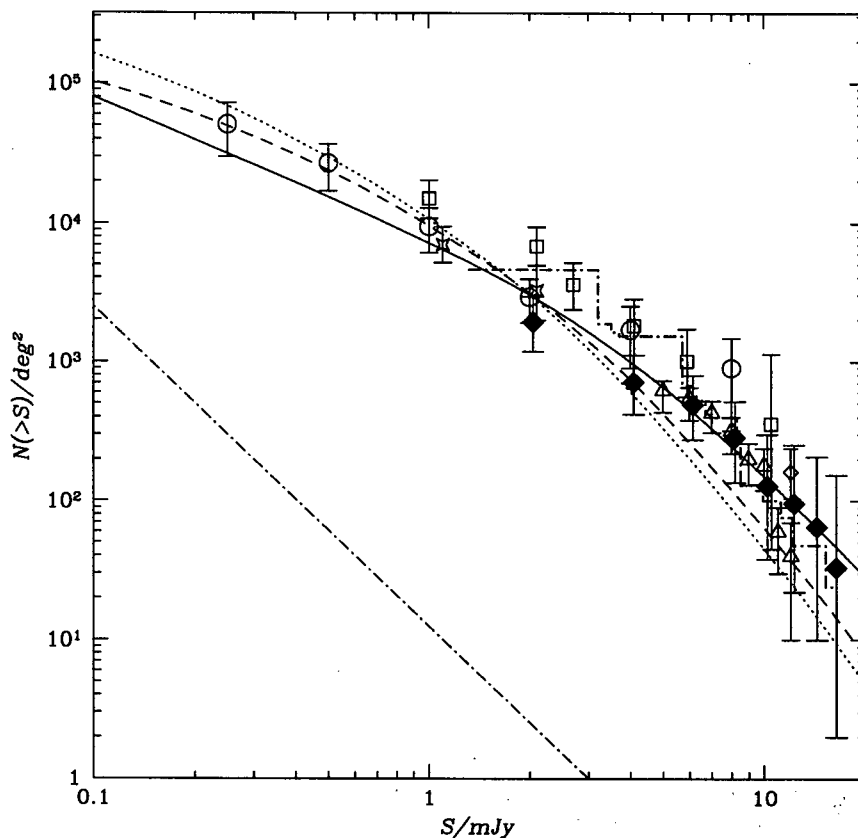


Figure 1.6: The 850 μm cumulative source counts. The solid diamonds and yellow jagged line denote results from Borys [6]. Open squares and circles represent source counts from cluster studies by Chapman et al. [14] and Smail et al. [59], respectively. The Scott et al. [56] UK 8 mJy survey counts are the open triangles. Stars mark the counts from Hughes et al. [38], and the open diamonds mark the counts from Borys et al. [8]. A two power-law model (solid line) is overlaid, as well as two predictions based on galaxy evolution models of Rowan-Robinson [49]. The dashed line is a $\Omega_\Lambda = 0.7$, $\Omega_M = 1.0$ universe, and the dotted line is a $\Omega_\Lambda = 0.7$, $\Omega_M = 0.3$ universe. The dot-dashed line near the bottom of the graph is the count prediction from extrapolating the *IRAS* 60 μm counts with no evolution. We use this plot to derive the number of sources we should see at the flux level of the HEROs. Use of this figure courtesy of Borys [6].

CHAPTER 2

THE INSTRUMENT AND DATA

2.1 The JCMT and SCUBA

The 15-metre diameter James Clerk Maxwell Telescope (JCMT) is the largest submillimetre telescope in the world and is situated atop Mauna Kea on the Big Island of Hawaii. At this height (approximately 13,400 feet or 4092 metres) we are above most of the water vapour in our atmosphere. It is very challenging to observe astronomical objects of interest in the submillimetre wavelength regime since there are very few “windows” where emission can penetrate the water-laden atmosphere, the largest opacity source in the submillimetre regime. The Submillimetre Common-User Bolometer Array (SCUBA) (Holland et al. [36]), a continuum detector mounted at the left Nasmyth focus of the JCMT, was built with special filters in these windows. Figure 2.1 shows the observed transmission of the SCUBA filters.

SCUBA has been in operation since May 1997 and is still the premier detector operating in the submillimetre regime and is the most highly cited instrument to date. The SCUBA detector has a field of view of 2.3 arcminutes and consists of hexagonal arrays of 37 and 91 bolometers operating at 850 and 450 μm , respectively (see Figure 2.2). It is cooled to about 70 mK, making it background-noise limited. Light collected by the telescope is reflected off of a series of mirrors, decreasing the f-ratio to $f/4$ where it is then split by a dichroic beam-splitter¹ with a 97 per cent transmission efficiency. The beamsizes for the arrays are telescope diffraction-limited and the 850 μm beam is well fit by a Gaussian with a FWHM of 14.7 arcseconds. The 450 μm beam has a FWHM of 7.5 arcseconds, although the beamshape is not so well-defined (it has significant sidelobes), is more prone to surface inaccuracies, and is characteristically less stable over time.

¹This allows the arrays to operate simultaneously

The Caltech Submillimetre Observatory (CSO) has a radiometer operating at 225 GHz which monitors the changing conditions in the atmosphere by performing skydips approximately every 10 minutes. We use the relations for the post-upgrade wide band filters derived by Archibald, Wagg & Jenness [1] to translate the CSO τ atmospheric opacity values to the wavelengths of interest in order to correct our data for sky extinction:

$$\tau_{850} = 4.02\tau_{\text{CSO}} + 0.001 \quad (2.1)$$

and

$$\tau_{450} = 26.2\tau_{\text{CSO}} + 0.014. \quad (2.2)$$

Often, the CSO τ meter is looking at a completely different part of the sky with a different airmass and it would be more desirable to measure the atmospheric opacity term at the same time and airmass as the astronomical source. In response to this need, since the summer of 2001 the JCMT has been using a cabin-mounted water vapour monitor (WVM) which looks at the 183 GHz water vapour line once every 6 seconds using a three channel double side band receiver. This instrument is particularly useful during unstable weather conditions, where the CSO tau meter may be giving unreliable readings.

2.1.1 Observing Modes

Sky emission dominates the astronomical signal being measured and must be removed. The secondary mirror “chops”, or nutates, at a default frequency of 7.8125 Hz with a user-defined chop “throw”, or amplitude, and position angle. This produces a differential measurement of the signal from the reference position and another point on the sky, effectively cancelling any rapid atmospheric background variations. The telescope also “nods” on and off the source (or “beam-switches”) every 10–20 seconds while chopping in order to compensate for the gradual change of the sky brightness over the timescale of an observation.

SCUBA has four standard modes of operation: photometry, jiggle-mapping, scan-mapping, and polarimetry. We will briefly describe the first two since they were the

Measured SCUBA filter profiles

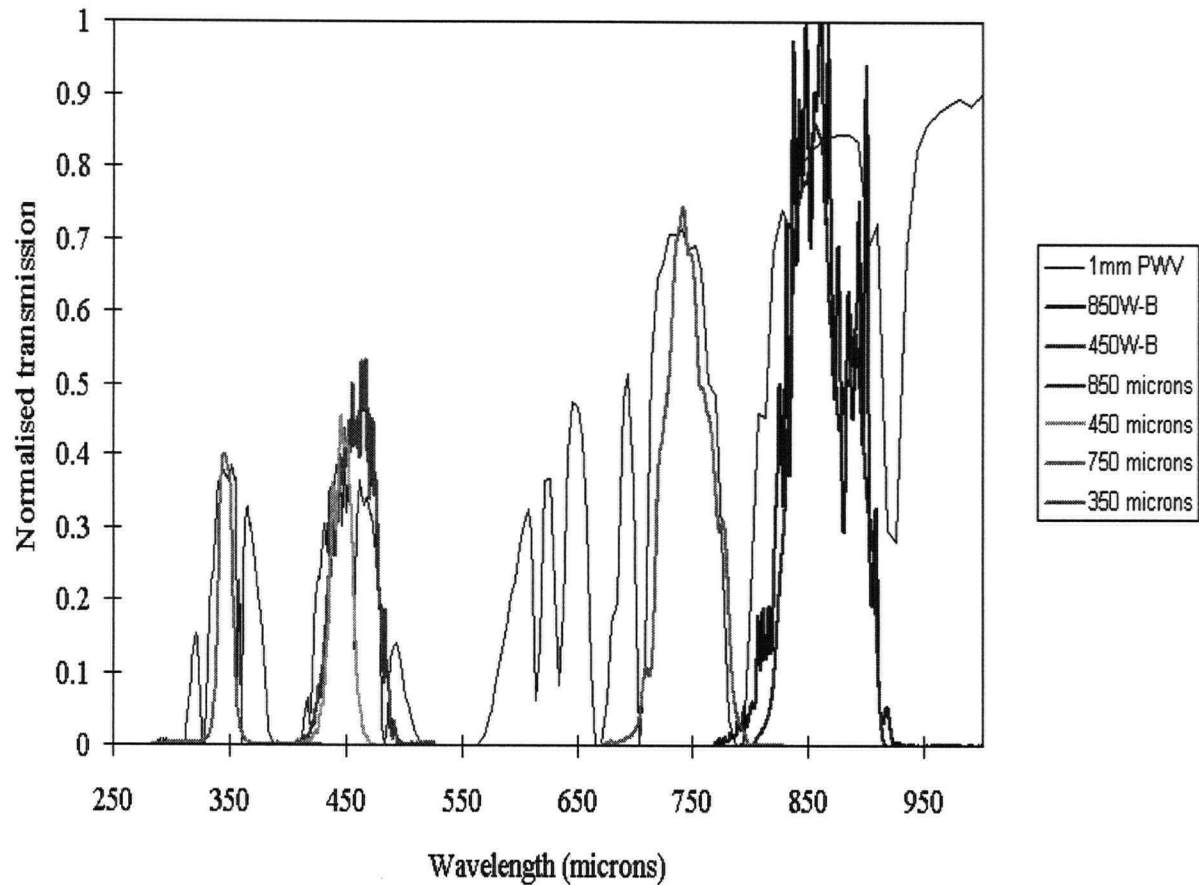


Figure 2.1: This figure shows the wideband filter profiles measured in 2000 with the University of Lethbridge Fourier Transform Spectrometer. They are plotted over the old narrowband filter profiles for comparison. The thin black line (1mm PWV) traces the submillimetre transmission function assuming a precipitable water vapour content of 1mm. This figure was created by David Naylor and Wayne Holland and is from the JCMT website.

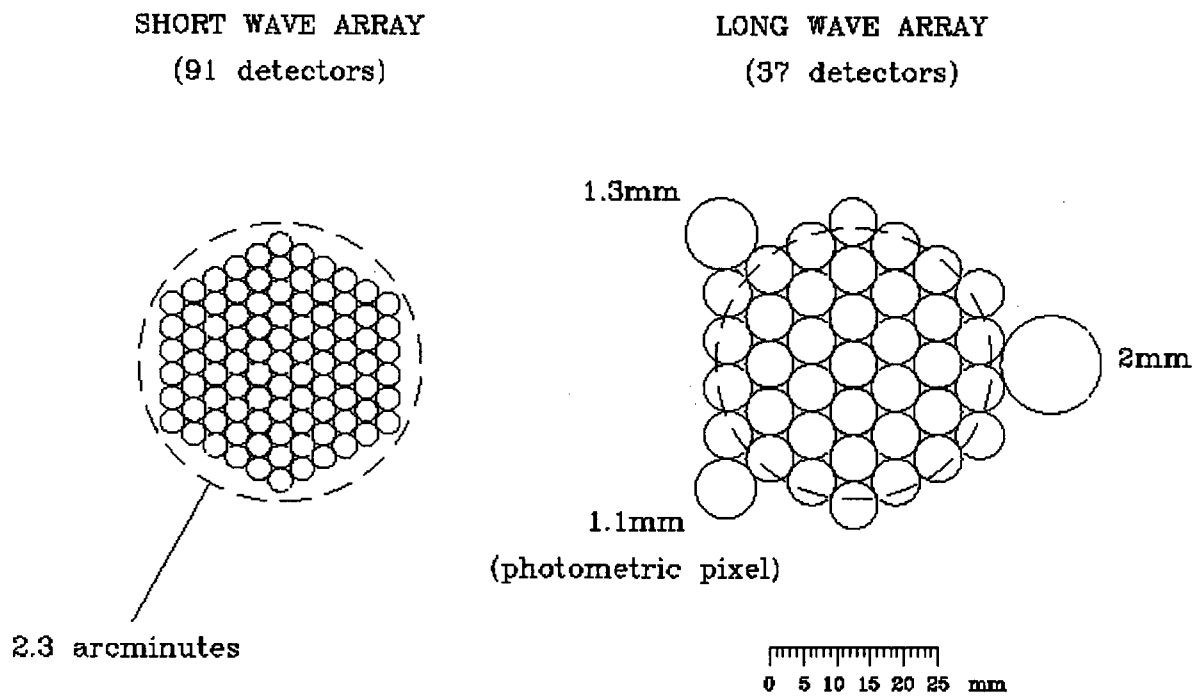


Figure 2.2: This figure displays the arrangement of bolometers in the short wave and long wave SCUBA arrays, which operate simultaneously at 450 and 850 μm , respectively. This figure is from the JCMT website.

modes used for this work.

Photometry

Photometry is used for small point sources and is done by pointing the central bolometer at the target and then making a very small 9-point jiggle around the source position, resulting in an undersampled map. This is the most efficient mode for getting down to the desired signal-to-noise level for a point source with accurately known coordinates. Each integration takes approximately 18 seconds including the nod.

Jiggle-Map

The jiggle-mapping mode is ideally suited for sources larger than a beam, but less than 2.3 arcminutes in extent. The secondary mirror makes a 16-point jiggle pattern of offset positions from the source's central pointing position. This produces a fully sampled image at $850\ \mu\text{m}$. In order to get a fully sampled image at $450\ \mu\text{m}$, the telescope must make a 64-point jiggle pattern, as 3 arcsecond spacing between points is required as opposed to the 6 arcsecond spacing required at $850\ \mu\text{m}$. Each integration takes approximately 128 seconds including the nod.

2.2 Observations

The SDF was observed with a resolution of 14.7 arcsec and 7.5 arcsec at 850 and $450\ \mu\text{m}$ respectively with SCUBA on the JCMT during May 2001, May 2002, February and March 2003. The centre of the field lies at an approximate RA and Dec (J2000) of $13^{\text{h}}24^{\text{m}}21^{\text{s}}20$ and $+27^{\circ}29'25''0$. 64-point jiggle map data of the SDF were obtained, providing measurements of the continuum at both wavelengths simultaneously with SCUBA. In addition, 9-point photometry data were obtained in 2002 and 2003 using the central bolometer on the SCUBA array for each of the four HEROs and one suspected redshift 7 source².

²The estimated photometric redshift of $z = 7$ was derived for one of the SDF galaxies by Kashikawa et al. [43].

The atmospheric zenith opacity at 225 GHz was monitored with the CSO tau monitor in 2001 and 2002 and with the JCMT water vapour monitor at 183 GHz in 2003. Table 2.1 summarizes the observations, telescope parameters, and weather conditions.

The secondary mirror was chopped at the standard frequency with alternating position angles of 0 and 90 degrees and chop throws ranging from 30 to 86 arcsec. Pointing checks were performed hourly on blazars and planets, and offsets from the pointing centre were nominal in all cases. Observations were co-added to create maps with total integration times of 13.5 hours at 450 μm (excludes poor-weather photometry-mode data from 2002) and 16.5 hours at 850 μm , over a variety of weather conditions. The maps have estimated rms values of about 15 and 2 mJy, at 450 and 850 μm , respectively.

Object	Observing Mode	Date	τ_{850} range	Chop Coords	Chop Throw (arcsec)	Psn. Angles (degrees)	Int. Time (hours)
SDF	Jiggle Map	May 27, 2001	0.25–0.44	LO	30,40	0,90	3.91
		Mar 2, 2003	0.18–0.21	AZ	30	0	0.71
		Mar 3, 2003	0.17–0.21	AZ	30,40	90	2.84
		Mar 4, 2003	0.22–0.23	AZ	30,40	90	0.71
		Mar 8, 2003	0.44–0.44	AZ	30,40	90	0.71
SDF1	Photometry	Feb 6, 2003	0.24–0.27	AZ	35,65	90	1.2
		Feb 9, 2003	0.18–0.19	AZ	35,65	90	0.4
SDF2	Photometry	May 16, 2002	1.03–1.25	AZ	33,82	90	1.05
		May 17, 2002	1.10–1.17	AZ	33,82	90	1.95
SDF3	Photometry	Feb 10, 2003	0.14–0.18	AZ	33,82	90	0.8
		Feb 9, 2003	0.16–0.18	AZ	32,86	90	0.8
SDF4	Photometry	Feb 10, 2003	0.12–0.16	AZ	35,49	90	0.8
		Mar 5, 2003	0.26–0.28	AZ	60	90	0.6
Total Int Time							16.48 hours

Table 2.1: Observations of the SDF with SCUBA. The last column (integration time) refers to the total on-source time, including the nod, minus all other observing overheads. “LO” refers to chopping in fixed RA/Dec coordinates, and “AZ” refers to azimuthal chopping (i.e. the sky is allowed to rotate with respect to the orientation of the array during the course of an observation).

2.2.1 Added Noise in the 2003 Data

In June 2003, Colin Borys, a former UBC PhD. student, discovered a large power spike at $\approx 1/16$ Hz coincident with the frequency of the secondary chopper in de-nodded, flatfielded, and extinction corrected 64-point jiggle map data. The telescope performs 1.024 second integrations on each of the 16-point jiggle pattern positions and nods to one side before repeating this procedure and nodding to the opposite side. This pattern is repeated two more times to complete a 64-point jiggle pattern³. Thus, the telescope is moving by a large amount every 16 seconds (1 nod every 16 points \times 1.024s/point \approx 16 nods/s). We hypothesize that there may be some microphonic noise pickup when the telescope moves during the nod, corresponding to the noise appearing stronger in the bolometers at a frequency of $\approx 1/16$ Hz.

300 jiggle map observations between 1998 and 2003 were analyzed by Colin Borys and Remo Tilanus of the Joint Astronomy Centre (JAC), and only observations taken between December 2002 and March 2003 seem to be affected by this anomaly (see Fig. 2.3). The SCUBA fridge cycle at the end of March is likely responsible for fixing the problem (Borys 2003, private communication). Upon analysis of the fourier spectrum of our data, we discovered that this power spike occurs on the long-wave array in about two-thirds of the bolometers, while the remaining third had nominal signals, similar to what Borys found. The effect is also present in the short-wave array, but to a lesser extent. Only about 10 per cent of the bolometers show this noise spike.

Usually this effect would be automatically removed after subtracting off the sky signal if all of the bolometers had this same spurious signal present in their frequency spectra. But since only a fraction of the bolometers have this signal, the effect of removing the mean sky background actually imposes this signal on the non-affected bolometers, corrupting them as well. The concern is that the presence of a periodic noise fluctuation on a similar timescale to the jiggle pattern may be affecting the data, thereby imposing

³When SURF de-nods the data, each data point it reports is actually the sum of two 1.024 second measurements taken 16 seconds apart.

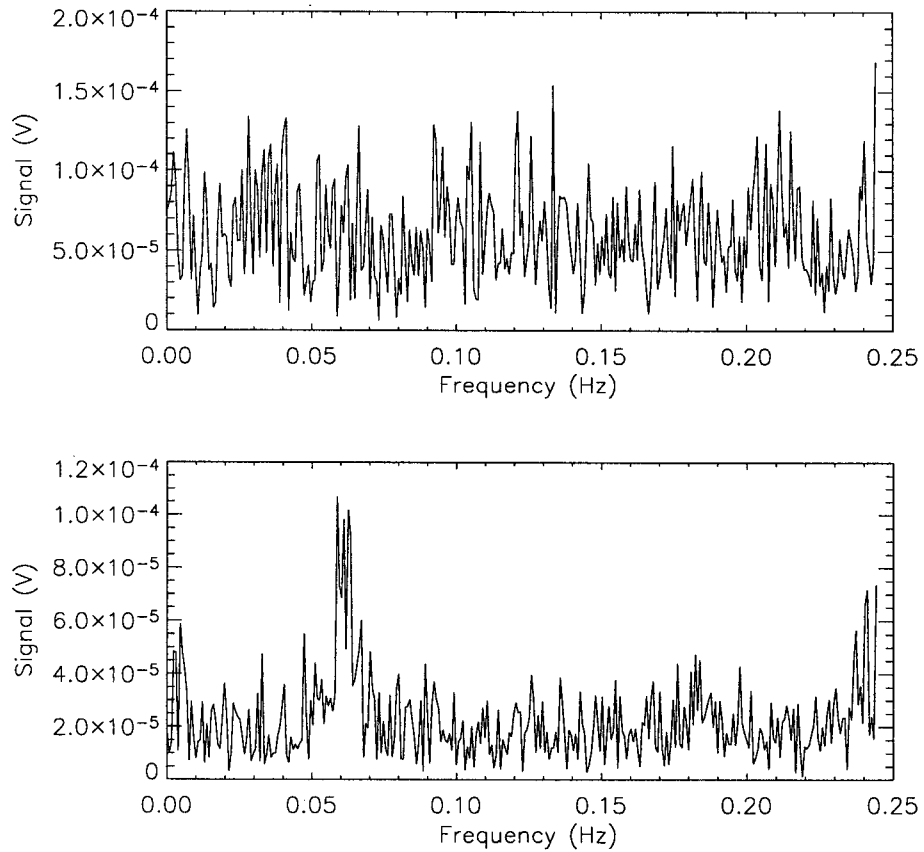


Figure 2.3: The top plot is the FFT of the timestream for bolometer G15 (or number 12) of the long-wave array, from 64-point jiggle map data taken of the SDF in May 2002. The bottom plot shows the FFT of the timestream for the same bolometer from 64-point jiggle map data taken of the same field in March 2003. Note the power contained in the large noise spike at about 1/16 Hz in the lowermost plot.

unwanted structure on the map data to some degree. (Borys 2003, private communication).

The data were examined in a variety of ways. First, we tried three different methods of separating the data: averaging all of the 2003 data together, separating the data according to chop throw and position angle and taking the average, and concatenating all of the timestream data for one night. Upon examination of the fourier spectrum of each of these new averaged data-sets we observed that the signal persisted. In the 2003 averaged data-set, the signal decreased by about an order of magnitude, but so did the overall noise level, resulting in a constant signal-to-noise ratio for the spike. See Fig. 2.4 for an example.

We first investigate if and how this additional noise affects the data in the time domain (i.e. the bolometer timestream). We trace how the standard deviation (σ) of the signal varies with time. One jiggle observation consists of 10 integrations of a 64-point jiggle pattern, adding up to 640 timestream elements for each bolometer. For the central bolometer H7 (number 19), we calculate a noise of $\sigma = 0.410$ V over the course of one ten-integration observation. For a single bolometer, we calculate the mean and error of each 64-point jiggle map integration and see no trend for the error (noise) either increasing or decreasing over the set of ten integrations. We therefore conclude that the noise is randomly fluctuating, as it does not vary significantly in the bolometer timestream over the course of an observation.

Next, we investigate if and how the noise spike affects the data in the spatial domain (i.e. the map structure). Obviously, one might worry that unwanted structure is being imposed on the map. We trace how the signal varies across the 64-point jiggle pattern array. A bolometer will hit 64 different positions in the sky during the course of one 64-point jiggle integration. Since each observation is made up of ten integrations, each position will be hit 10 times during the course of an observation. We add up the contribution of each integration at each jiggle position, calculate the mean, σ and the error in σ , and look for a trend in the noise. We do not see any trends of the noise either increasing or decreasing. For an error of $\sigma = 0.410$ V (found above), we determine the typical error

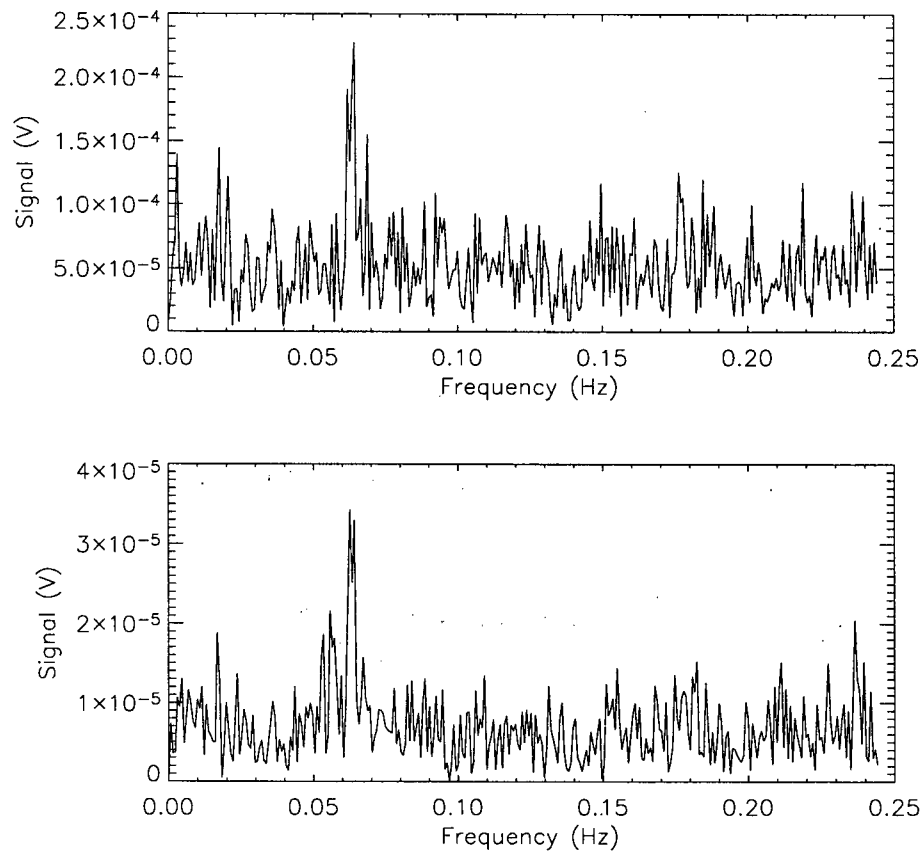


Figure 2.4: The top plot is the FFT of the timestream for bolometer G15 (or number 12) of the long-wave array, from 64-point jiggle map data taken of the SDF in March 2003. The bottom plot shows the FFT of the timestream for the same bolometer from the average of all the 2003 64-point jiggle map data taken of the same field. Note the factor of ≈ 10 decrease in the power of the noise spike at about 1/16 Hz and in the overall noise level in the lowermost plot from the one above.

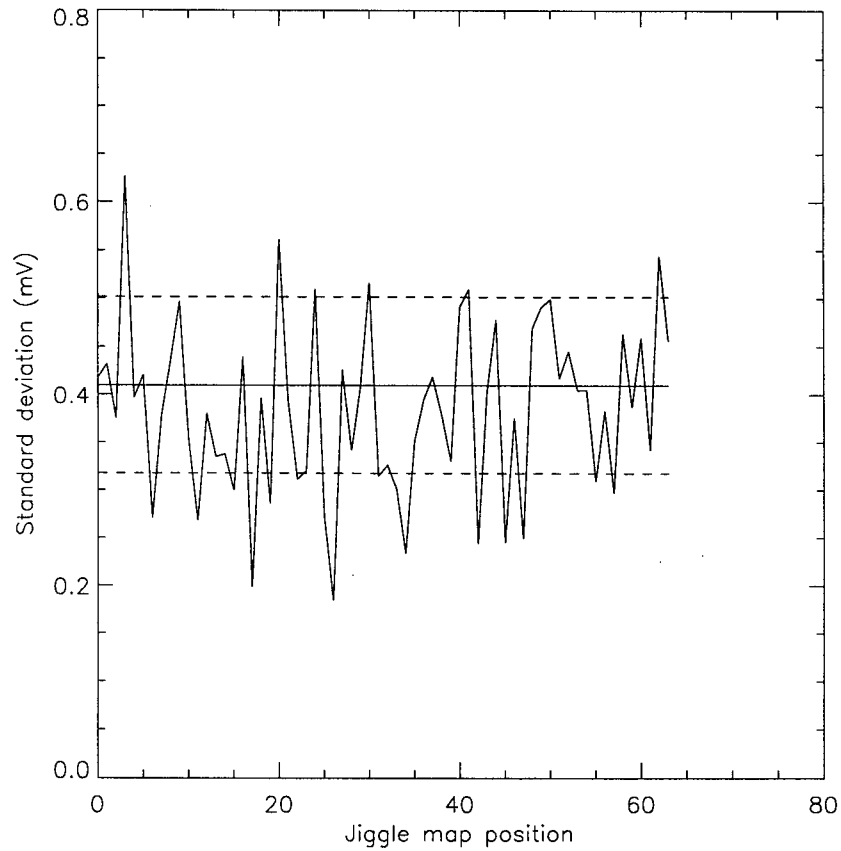


Figure 2.5: This plot shows the standard deviation of ten points (ten integrations) for each of the 64 different jiggle positions for the central bolometer, H7. The solid line represents the mean standard deviation value. The dashed lines represent the 1σ error in the standard deviation ($\simeq \pm 1/\sqrt{2N}$).

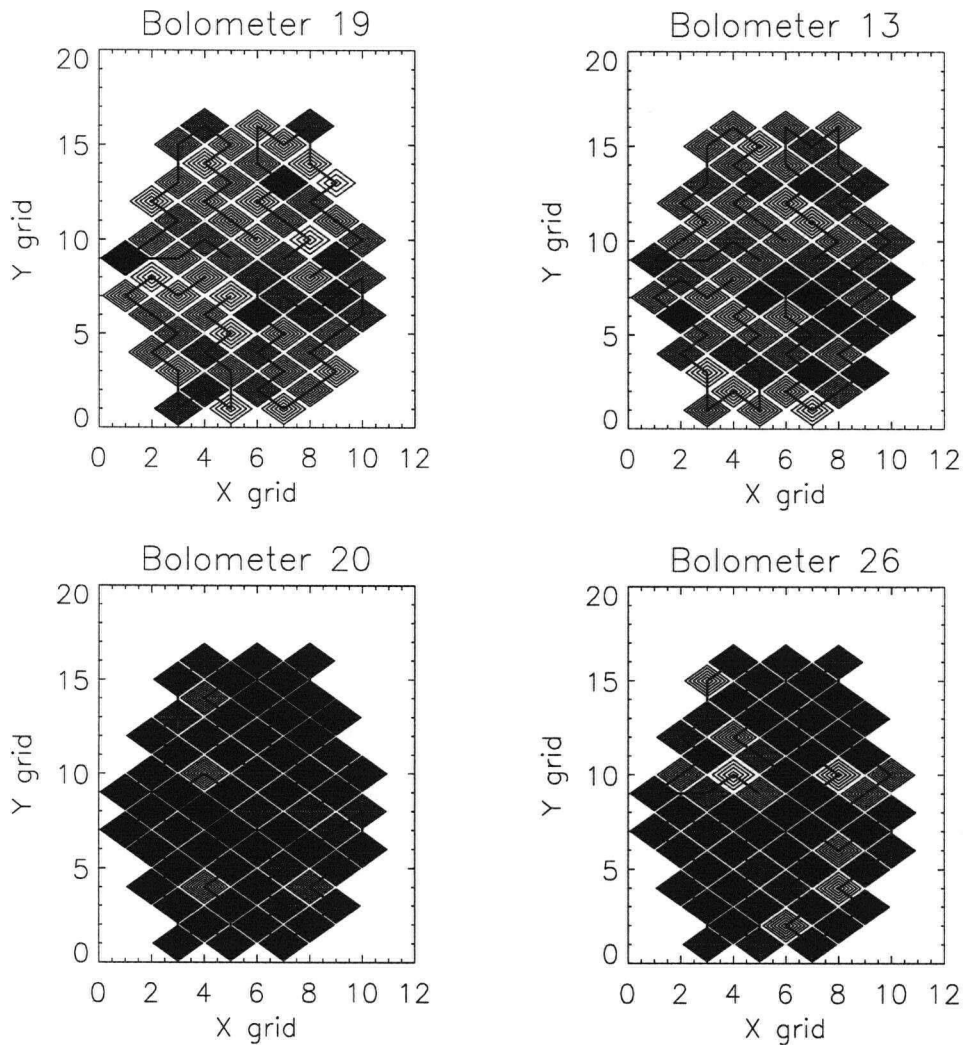


Figure 2.6: The 64-pt jiggle pattern is observed in 4 sections of 16 points (solid lines). For 4 different bolometers on the array, we plot the standard deviation of ten measurements (ten integrations) at each position in the 64-point jiggle pattern using contours to specify the noise level. Contours begin at $\sigma = 0.0$ and increase in steps of 0.05 up to a maximum of $\sigma = 1.0$. It is evident that the noise varies randomly across the array for any given bolometer.

in σ to be about 0.0920 V. Figs. 2.5 and 2.6 illustrate that the noise appears to vary randomly over the course of 64-point jiggle pattern for a given bolometer. We conclude that the noise is randomly fluctuating, does not depend on position, and therefore does not impose any structure on the map.

Colin Borys postulates that there was some kind of vibration-induced microphonic pickup when the telescope suddenly moves at the end of the 16 point jiggle pattern to nod, making the noise on the array stonger at a frequency of 1/16 Hz. It may also be due to a noisy atmosphere or to a temperature instability which makes the bolometer gains fluctuate in a random way (which would have been fixed by the SCUBA fridge cycle). In any case, we conclude that the large power spike at 1/16 Hz is just introducing more random noise ($\approx 1/\sqrt{2}$) into the data and not imposing any structure on our maps.

2.3 Data Reduction

2.3.1 Preliminary Reduction with SURF

The SURF (SCUBA User Reduction Facility; Jenness & Lightfoot [40]) reduction packages were used for nod compensation (`reduce_switch`), flat-fielding (`flatfield`) and extinction correction (`extinction`) of the data. The `reduce_switch` command subtracts the off-position from the on-position and splits the raw data array into separate components. Next, the `flatfield` command “flatfields” or corrects the gain of the array by multiplying each bolometer by the volume flatfield value relative to a reference pixel, usually the central pixel of the array. The `extinction` command corrects the data for source airmass (elevation) and sky opacity, τ . A great deal of care was taken to eliminate any spikes in the CSO τ readings using the polynomial fits provided by the JAC, and a constant τ value was used over the duration of each observation. The `extinction` command has the capability to interpolate between two specified τ values (before and after the observation) but the τ did not vary significantly during the course of any one observation so this feature was not used. This last command also splits up the data into

the two different wavelength components, namely 850 and 450 μm .

The work produced in this thesis made use of locally developed code written in C++ by Colin Borys (Borys [6]) for his UBC doctoral dissertation. We converted the observation files into the more versatile “FITS” format using the program SCUBA2FITS, making it readable for the next series of locally developed programs. The files all now contain a header, and an array of three vectors containing: data timesteps, bolometer number, and the data. The data vector itself contains the signal in Volts and three RA/Dec offset positions corresponding to the three positions on the sky that the bolometer looked at while taking the difference measurement.

2.3.2 Making the Maps

A program called BS_SCAN_REDUCE was then used to 4σ despiked and rebin all data types (photometry and jiggle maps) into a single map, producing three useful data products (similar to those that can be produced by SURF): a signal map, a noise map (the standard deviation or σ), and a signal-to-noise ratio (SNR) map. Bad pixels were essentially eliminated by weighting each pixel by its timestream inverse variance relative to the central pixel. The data were despiked by means of calculating the root-mean-square (rms) for each bolometer and rejecting any data 4 times greater than this value. Sky subtraction was performed by calculating the mean sky at each timestep using the median of all of the bolometers save the noisiest bolometers and subtracting this result from the data. A bolometer was deemed too noisy to include in the sky subtraction by calculating its variance and cutting out the bolometers that were above a certain threshold (usually $\sigma > 0.005$).

The flux from the negative off-beams were then “folded in” to increase the overall sensitivity of the 850 μm map. For each sample in the bolometer timestream, we add -0.5 times the measured flux to the position of the off-beam. Since a bolometer spends only half as much time in each of the off-positions (reference positions that do not lie on the target) as in the on-position during the course of a single observation, we assign the

on-position a weight of $w = 1$ and the off-positions weights of $w = -0.5$ each⁴. Following the treatment by Sajina [50], the folding can be represented by:

$$\mu = \frac{\sum_{i=1}^3 \frac{w_i x_i}{\sigma_i^2}}{\sum_{i=1}^3 \frac{w_i^2}{\sigma_i^2}} \quad (2.3)$$

and

$$\sigma = \frac{1}{\sqrt{\frac{w_i^2}{\sigma_i^2}}}, \quad (2.4)$$

where μ is the mean, σ is the standard deviation, and x is the voltage measured. It should be noted that the beam is assumed to be Gaussian in shape which is usually the case at $850 \mu\text{m}$ but not at $450 \mu\text{m}$, where the beam is often more severely distorted and non-Gaussian in shape. Therefore we do not fold in the off-beams to produce the $450 \mu\text{m}$ map. In this way, folding in the off-beams will improve the sensitivity of the map by about a factor of:

$$\frac{1}{\sqrt{0.5^2 + 1.0 + 0.5^2}} = \sqrt{\frac{2}{3}} \quad (2.5)$$

The “-f” option of the BS_SCAN_REBIN program was used to produce this result. This step is essentially equivalent to a single iteration in the iterative deconvolution technique described in Borys [6]. This method is only valid if sources are far enough apart and are not being chopped onto one another. We have taken great care to use a chopping strategy that avoids the HEROs being chopped onto each other by selecting appropriate chop throws in azimuthal coordinates, allowing the chop position to rotate on the sky during the observation (see Fig. 2.7). This procedure of folding in the off-beams was used successfully by Borys [6] to produce the Hubble Deep Field Supermap and by Eales et al. [26] to produce the 14 Hour Field, for example.

The $850 \mu\text{m}$ data were then regridded onto a rectangular grid of 3 arcsec pixels and smoothed using the program BS_SMOOTHFIT to a final FWHM of 14.7 arcsec (the size

⁴This can also be seen in that for an observation, both values vary as N^{-1} since $\mu = (1/N_{\text{tot}})(\sum_{j=1}^{N_{\text{tot}}} x_j)$.

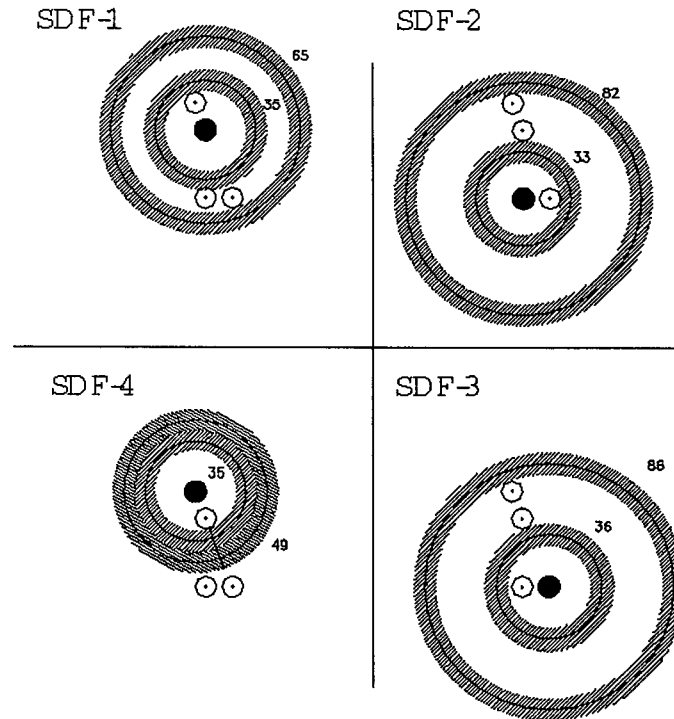


Figure 2.7: We plot the chopping strategies for photometry observations of the four HEROs. For each plot, the shaded source is the HERO that the central bolometer is pointed at during photometry, and the other small circles (scaled to the represent the beam-size at $850 \mu\text{m}$) represent the other HEROs in the field. We also plot the path that the bolometer will chop on the sky as the sky rotates during the night. We label the chop throws in arcseconds on each path.

of the JCMT beam at $850\ \mu\text{m}$) and the $450\ \mu\text{m}$ data were smoothed to a FWHM of 7.5 (the beamsize at $450\ \mu\text{m}$). By rebinning the $850\ \mu\text{m}$ map using 3 arcsec pixels, the map will have pixels which are correlated since the beam is 4.93 of these new pixels wide. Another reason for smoothing is that the 3 arcsecond pixel grid gives an artificially small resolution which is not the true resolution of the image (given by the beam size) and will have the effect of making the map appear more noisy than it truly is.

Neglecting the undersampled and hence noisier edges of the map, we get a mean signal of $-0.047 (\pm 0.03)$ mJy from the central 3425 pixels of the $850\ \mu\text{m}$ map. This is in agreement with the expected map average of 0 mJy for differential measurements. As a check, we examine the rms of the map without the off-beams folded in and compare it to the rms of the map with the off-beams folded in. The rms before off-beam folding is 2.26 mJy and the rms post off-beam folding is 1.80 mJy, which is entirely consistent with an estimated resulting rms of $2.26 \times \sqrt{2/3} = 1.85$. Similarly, we measure the mean signal of the central 1662 pixels of the $450\ \mu\text{m}$ map to be $0.32 (\pm 0.24)$ mJy. We measure an rms for the $450\ \mu\text{m}$ map of 9.7 mJy.

2.3.3 Calibration

Because the map is output in Volts and we wish to measure flux in an astronomically-meaningful units (i.e. mJy) we must calibrate the data-set by observing objects with known submillimetre fluxes.

For consistency, the calibrators were reduced in the same way as the SDF map and the mean of the peak pixel values of the calibration sources were used to convert the measurements into units of flux. See table 2.2 for the list of average FCFs used. We adopt the average value of all of the flux conversion factors (FCFs) obtained over one night of observing and use this value as the FCF for every observation on the same night. The average values and standard deviations of all of the FCFs we obtained are $224 (\pm 27)$ mJy at $850\ \mu\text{m}$ and $339 (\pm 120)$ mJy at $450\ \mu\text{m}$. These flux conversion factors are consistent with the standard gains (within the uncertainties) at 450 and $850\ \mu\text{m}$ of

308(± 109) and 219(± 21) mJy, respectively, from the JCMT website. For photometry mode, the standard gains are slightly different: 384(± 82) and 197(± 13) mJy/Volt at 450 and 850 μm .

Rms uncertainties in the calibrations are approximately 10 per cent for the 850 μm jiggle map and photometry data and 30 per cent for the 450 μm jiggle map data-set. These uncertainties are mainly caused by the variability of the atmospheric transmission and changes in the dish surface accuracy induced by temperature fluctuations (Jenness et al. [41]).

2.3.4 Flux Measurements

SCUBA operates at wavelengths appropriate to detect thermal emission from dust with temperatures of 3–30K. At higher temperatures (excluding high-redshift objects), dust radiates mostly in the far-IR, so high-redshift far-IR emitters will have this emission redshifted into the submillimetre (Holland et al. [36]). Since the angular extent of any of these sources is likely to be much smaller than the 3 arcsec pixel size (for example a 1 kpc source at a distance of $z = 3$ would appear to be 0.14 arcsec in the sky), we simply measure the flux of each source in the pixel corresponding to the near-IR source coordinates on the beam-convolved map. The best estimate of the noise associated with each pixel is given in the noise map. We ignore the calibration uncertainty, which is unimportant with these low signal-to-noise ratio data. The flux measurements include contributions from all jiggle map and photometry data which have all been inverse-variance weighted in the co-addition process. The final maps are displayed in Figs. 2.8 and 2.9. The results for the HEROs are summarized in Table 2.3. It is interesting to note that the 3 reddest objects ($J - K' > 3$) all have positive submillimetre flux greater than the least red HERO, SDF3.

Date	Observing Mode	Number of Calibrators	FCF_{450} (mJy/Volt)	Number of Calibrators	FCF_{850} (mJy/Volt)
May 27, 2001	Jiggle Map	5	325	8	235
May 16, 2002	Photometry	–	–	0	*197
May 17, 2002	Photometry	–	–	0	*197
Feb 6, 2003	Photometry	2	324	2	201
Feb 9, 2003	Photometry	0	*384	0	*197
Feb 10, 2003	Photometry	2	404	2	233
Mar 2, 2003	Jiggle Map	2	292	2	200
Mar 3, 2003	Jiggle Map	3	402	3	232
Mar 4, 2003	Jiggle Map	1	318	1	219
Mar 5, 2003	Photometry	3	417	3	230
Mar 8, 2003	Jiggle Map	4	260	5	215

Table 2.2: For each night of data, a different Flux Conversion Factor (FCF), or gain, is derived from the average value of calibration observations taken near to the observations. In cases where the calibration source was too extended to give a useful measurement or where too few calibration observations were made (denoted by an asterisk), we just use the “standard” gain value from the JAC website. The $450\ \mu\text{m}$ data from May 2002 were not used because the weather was very poor (see Table 2.1). The standard gains are $308(\pm 109)$ and $219(\pm 21)$ mJy/Volt at 450 and $850\ \mu\text{m}$ respectively in mapping-mode and $384(\pm 82)$ and $197(\pm 13)$ mJy/Volt in photometry mode (c.f. SCUBA calibration webpage).

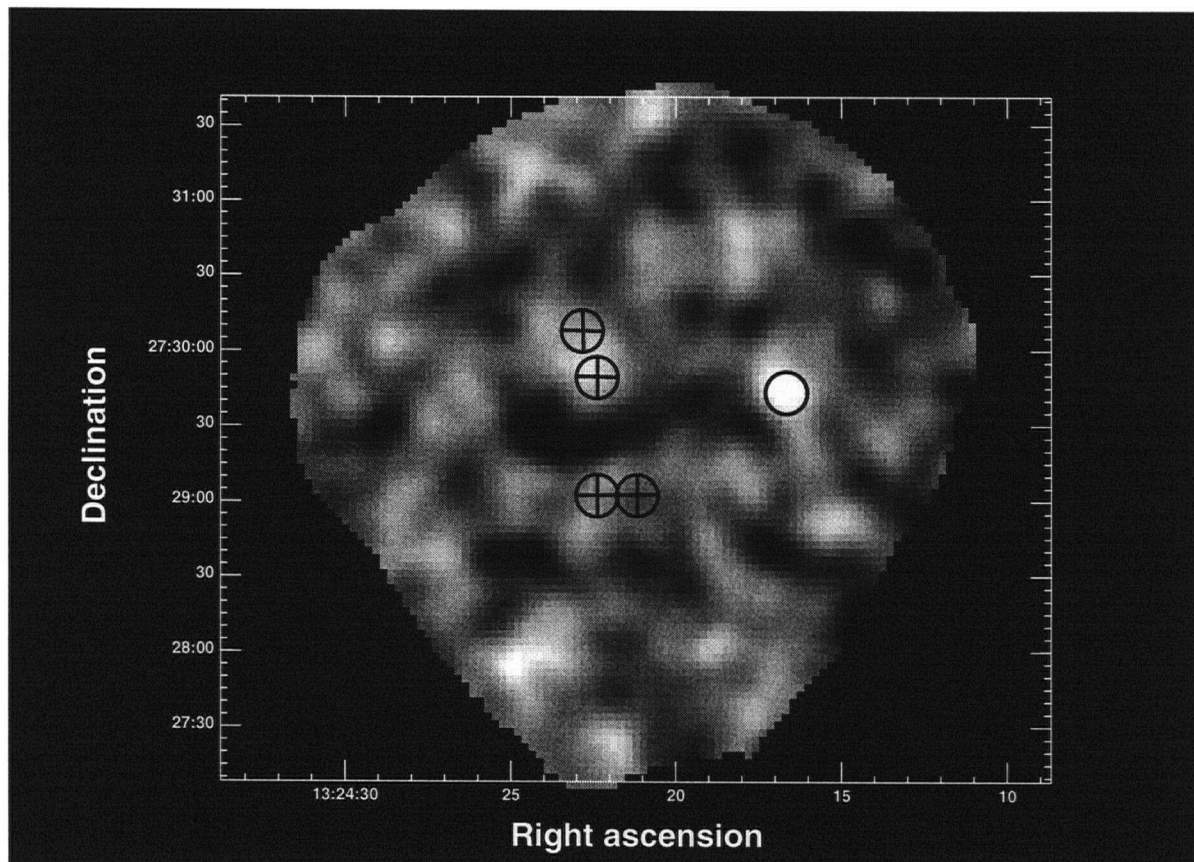


Figure 2.8: The Subaru Deep Field $850 \mu\text{m}$ signal-to-noise ratio (SNR) map. The brightest points have a SNR of $\approx 3 - 4$ and the lowest points have a SNR of ≈ -3 . The circles are roughly 14.7 arcsec in diameter, the size of the SCUBA $850 \mu\text{m}$ FWHM beam size. The circles with crosses inside mark the location of the four HEROs, and the other circle marks a $> 3\sigma$ detection.

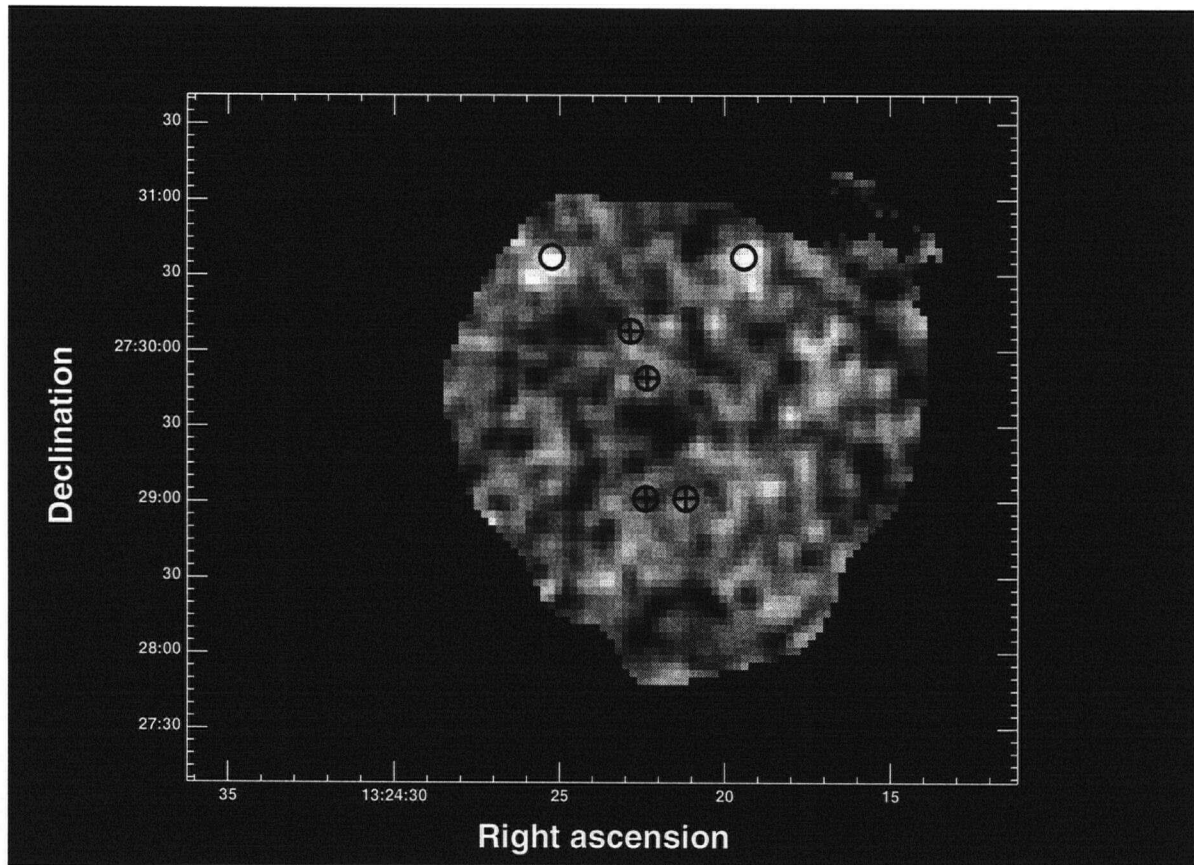


Figure 2.9: The Subaru Deep Field $450 \mu\text{m}$ signal-to-noise ratio (SNR) map. The brightest points have a SNR of $\approx 3 - 4$ and the lowest points have a SNR of ≈ -3 . The circles are roughly 7.5 arcsec in diameter, the size of the SCUBA $450 \mu\text{m}$ FWHM beam size. The circles with crosses inside mark the location of the four HEROs, and the other two circles mark $> 3\sigma$ detections.

ID	S_{450} (mJy)	S_{850} (mJy)	Upper Limits S_{850}
SDF1	1.47 (\pm 5.94)	2.15 (\pm 0.92)	< 3.46
SDF2	-7.84 (\pm 6.36)	1.01 (\pm 0.94)	< 2.64
SDF3	6.10 (\pm 6.48)	-0.22 (\pm 0.88)	< 1.63
SDF4	1.73 (\pm 5.76)	1.85 (\pm 0.98)	< 3.45
Mean	0.42 (\pm 3.06)	1.15 (\pm 0.46)	< 1.76

Table 2.3: Measured flux densities with errors and predicted redshift upper limits for the four SDF HERO sources. The fourth column lists the 95 per cent Bayesian upper limits (in mJy) at $850 \mu\text{m}$. The bottom row lists the error-weighted mean of the $850 \mu\text{m}$ fluxes, and the 95 per cent Bayesian upper confidence limit to this mean flux.

CHAPTER 3

HEROS

In the following chapter, we estimate the cirrus contribution to our $850\ \mu\text{m}$ map. We also briefly discuss the relation between HERO colour and submillimetre flux. We then create two template SEDs, a starburst galaxy and a normal galaxy, and use them to facilitate estimates of the redshifts of the HEROs. We compare and evaluate the models to determine how realistic these templates are at describing the HEROs.

3.1 Cirrus Contribution

We need to estimate the amount of cirrus contribution to our map in case it is providing a large fraction of the flux, which would mean we are just measuring galactic emission and not extragalactic sources at all. We use a portion of the Schlegel, Finkbeiner & Davis [53] full sky $100\ \mu\text{m}$ map, a reprocessed composite image of the *COBE/DIRBE* (Diffuse InfraRed Background Experiment) and *IRAS/ISSA* (*IRAS* Sky Survey Atlas) maps. These authors carefully removed zodiacal foreground emission, artefacts from the *IRAS* scan pattern, and confirmed point sources, resulting in a map with *DIRBE*-quality calibration and *IRAS* resolution. From this map we obtain $0.9\ \text{MJy/steradian}$ in the direction of the SDF pointing centre coordinates.

Franceschini [30] presents a plot of the SED of the diffuse dust due to cirrus for a nearby prototype starburst galaxy, M82. From this plot, we take the ratio of the cirrus contribution at $100\ \mu\text{m}$ to the contribution at $850\ \mu\text{m}$ and scale the $100\ \mu\text{m}$ cirrus measurement by this ratio in order to estimate the $850\ \mu\text{m}$ cirrus contribution.

We obtain a cirrus flux contribution of $5 \times 10^{-4}\ \text{MJy/sterad}$ at $850\ \mu\text{m}$. Given that there are about 60,000 14.7 arcsecond SCUBA beams in 1 square degree of sky, the flux contribution becomes $2 \times 10^{-3}\ \text{mJy}$ per SCUBA beam at $850\ \mu\text{m}$. This is much less than

the confusion limit of our map (≈ 1 mJy) and is extremely negligible. At $450\ \mu\text{m}$ we obtain a cirrus flux contribution of 3×10^{-3} MJy/sterad. The $450\ \mu\text{m}$ cirrus contribution is 4×10^{-3} mJy due to the smaller beam size of 7.5 arcseconds FWHM. We can therefore safely ignore the negligible contribution of cirrus in our measurements.

3.2 HERO IR Colours and $850\ \mu\text{m}$ Fluxes

SCUBA galaxies are often found to be associated with EROs but we have shown that hyper-EROs are not always necessarily associated with SCUBA-bright galaxies. We do not find that the HEROs are SCUBA-bright, and we also do not find any evidence for their $850\ \mu\text{m}$ submillimetre flux increasing with $J - K'$ colour. The latter finding is illustrated in Fig. 3.1, where we plot $850\ \mu\text{m}$ against $J - K'$ colour and get a slope of 0.81 ± 0.89 and a χ^2 value of 3.3 for the best-fit line through the data. Given that extremely red objects associated with SCUBA sources tend to be dusty starburst galaxies, we might expect an overlap between the HEROs and the ULIRG population at high redshifts. We use the SED of Arp220, constrained to fit the near-IR and submillimetre observations, to investigate if this is a reasonable assumption. We compare the results against a normal galaxy template as well.

3.3 Using Arp220 as a Template

We created a template SED using public photometric data available for Arp 220 from the NASA/IPAC Extragalactic Database (NED). Arp 220 is the most luminous object in the nearby universe (at $z = 0.018$) and is the most well-studied example of a ULIRG. It is necessary to use this low-redshift analogue of a SCUBA source since higher redshift sources have more sparsely sampled SEDs, due to the difficulty of observing them in multiple wavelength regions.

We use the Lagache, Dole & Puget [45] UV to radio SED models of a typical starburst galaxy to fill in the gaps in the data for Arp220. The Lagache, Dole & Puget [45]

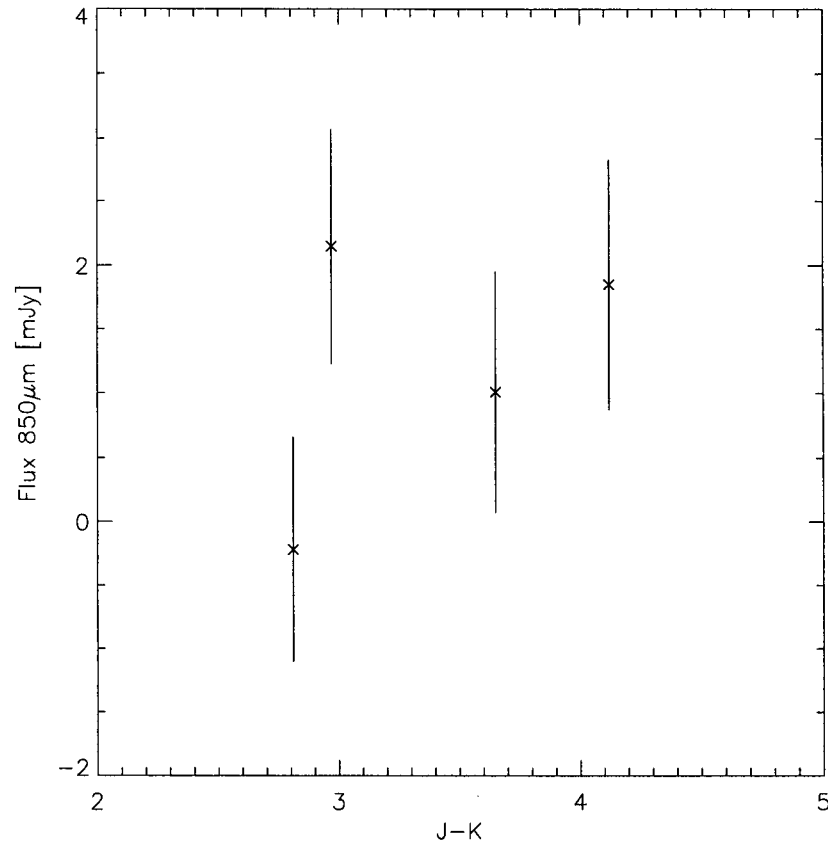


Figure 3.1: Is there a colour-flux correlation for the HEROs? We plot $850\ \mu\text{m}$ flux versus $J - K'$ colour. The best-fit line through these data has a slope of 0.81 ± 0.89 and a goodness-of-fit χ^2 value of 3.3, suggesting that there is no correlation between the measured $850\ \mu\text{m}$ submillimetre flux and IR colour in the case of the SDF HEROs.

templates evolve (become hotter) with luminosity over a range of luminosity levels from about $L = 10^9 - 10^{13}L_{\odot}$. These templates cover the range of bolometric luminosities of galaxies that comprise the Cosmic Infrared Background up to $z < 2$. For example, FIRBACK (Far InfraRed BACKground) sources comprise a cold nearby population with $L = 10^9 - 10^{11}L_{\odot}$ and a more distant ($z < 1.2$) cold (or warm and highly luminous) population with $L = 10^{12}L_{\odot}$. We employ their model number 30 (albeit heavily modified in terms of its dust content in the IR portion of the spectrum) in order to draw a smooth line through Arp220 (see Fig. 3.2). Fig. 3.3 shows that for the K' -band and at $850 \mu\text{m}$, the flux does not vary by more than about 10 per cent from the Lagache, Dole & Puget [45] template number 41, the most luminous template available.

We have constructed a three parameter model based on the SED of Arp220, constrained only by the K' magnitude and the $J - K'$ colour. We effectively redshift, dust extinct, and brighten the SED by known amounts and then read off the flux at $850 \mu\text{m}$. After choosing a redshift, we find the $J - K'$ colour and add dust to fix the colour to the observed value for each HERO. The model we have employed fits known sources even though it is very simple (one-parameter), and this gives it an advantage over more complicated multi-parameter models.

We add dust by multiplying our Arp220 template by an extinction function which varies with wavelength. We determine such an extinction law by constructing a power-law fit to the relative extinction values in the Landolt V , R , I and UKIRT J , H , K and L' bandpasses versus effective wavelength from Schlegel, Finkbeiner & Davis [53] (see Figs. 3.4 and 3.5). They employ a 'diffuse ISM' mean value of $R_V = 3.1$ for the extinction laws of Cardelli, Clayton & Mathis [10] and O'Donnell [47]. We note that the difference between the extinction curves of the Milky Way, the Magellanic Clouds and starburst galaxies is almost negligible at wavelengths longer than $\approx 0.26 \mu\text{m}$ (see Calzetti, Kinney & Storchi-Bergmann [9], Cardelli, Clayton & Mathis [10]). Therefore, using a different extinction law should not affect our results since only galaxies at redshifts of $z \lesssim 3$ are considered, corresponding to a rest wavelength of $0.31 \mu\text{m}$ being redshifted into the J -band.

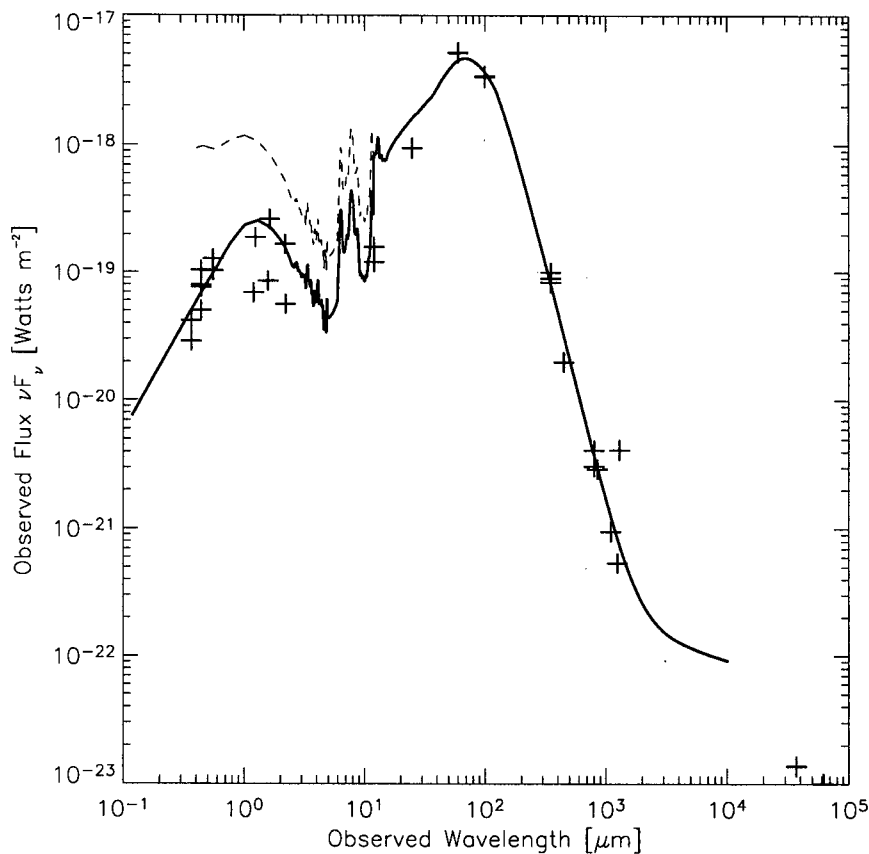


Figure 3.2: The model spectral energy distribution of a nearby ULIRG: the Lagache, Dole & Puget [45] starburst template (dashed line represents template number 30) fit at $z = 0.018$ to Arp220 photometric data (solid line), which are marked with the plus signs. The energy output is dominated by a modified blackbody and the mid-IR emission features seen here are attributed to PAH molecules. The slope of the drop at $\approx 1 \mu m$ in the original SED has been extrapolated to shorter wavelengths and fits an Arp220 *ROSAT* X-ray data point (not shown in the plot) within its error bar.

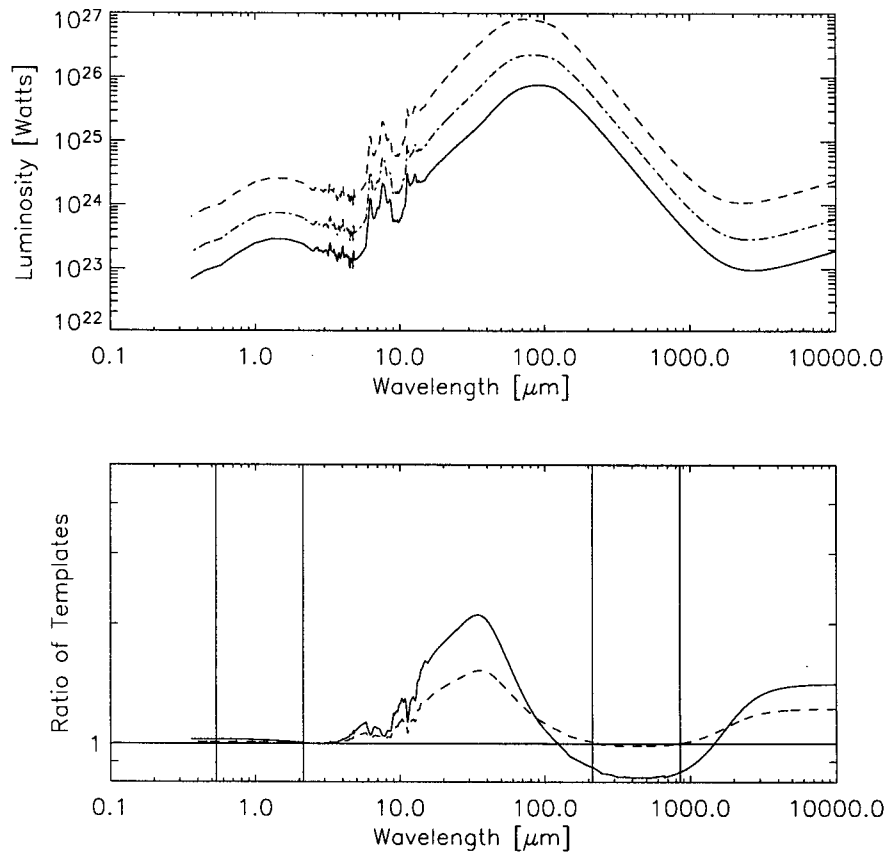


Figure 3.3: The upper panel shows 3 different luminosity templates from Lagache, Dole & Puget [45]. The lowest line is the template used for Arp220 (number 30), the middle line is template number 35, and the highest line is the brightest template available (number 41). The lower panel gives plots of the ratio of the Arp220 template with the other two higher luminosity templates. Note how the template SEDs actually change intrinsically in shape with luminosity. Vertical lines indicate the portion of the spectrum that we will be sampling over a redshift range $0 \leq z \leq 3$ at wavelengths of $850 \mu\text{m}$ and K' . For an observed band, the ratio of the K' -band to $850 \mu\text{m}$ flux does not vary by more than 10 per cent across the models chosen.

TABLE 6
RELATIVE EXTINCTION FOR SELECTED BANDPASSES

Filter	λ_{eff} (Å)	$A/A(V)$	$A/E(B-V)$	Filter	λ_{eff} Å	$A/A(V)$	$A/E(B-V)$
Landolt <i>U</i>	3372	1.664	5.434	Strömgren <i>u</i>	3502	1.602	5.231
Landolt <i>B</i>	4404	1.321	4.315	Strömgren <i>b</i>	4676	1.240	4.049
Landolt <i>V</i>	5428	1.015	3.315	Strömgren <i>v</i>	4127	1.394	4.552
Landolt <i>R</i>	6509	0.819	2.673	Strömgren β	4861	1.182	3.858
Landolt <i>I</i>	8090	0.594	1.940	Strömgren <i>y</i>	5479	1.004	3.277
CTIO <i>U</i>	3683	1.521	4.968	Sloan <i>u'</i>	3546	1.579	5.155
CTIO <i>B</i>	4393	1.324	4.325	Sloan <i>g'</i>	4925	1.161	3.793
CTIO <i>V</i>	5519	0.992	3.240	Sloan <i>r'</i>	6335	0.843	2.751
CTIO <i>R</i>	6602	0.807	2.634	Sloan <i>r'</i>	7799	0.639	2.086
CTIO <i>I</i>	8046	0.601	1.962	Sloan <i>z'</i>	9294	0.453	1.479
UKIRT <i>J</i>	12660	0.276	0.902	WFPC2 F300W	3047	1.791	5.849
UKIRT <i>H</i>	16732	0.176	0.576	WFPC2 F450W	4711	1.229	4.015
UKIRT <i>K</i>	22152	0.112	0.367	WFPC2 F555W	5498	0.996	3.252
UKIRT <i>L'</i>	38079	0.047	0.153	WFPC2 F606W	6042	0.885	2.889
Gunn <i>g</i>	5244	1.065	3.476	WFPC2 F702W	7068	0.746	2.435
Gunn <i>r</i>	6707	0.793	2.590	WFPC2 F814W	8066	0.597	1.948
Gunn <i>i</i>	7985	0.610	1.991	DSS-II <i>g</i>	4814	1.197	3.907
Gunn <i>z</i>	9055	0.472	1.540	DSS-II <i>r</i>	6571	0.811	2.649
Spinrad <i>R_s</i>	6993	0.755	2.467	DSS-II <i>i</i>	8183	0.580	1.893
APM <i>b_J</i>	4690	1.236	4.035				

NOTE.—Magnitudes of extinction evaluated in different passbands using the $R_V = 3.1$ extinction laws of Cardelli et al. 1989 and O'Donnell 1994. The final column normalizes the extinction to photoelectric measurements of $E(B-V)$.

Figure 3.4: We use the effective wavelengths (λ_{eff} column) and relative extinction values ($A/A(V)$ column) for the Landolt *V*, *R*, *I* and UKIRT *J*, *H*, *K* and *L'* bandpasses in order to construct an extinction law. This table has been extracted from Schlegel, Finkbeiner & Davis [53], and they employ a 'diffuse ISM' mean value of $R_V = 3.1$ for the extinction laws of Cardelli, Clayton & Mathis [10] and O'Donnell [47].

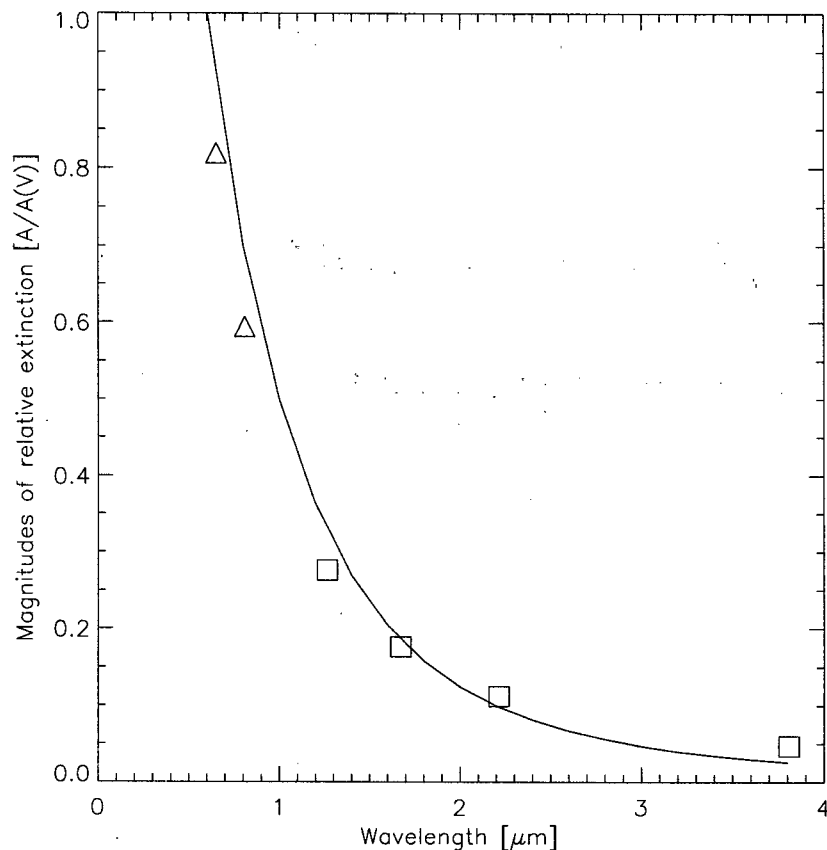


Figure 3.5: We plot the magnitudes of extinction relative to the V -band ($A/A(V)$) for the Landolt (triangles) and UKIRT (squares) bandpasses (see Fig. 3.4 for the complete table). We fit $2.5 \log(1/(1 + (\frac{1.23}{\lambda})^{2.6})^{0.2x})$ with $x = 1.0$ (i.e. $2.5 \log$ of Eqn. 3.1) to the data points (solid line). The values in the function were chosen arbitrarily to give a reasonable fit to the data points: 1.23 places the line at the correct vertical position relative to the points, 2.6 gives the correct line steepness to fit the data, and 0.2 places the graph in the correct horizontal location relative to the data points and also adjusts the line steepness to a lesser degree.

We redden the original template by a factor of:

$$\frac{1}{\left(1 + \left(\frac{1.23}{\lambda}\right)^{2.6}\right)^{0.2x}} \quad (3.1)$$

where x is our free parameter which adjusts the reddening (i.e. $J - K'$ colour) and λ is wavelength in microns. The function was fabricated to fit the relative extinction values of the Landolt and UKIRT bandpasses (which are similar enough to the Subaru bandpasses), and the values in the function were chosen arbitrarily to give the best fit to the data points (see caption of Fig. 3.5 for details). Choosing template number 30, redshifted to $z = 0.018$ and using a value of $x = 2.5$ in the equation above gives a good fit to the Arp220 photometric data (see Fig. 3.2 solid line).

We alter the luminosity of the template to fit the observed K' flux, as determined from the observed K' magnitude following Skinner [57]:

$$F_\nu = 10^{-0.4m} F_0, \quad (3.2)$$

where m is the magnitude and F_0 is the zero-point flux for the photometric band. The zero-point for the K' -band is $F_0 = 718.903$ Jy and was extracted from the interpolation of the broad-band flux of Vega (Motohara 2002, private communication).

We read off the observed $850 \mu\text{m}$ flux. For a given spectrum, the differential flux per unit frequency S_ν is related to the differential luminosity L_ν :

$$(\nu S_\nu)_{\text{obs}} = \frac{(\nu L_\nu)_{\text{em}}}{4\pi d_L^2}, \quad (3.3)$$

where d_L is the luminosity distance. Following Carroll, Press & Turner [11], the luminosity distance, d_L , in a flat Universe is derived from:

$$d_M = (1+z) \int_0^z \frac{c dz}{H(z)}, \quad (3.4)$$

with

$$H(z) = H_0 \{(1+z)^3 \Omega_M + \Omega_\Lambda\}^{1/2}, \quad (3.5)$$

and

$$\Omega_\Lambda = 1 - \Omega_M. \quad (3.6)$$

ID	Optical	S_{850} (mJy)	z_{spec}	z_{model}
SMMJ123628+621048	$I = 22.5, I - K = 4.0$	4.4 ± 1.2	1.013	1.2 ± 0.3
SMMJ123635+621239	$I = 22.3, I - K = 3.5$	3.0 ± 0.8	1.219	1.3 ± 0.3
SMMJ123652+621227	$I = 28.7, I - K = 5.2$	7.0 ± 0.5	4.1 ± 0.5	3.4 ± 0.1
SMMJ164502+4626.4	$I = 24.9, I - K \simeq 6.5$	4.9 ± 0.7	1.44	0.82 ± 0.1
FIRBACK FN1 40 (J1)	$I = 23.96, I - K = 4.23$	6.3 ± 1.4	0.449	1.8 ± 0.2

Table 3.1: Submillimetre sources with red IR colours and known redshifts. Model-predicted redshifts and errors (estimated using the errors in the $850 \mu\text{m}$ fluxes) are given in the last column.

We test this model on a number of red objects with measured IR colour, $850 \mu\text{m}$ flux and spectroscopic redshift to test whether we can reproduce these redshifts photometrically. We use an ERO and a VRO (very red object), two red objects from the Hubble Deep Field (HDF) with measured spectroscopic redshifts from the work of (Borys [6]). Also from the HDF, HDF850.1, detected by Hughes et al. [38] in the submillimetre, is a SCUBA-bright IR-faint ERO with a redshift deduced by Monte Carlo photometric redshift techniques from Dunlop et al. [24]. is also included in this test. We also include HR10 (or ERO J164502+4626.4, Dey et al. [17]), the first ERO discovered to be associated with a ULIRG, and FN1 40 (J1), discovered in the FIRBACK (Far InfraRed Background) survey (Dole [19]). See Table 3.1 for the IR colours, submillimetre fluxes, spectroscopic redshifts and predicted redshifts. The mean difference between the spectroscopic redshifts and model-estimated redshifts ($z_{\text{model}} - z_{\text{spec}}$) is $+0.06 \pm 0.8$. Fig. 3.6 illustrates how accurately the model predicts source redshifts by comparing model results to spectroscopically measured redshifts. We are therefore confident that this simple model is suitable for estimating redshifts of the reddest population of objects when the IR-colour and $850 \mu\text{m}$ flux are known.

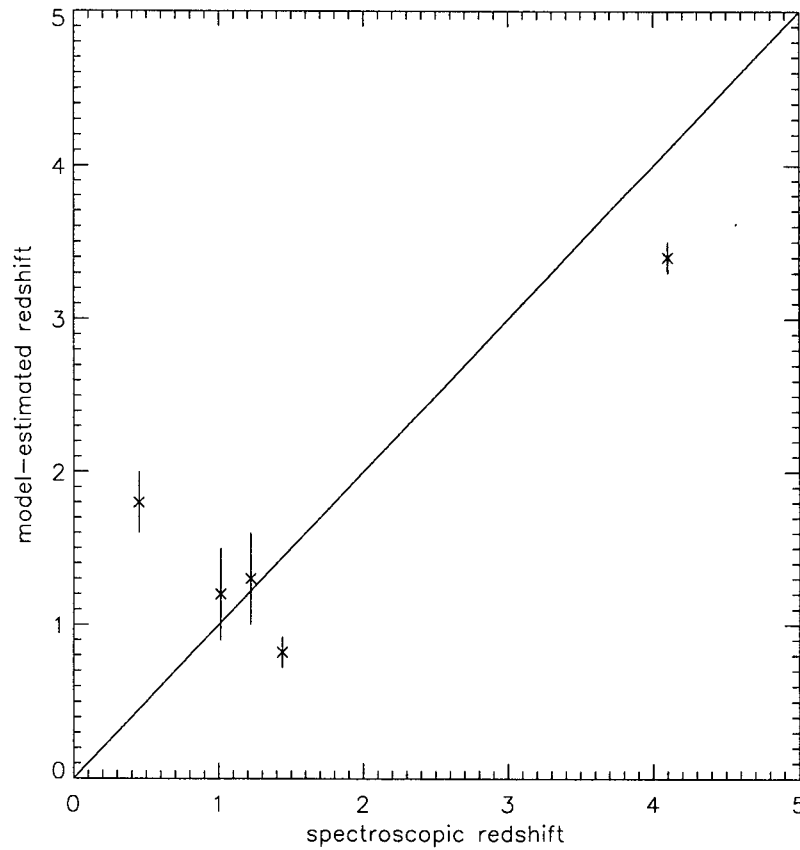


Figure 3.6: We plot model-estimated redshifts (with errors) against spectroscopic redshifts to see how well our model does for sources with known redshifts. Points falling on the line indicate a good correlation between the spectroscopic redshift and model-predicted redshift. On average, the mean difference between the spectroscopic redshifts and model-estimated redshifts ($z_{\text{model}} - z_{\text{spec}}$) is $+0.06$ with a spread of $\pm \sigma = 0.8$.

3.4 Using a NGC3938 as a Template

For comparison, we also created a normal spiral galaxy SED using NED public photometric data for NGC 3938. NGC 3938 is a well-studied, multiple-armed, early luminosity class Sc(s) face-on galaxy 10.8 Mpc away. We utilize the Lagache, Dole & Puget [45] template of a normal cold spiral galaxy to fill in the gaps in the photometric data in the same way as for Arp220. Unlike the starburst galaxy, the normal galaxy template of Lagache, Dole & Puget [45] does not evolve with luminosity, since the lack of data limits the constraints that can be placed on the model (Lagache 2003, private communication). We scale the template evenly across all wavelengths and add a small amount of dust ($x = 0.1$, c.f. Eqn 3.1) to the IR region of the spectrum to match the photometric data as closely as possible (see Fig. 3.7).

3.5 Results

We present the model-estimated redshifts derived from our analysis using the Arp220 and NGC3938 templates in Table 3.2.

3.6 Are the Models Feasible?

Here we perform a quick check to see that the flux level we measure for the HEROs is consistent with the number of HEROs found in the SDF. We then examine the model parameters such as dust content and luminosity that were chosen to satisfy the colour and K magnitude constraints at each redshift step (usually $\Delta z = 0.2$). If either of the starburst or normal galaxies are reasonable analogues of the HEROs then we would not need to add in an extraordinary amount of dust (i.e. more than a magnitude or 2 in J -band) nor brighten the template by an unreasonable amount (i.e. more than a factor of a few) at the redshift where the expected $850 \mu\text{m}$ flux matches the upper limit to the $850 \mu\text{m}$ observed flux.

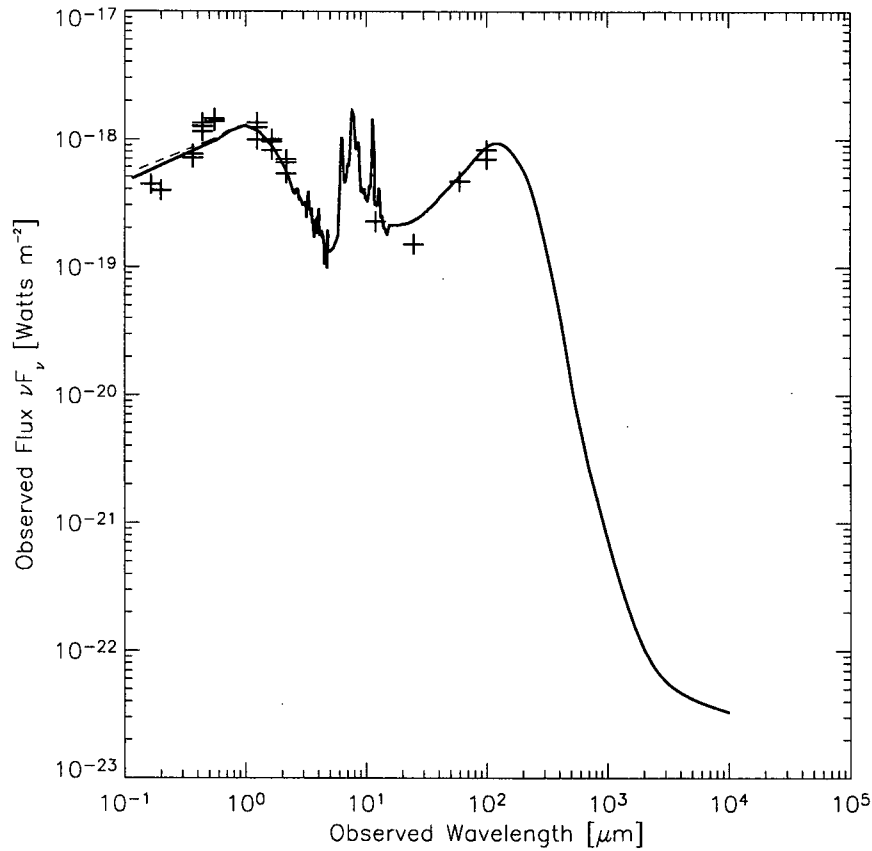


Figure 3.7: The model spectral energy distribution of a nearby normal spiral galaxy: the Lagache, Dole & Puget [45] normal galaxy template (dashed line represents template with no added dust) fit at $z = 0.002699$ to NGC3938 photometric data (solid line), which are marked with the plus signs. Again, the model SED has been extrapolated to shorter wavelengths.

ID	S_{450}	S_{850}	Upper Limits		
	(mJy)	(mJy)	S_{850}	z_{burst}	z_{spiral}
SDF1	1.47 (\pm 5.94)	2.15 (\pm 0.92)	< 3.46	< 1.65	< 1.79
SDF2	-7.84 (\pm 6.36)	1.01 (\pm 0.94)	< 2.64	< 1.65	< 1.77
SDF3	6.10 (\pm 6.48)	-0.22 (\pm 0.88)	< 1.63	< 1.83	< 1.97
SDF4	1.73 (\pm 5.76)	1.85 (\pm 0.98)	< 3.45	< 1.66	< 1.76
Mean	0.42 (\pm 3.06)	1.15 (\pm 0.46)	< 1.76	< 1.61	< 1.74

Table 3.2: Measured flux densities with errors and predicted redshift upper limits for the four SDF HERO sources. The fourth column lists the 95 per cent Bayesian upper limits (in mJy) at $850 \mu\text{m}$. The last two columns list the starburst galaxy and spiral galaxy model-estimated redshifts, respectively, based on the upper limit flux of each source. The bottom row lists the error-weighted mean of the $850 \mu\text{m}$ fluxes, the 95 per cent Bayesian upper confidence limit to this mean flux, and the model-estimated redshift based on this upper limit.

3.6.1 Number Counts of Submillimetre Sources

By looking at number counts of submillimetre sources above some threshold flux level we can predict how many sources we would see at the measured flux level of the HEROs. Based on interpolations from $850\ \mu\text{m}$ cumulative source counts (see Fig. 1.6) we expect to find $\approx 4 \pm 2$ sources brighter than some flux threshold S , which we observe to be $S > 1.76\ \text{mJy}$ (the 95 per cent upper limit to the average measured flux of the HEROs). So the flux level we measure for the HEROs is consistent with the number of HEROs in the SDF.

3.6.2 Could the HEROs be Starburst Galaxies?

We use the modified starburst template to create Fig. 3.8, a plot of expected $850\ \mu\text{m}$ flux as a function of redshift for a HERO which is representative of the whole population with the average colour and magnitude of the four-source sample.

Since we cannot claim detection above 3σ of any of our faint sources, Bayesian 95 per cent upper confidence limit flux estimates can be calculated for each source by integrating over the non-negative flux regions of a normalized Gaussian probability function. These upper flux limits were provided earlier in Table 3.2.

Combining the results from the four sources allows us to obtain an average object flux for our sample of HEROs. The error-weighted average flux density for the whole sample at $850\ \mu\text{m}$ is $1.15 \pm 0.46\ \text{mJy}$, and has a 95 per cent upper limit of $1.76\ \text{mJy}$. The average flux density at $450\ \mu\text{m}$ is $0.42 \pm 3.06\ \text{mJy}$.

When we force our template SED to match this same $850\ \mu\text{m}$ flux, constrained by a faint K' magnitude and very red $J - K'$ colour, we estimate a corresponding redshift of 1.6. This result is consistent with the median redshift estimates for SCUBA sources (see e.g. Dunlop [23]). Based on the assumption that hyper-extremely red objects are well-represented by an SED that fits Arp220, then they are at a redshift less than ≈ 1.6 .

Fig. 3.9 investigates how much we need to brighten the SED to get the correct K' magnitude after adding in an amount of dust to the Arp220 SED to get the correct

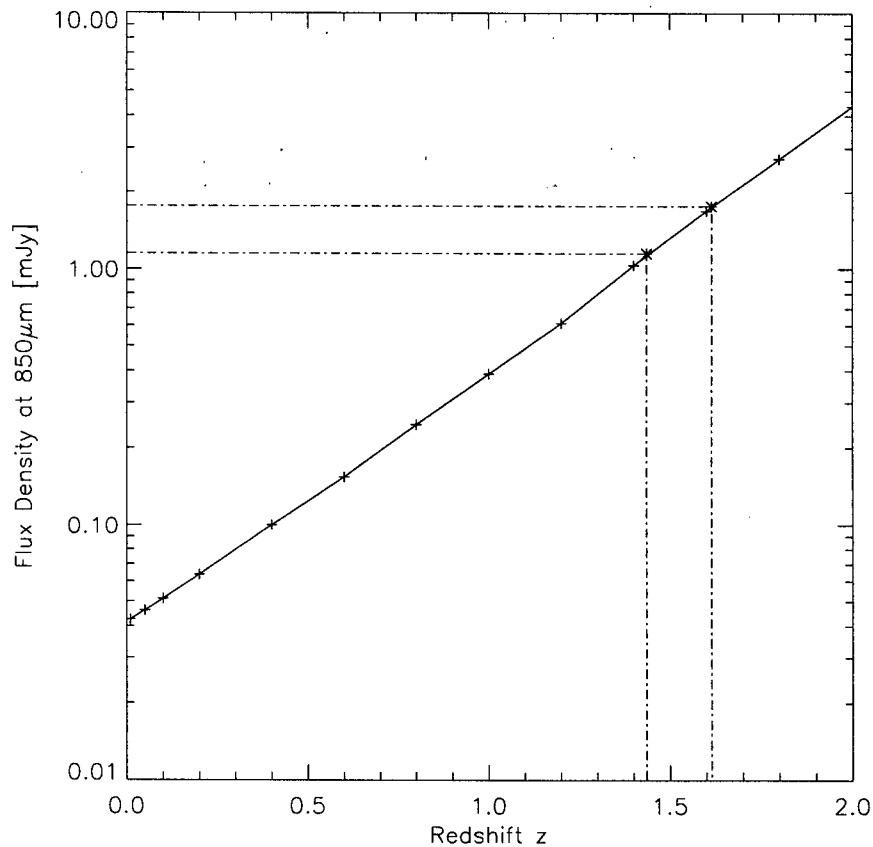


Figure 3.8: A plot of expected 850 μm versus redshift for our average HERO. Calculated data points are marked with plus signs and the asterisks represent where we read off a redshift, based on the mean and upper limit fluxes. We expect this semilog plot to have a linear shape since we add dust to the SED by applying a power-law function to the template. We expect a range of models to occupy a “band” around this line, predicting different flux levels for a given redshift.

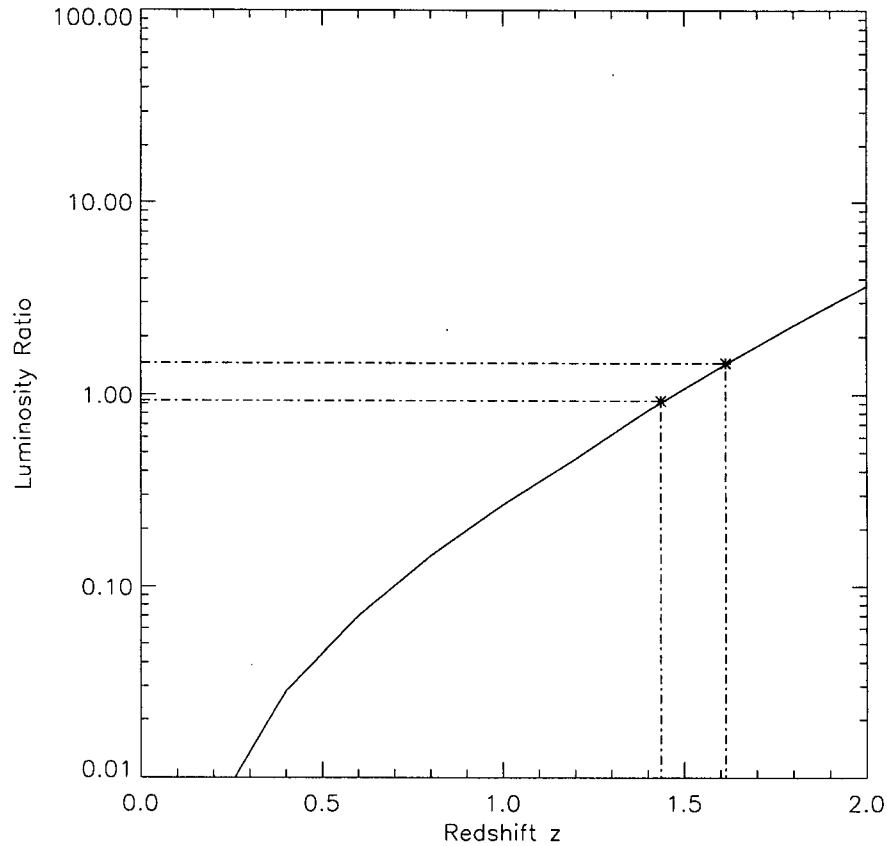


Figure 3.9: A plot of the brightness in the K' -band (giving the correct K' magnitude) compared to the brightness of Arp220 (after adding in the right amount of extra dust extinction included to obtain the observed $J - K'$ colour) versus redshift for our average HERO. Based on the assumption that this model describes the HEROs, then they are approximately as luminous as Arp220.

$J - K'$ colour. We notice that we need the K' flux to be dimmer than that of this 'dust-enriched' Arp220 until $z \simeq 1.5$, where the HERO starts becoming intrinsically brighter and more luminous than the dusty template. For $z \simeq 1.6$, we need to multiply the SED by a factor of $\simeq 1.5$ to get the correct K' magnitude for the HERO sample, which is reasonable (i.e. not brighter than a factor of a few) since we believe that more distant galaxies will be more intrinsically luminous (Blain et al. [3]). Even the brightest HERO in this sample, SDF1, only needs to be brightened by a factor of $\simeq 3$ at its upper redshift limit of $z \simeq 1.65$

Fig. 3.10 shows that the amount of dust reddening applied to the Arp220 SED in order to match $J - K'$ decreases with redshift. (Recall that our Arp220 template SED is comprised of Lagache et al.'s (2002) starburst template number 30 with dust added via equation (3.1) with $m = 0.5$). After $z \simeq 1$, the amount of required dust decreases very slowly but never reaches zero. The curves show an asymptotic behaviour, illustrating that some amount of dust extinction must always be applied to the SED. At $z \simeq 1.6$, we add in only ≈ 0.4 magnitudes in K' and ≈ 1.2 magnitudes in J . For the reddest HERO, SDF4, we need to add ≈ 1.8 magnitudes of dust in J at the upper redshift limit of $z = 1.66$. The HEROs could be about the same luminosity as Arp220 and only slightly more dusty.

Again, we stress that the model possesses an advantage over more complicated multi-parameter models in that it fits known sources well, despite its single-parameter simplicity. In Fig. 3.11, we compare our SED with that of Totani et al. [63] to get an idea of the amount of uncertainties in our model and which way a more sophisticated model would affect the results. We note that we must add about 1.80 magnitudes in J and 0.57 magnitudes in K' in order to obtain the correct colour of 4.12 at a redshift of $z = 2.3$. This results in a predicted $850 \mu\text{m}$ flux of $\simeq 0.5 \text{ mJy}$, close to predicted value of 1 mJy that Totani et al. [63] determined. In comparison, when we use the Arp220 SED and place it at this same redshift of $z = 2.3$ we predict a $850 \mu\text{m}$ flux of $\approx 20 \text{ mJy}$. This demonstrates how different redshifts will be inferred, given the large difference in the predicted $850 \mu\text{m}$ flux, depending entirely on the type of SED that is chosen. The result

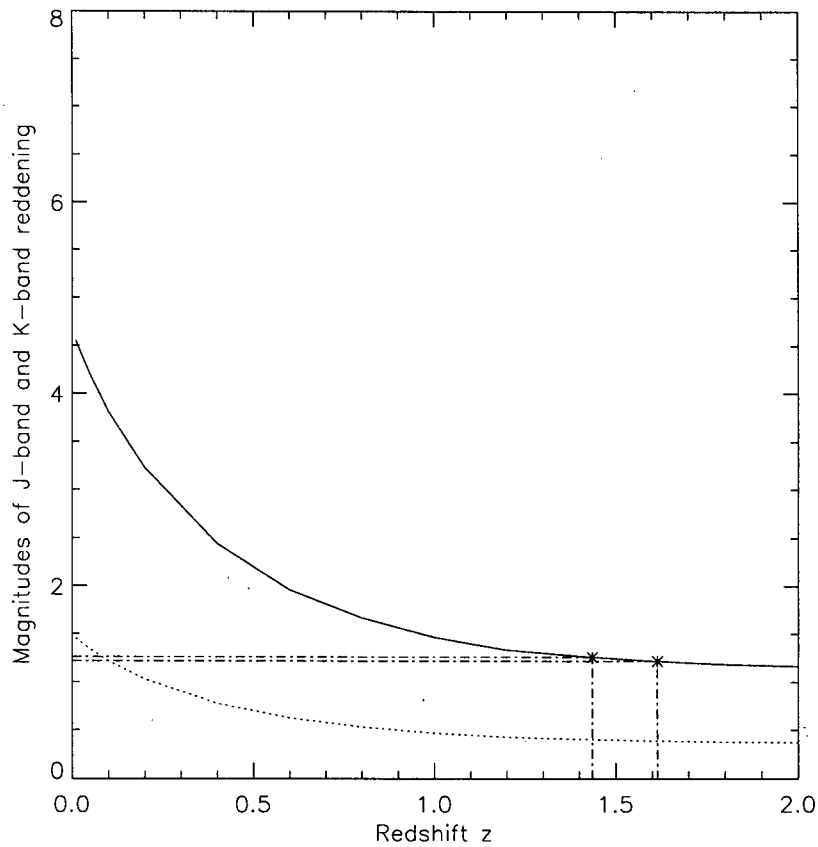


Figure 3.10: The amount of dust extinction that required to redden our we our template SED to match the data versus increasing inferred redshift at the J (solid line) and K' (dotted line) rest wavelengths. The curves display an asymptotic behaviour to values above zero, illustrating that some amount of dust extinction must always be applied to the SED.

of 0.5 mJy from the typical elliptical SED is plausible given our measured average HERO flux. The HEROs could in fact be typical dusty starburst galaxies at $z \simeq 2.3$ which formed at $z \simeq 3$ and are the progenitors of present-day giant ellipticals, as Totani et al. [63] suggest.

We make note here of some caveats with this model and address some issues. We have assumed that the far-IR luminosity does not increase or decrease as we alter the amount of dust or extinction in the optical/near-IR portion of the SED via equation 3.1. Performing numerical integration over the SED of Fig. 3.2 reveals that the total power absorbed in reddening the starburst galaxy template is only about 3 – 5 per cent of the total galactic emission. The small increase in the far-IR luminosity can be neglected as the reddening is altered.

We also scale the galaxy brightness uniformly across the spectrum, which inherently assumes that intrinsic properties such as temperature and density remain constant, which essentially has the effect of simply changing the physical size of the galaxy. The simple one-to-one relation between dust temperature and IR luminosity which is widely used empirically is also assumed here and is likely to break down for high-redshift galaxies from a theoretical standpoint (see Totani & Takeuchi [62]). Dust grains in a real galaxy always span a range of temperatures (20–200K), but in reality a large amount of it is cold (i.e. at the lower end of the 20–200K range). Therefore, the underlying assumption of a constant temperature seems reasonable here. The redshift upper limit would be weakened if the dust temperature was allowed to increase over a modest range. As alluded to earlier, high-redshift source SEDs may be systematically different, since primordial galaxies will contain smaller-sized and more chemically simpler dust which will heat up to higher temperatures due to the higher reflectivity and grain physics involved (see for e.g. Takeuchi et al. [61]).

Since the HEROs are extreme examples of EROs, it is useful to consider how the results would change by fitting an ERO-specific SED to the data aswell. HR10 was detected by Hu & Ridgway [37], has subsequently been well-studied at many wavelengths, and was the first ERO discovered to be associated with a ULIRG. Not suprisingly, the

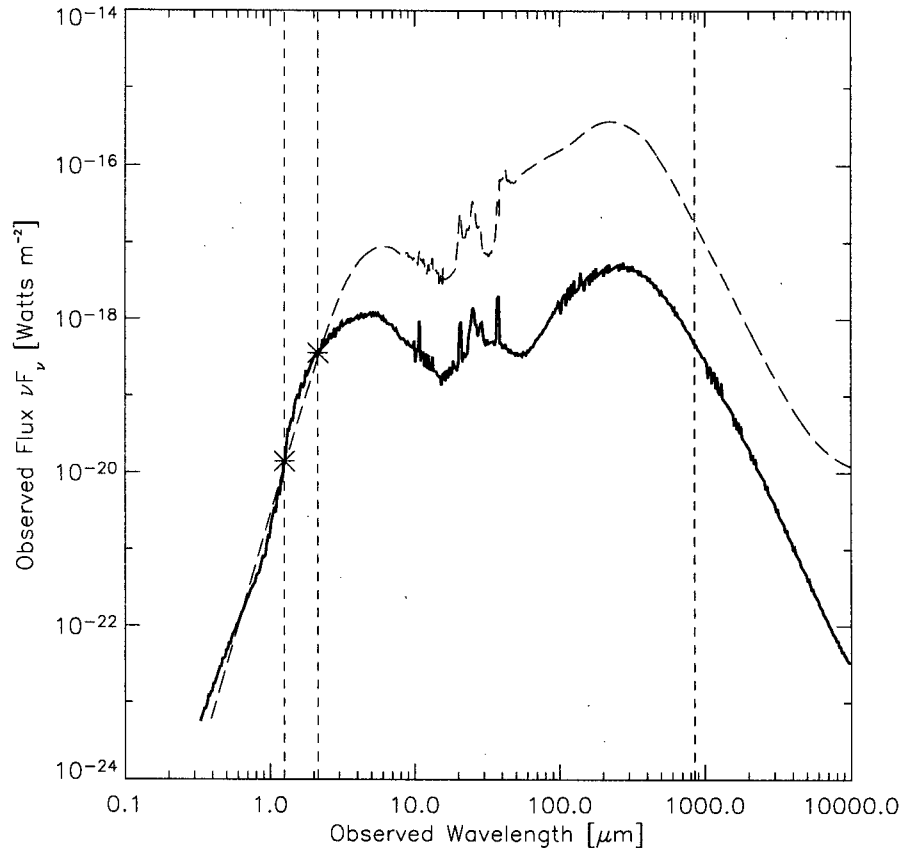


Figure 3.11: We scale and plot the Totani et al. [63] model of a typical elliptical galaxy with present-day absolute magnitude of $M_B = -20$, $J - K'$ colour of 4, and formation redshift $z_F = 3$ at a redshift of $z = 2.3$. The model contains emission from the direct stellar light that survived absorption by dust, as well as emission from heated dust. We scale the brightness to match the K -band brightness of SDF4 and adjust the $J - K'$ colour slightly to that of SDF4 (4.12) using our extinction law (c.f. Eqn. 3.1) (solid line). For comparison, we plot Arp220 (dashed line) at $z = 2.3$ and adjust the brightness and colour to match that of SDF4. The three vertical lines represent (from left to right), the J -band, the K' -band, and $850 \mu\text{m}$. This plot demonstrates how different redshifts will be inferred, given the large difference in the predicted $850 \mu\text{m}$ flux, depending entirely on the type of SED that is chosen.

SED for HR10 matches the SED shape of Arp220, a nearby ULIRG, but is brighter (i.e. more intrinsically luminous) by a factor of 3.8 (see Fig. 3.12 and Elbaz et al. [28]). HR10 lies at a redshift of $z = 1.44$ and is thought to be no more than a distant clone of Arp220. If we examine this template specific to EROs, and fit it to the HEROs, we find that the brightness factor is reduced to the HEROs being 0.34 times as bright as HR10 as opposed to being 1.3 times as bright as Arp220 at a redshift of 1.6.

Maihara et al. [46] state that the HEROs are likely to be remote galaxies, based on their “stellarity” indices and their apparent spatial extent. From the SDF K' -band image, we estimate the spatial extent of the HEROs to be between 1.2 to 2.0 arcsec in diameter. Based on this estimate from the image, if the HEROs are at $z \simeq 1.6$, then this would make them $\simeq 4 - 6.5$ kpc in size. This is consistent with the known range of galaxy sizes of 1 kpc up to 50 kpc.

3.6.3 Could the HEROs be Normal Spiral Galaxies?

We use the modified normal spiral galaxy template to create Fig. 3.8, a plot of expected $850 \mu\text{m}$ flux as a function of redshift for a HERO which is representative of the whole population with the average colour and magnitude of the four-source sample. As before, we use the Bayesian 95 per cent upper confidence limit flux estimates to derive the upper redshift limits listed in the last column of Table 3.2.

When we force our template SED to match the 95 per cent upper limit to the $850 \mu\text{m}$ flux of 1.76 mJy, constrained by a faint K' magnitude and very red $J - K'$ colour, we estimate a corresponding redshift of 1.74. Based on the assumption that hyper-extremely red objects are well-represented by an SED that fits NGC3938, then they are at a redshift less than $\simeq 1.74$.

Fig. 3.14 investigates how much we need to brighten the SED to get the correct K' magnitude after adding in an amount of dust to the NGC3938 SED to get the correct $J - K'$ colour. We notice that we need the K' flux to be dimmer than that of this ‘dust-enriched’ NGC3938 until $z \simeq 0.6$, where the HERO starts becoming intrinsically brighter

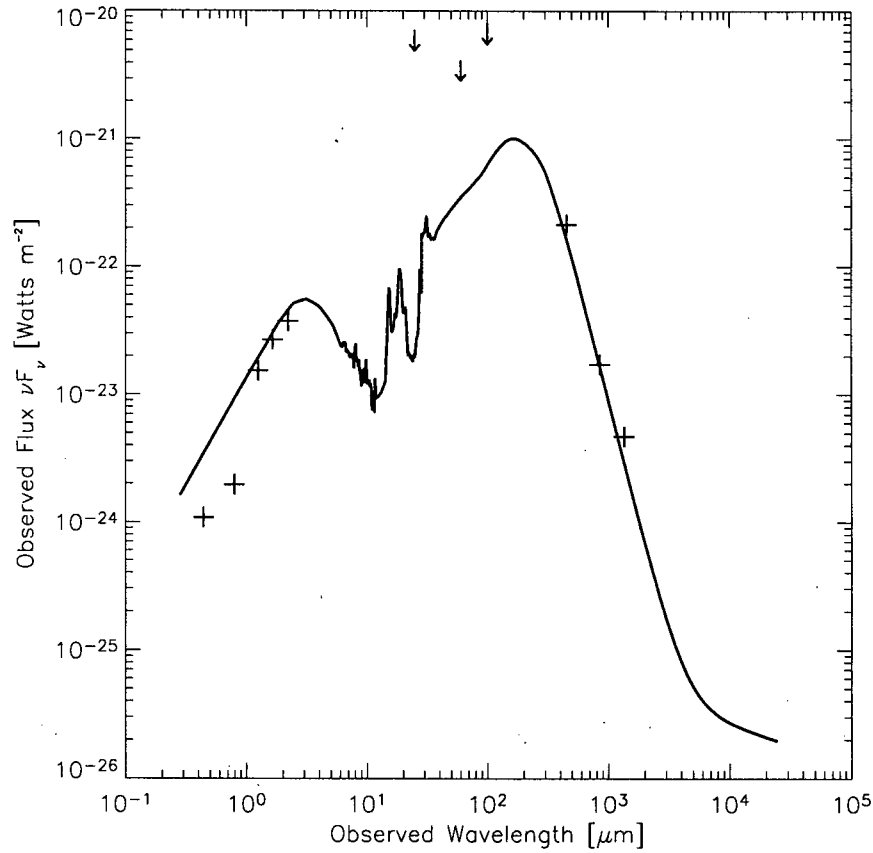


Figure 3.12: This is a model of HR10 based on an Arp220 SED brightened by a factor of 3.8 to fit the SED of HR10 at a redshift of $z = 1.44$. No dust has been added to this model. The crosses mark photometric data points and the arrows denote upper limit flux estimates from NED.

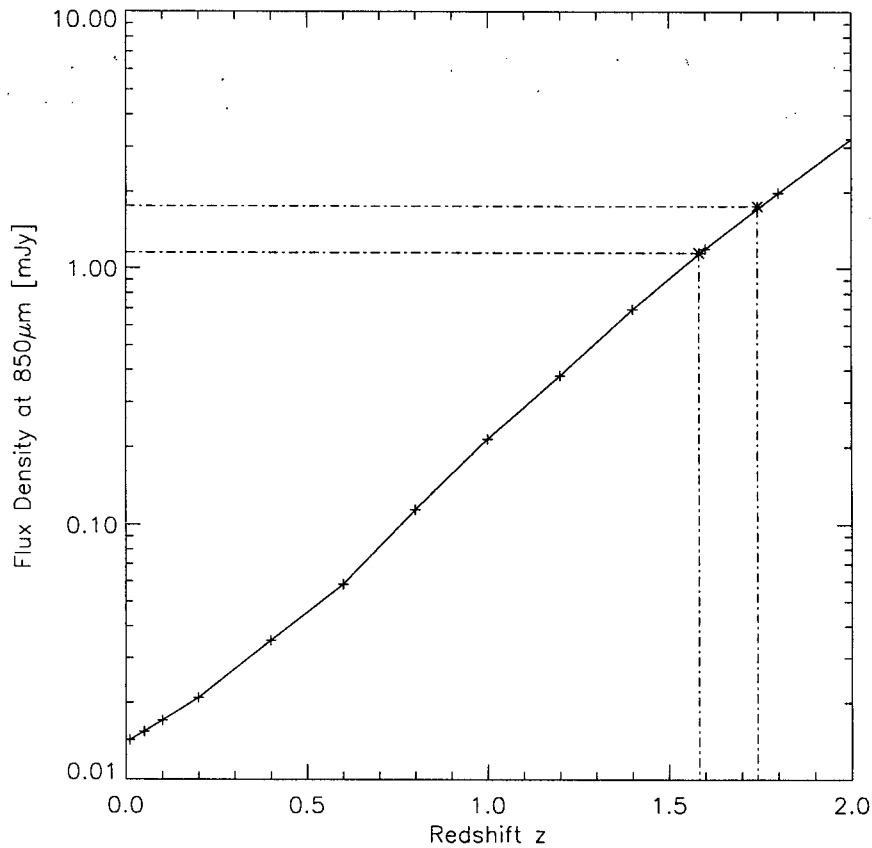


Figure 3.13: A plot of expected $850\mu\text{m}$ versus redshift for our average HERO, based on the normal spiral galaxy template. To reach a flux level of 1.76 mJy at $850\mu\text{m}$, the template must be moved out to $z \simeq 1.74$. Using the Arp220 SED, the template only needed to be moved out to $z \simeq 1.61$ in order to reach the same $850\mu\text{m}$ flux. Calculated data points are marked with plus signs and the asterisks represent where we read off a redshift, based on the mean and upper limit fluxes.

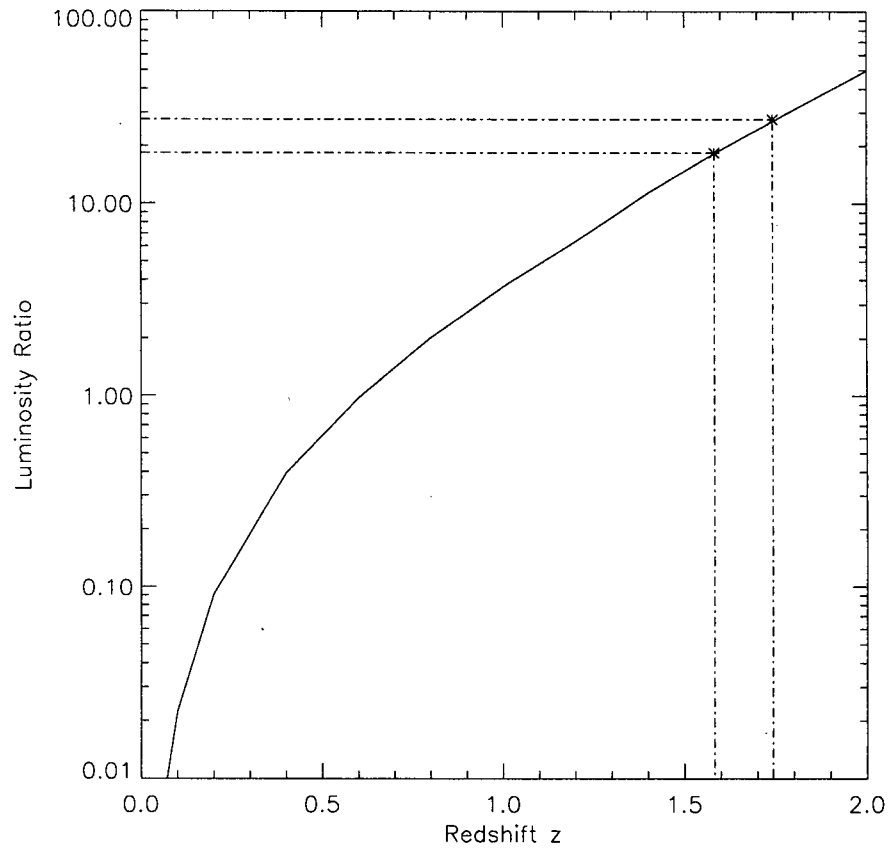


Figure 3.14: A plot of the brightness in the K' -band (giving the correct K' magnitude) compared to the brightness of spiral galaxy NGC3938 (after adding in the right amount of extra dust extinction included to obtain the observed $J - K'$ colour) versus redshift for our average HERO.

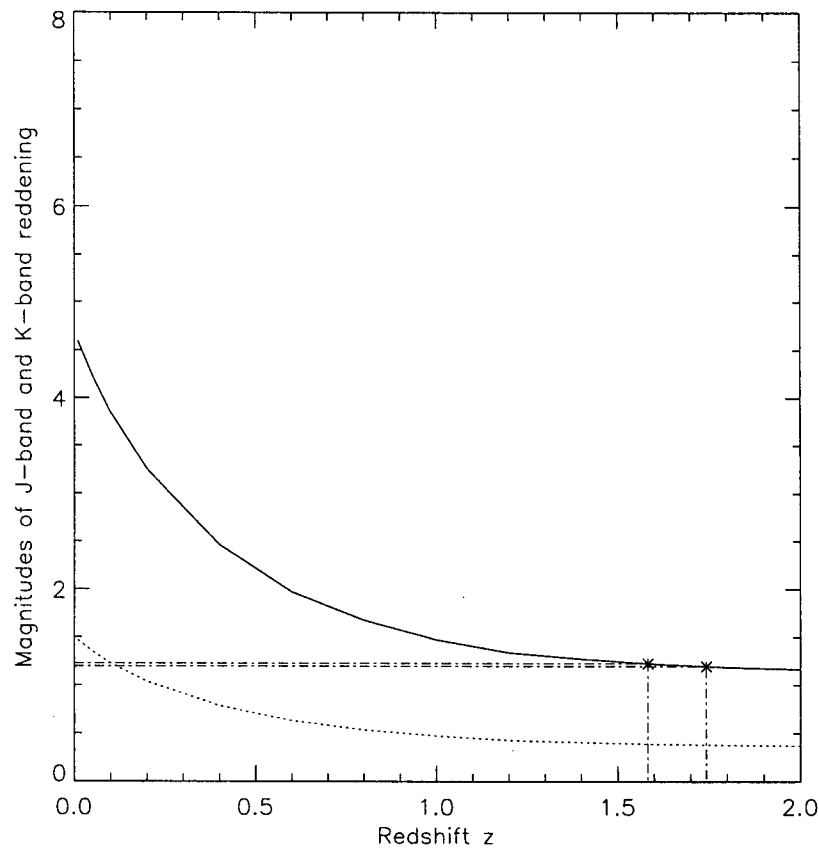


Figure 3.15: The amount of dust extinction that we must add to our normal galaxy SED template for increasing redshift at the J (solid line) and K' (dotted line) rest wavelengths.

and more luminous than the dusty template. For $z \simeq 1.7$, we need to multiply the SED by a factor of $\simeq 30$ to get the correct K' magnitude for the HERO sample. The brightest HERO, SDF1, requires the SED to be brightened by a factor of 60 at its upper redshift limit of $z = 1.79$.

Fig. 3.7 reveals the energetics of the normal cold spiral galaxy, and it is clear that there is just as much power in the near-IR peak as in the far-IR peak. This was not the case in the starburst galaxy template, where the far-IR peak dominated the energy output of the galaxy. With this in mind, it is clear that for such galaxies we cannot

ignore the effect of dust extinction on the total power of the galaxy. The power that would be “lost” due to reddening the spiral galaxy must be added back into the far-IR region of the spectrum in order to conserve energy. We calculate the total power of the galaxy before adding dust, and calculate the power in both the far-IR and near-IR peaks after adding some dust to the galaxy. We subtract the power in the near-IR peak from the total power “before dust” to find the amount of energy that must be elsewhere in the spectrum in order to conserve energy. We achieve this by first splitting the spectrum into two different components (the near-IR bump and the far-IR bump) and multiplying each bump by a smooth function of the form:

$$f_1(x) = e^{(\frac{\lambda}{\lambda_*})^n} \quad (3.7)$$

for a decreasing exponential, or

$$f_2(x) = 1 - e^{(\frac{\lambda}{\lambda_*})^n} \quad (3.8)$$

for an increasing exponential. λ_* is the cut-off wavelength where the function drops off steeply and n controls the steepness of the function’s drop-off (we choose a large enough value, $n = 20$, to get sufficient steepness). Subsequently, we add the two components back together to create one unified template. We take the ratio of the “missing power” (i.e. the power not in the near-IR peak) to the amount of energy in the far-IR to find the far-IR “boosting” factor. Multiplying the far-IR bump by this factor effectively moves the entire far-IR νF_ν spectrum up by the same amount. By conserving energy in this way, the total power absorbed in reddening the galaxy is extremely negligible. Even though this scaling method is rather crude, it avoids changing the temperature and other intrinsic physics of the galaxy.

Fig. 3.15 shows that the amount of dust reddening applied to the NGC3938 SED in order to match $J - K'$ decreases with redshift. (Recall that our NGC3938 template SED is comprised of Lagache et al.’s (2002) normal cold spiral galaxy template with dust added via Eqn (3.1) with $x = 0.1$). After $z \simeq 1$, the amount of required dust decreases very slowly. At $z = 1.74$, we add in only ≈ 0.7 magnitudes in K' and ≈ 1.2 magnitudes

in J . For the reddest HERO, SDF4, we need to add ≈ 1.8 magnitudes of dust in J at the upper redshift limit of $z = 1.76$

NGC3938 is not a reasonable analogue for the HEROs, since we need to brighten the galaxy by an extraordinary amount to fit the entire SED (i.e. more than a factor of a few). An $850\ \mu\text{m}$ flux of 1.76 mJy indicates that the galaxy lies at $z = 1.74$, the galaxy would need to be intrinsically brighter by a factor of about 30 compared with a normal spiral galaxy, not a very realistic scenario for this type of galaxy. The possibility of the HEROs being normal spiral galaxies is therefore eliminated. Even if NGC3938 was at a lower redshift and would therefore not need to be brightened by such a large factor, we would need to add in more dust than would be reasonable (i.e. more than one or two magnitudes of extinction in J , c.f. Fig. 3.15). If the flux is just above the confusion limit at $\simeq 0.6$ mJy then the redshift is about $z \simeq 1.3$ and the galaxy would be still need to be brighter than NGC3938 by a factor of 8 and contain about 1.3 magnitudes of extinction in J -band.

CHAPTER 4

SDF SOURCES

An image is “confused” when multiple unresolved faint objects cluster in one beam-size. As we look fainter and fainter, dim objects become more numerous, superimposing their signals on each other, until the confusion limit is reached. We investigate the number of pixels within a certain flux level in Fig. 4.1, a histogram of the number of pixels at each flux level in the $850\ \mu\text{m}$ SDF map. The positively skewed non-Gaussian single peak distribution of flux demonstrates that a population of submillimetre sources lies in the positive tail of the distribution, below the confusion limit of these data (Condon [15]). If we subtract the flux bins reflected about 0 mJy from the original flux bins, this effect becomes apparent (see Fig. 4.2). We can therefore infer that a population of sources lies just below the confusion limit of the $850\ \mu\text{m}$ SDF map. Figs. 4.3 and 4.4 demonstrate this also for the $450\ \mu\text{m}$ map. This result hints that we are detecting submillimetre emission from the SDF and that it could be correlated with SDF data in another wavelength region.

4.1 Correlating the IR Galaxies with the Submillimetre Data

Kashikawa et al. [43] have constructed a deep K' -band selected B, V, R, I, z', J, K' multi-colour sample of 439 galaxies ($K' < 24.0$) in the Subaru Deep Field and estimated a photometric redshift for each galaxy using the public domain HYPERZ code written by Bolzonella, Miralles & Pello [5]. HYPERZ finds the redshift of a galaxy using a standard SED fitting procedure, i.e. comparing the observed magnitudes with those computed from template SEDs. Throughout this thesis we use the more complete, unpublished 526 K' -selected galaxy catalogue based on the criterion of $K'_{\text{isophot}} < 24.6$ (Kashikawa 2002, private communication). In Fig. 4.5, we plot the mean of the 20 brightest K' -band

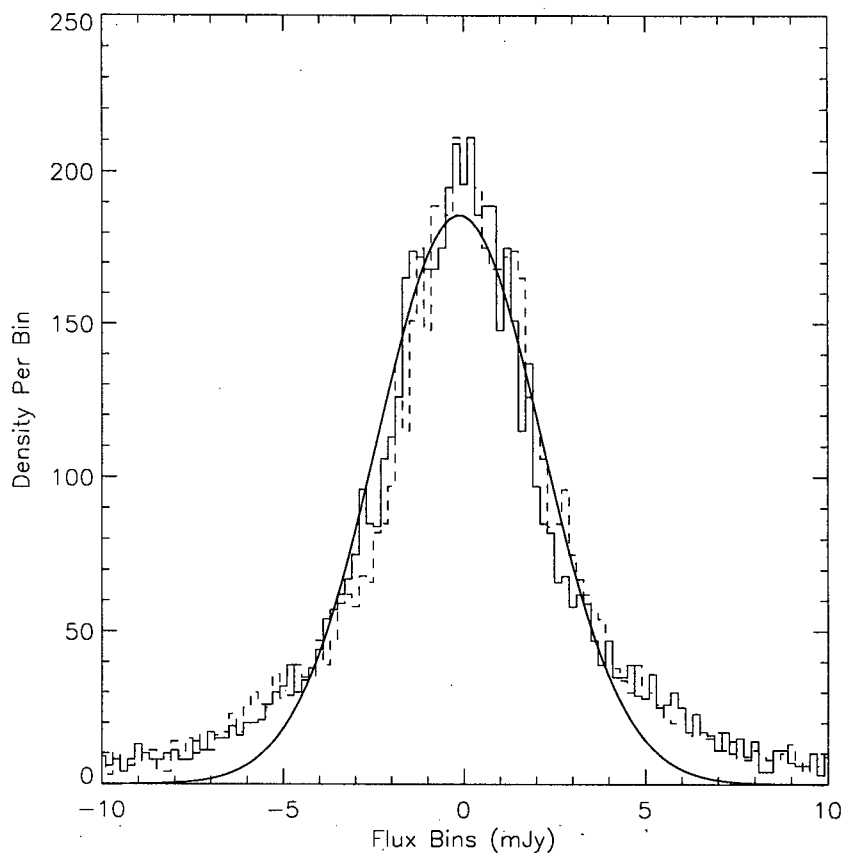


Figure 4.1: We plot the number of pixels at each brightness level in the $850\ \mu\text{m}$ map as a histogram with 100 bins of width $0.2\ \text{mJy}$ (solid jagged line). The overlaid dashed histogram represents the flux bins reflected about $0\ \text{mJy}$, demonstrating that there is clearly more positive flux in the map than negative flux. The flux distribution is clearly non-Gaussian and has enhanced high and low flux tails when compared to the overlaid Gaussian. The Gaussian fit to the data (smooth solid line) has a height of 186 ± 0.27 , center of -0.12 ± 2.3 , and a half-width half-maximum of 2.26 ± 0.004 .

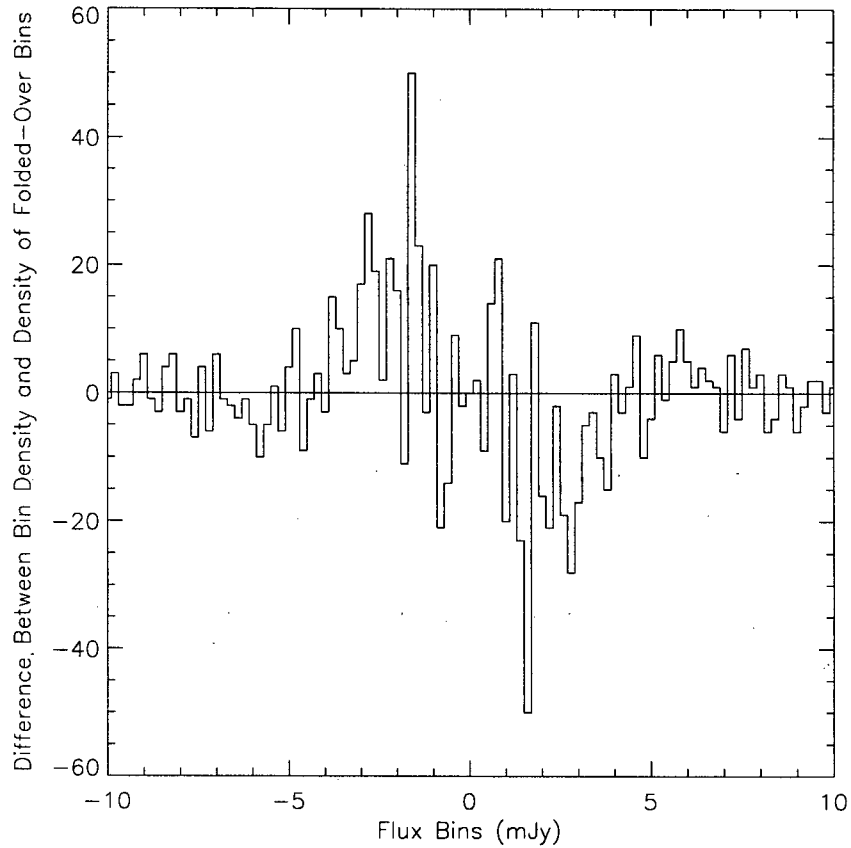


Figure 4.2: We plot the difference of the flux bins and the flux bins reflected about 0 mJy. If we take the difference between a positively skewed single peaked distribution and its reflection about 0 mJy, we reproduce this result. We can therefore infer a population of sources lying just below the confusion limit of the $850\ \mu\text{m}$ map.

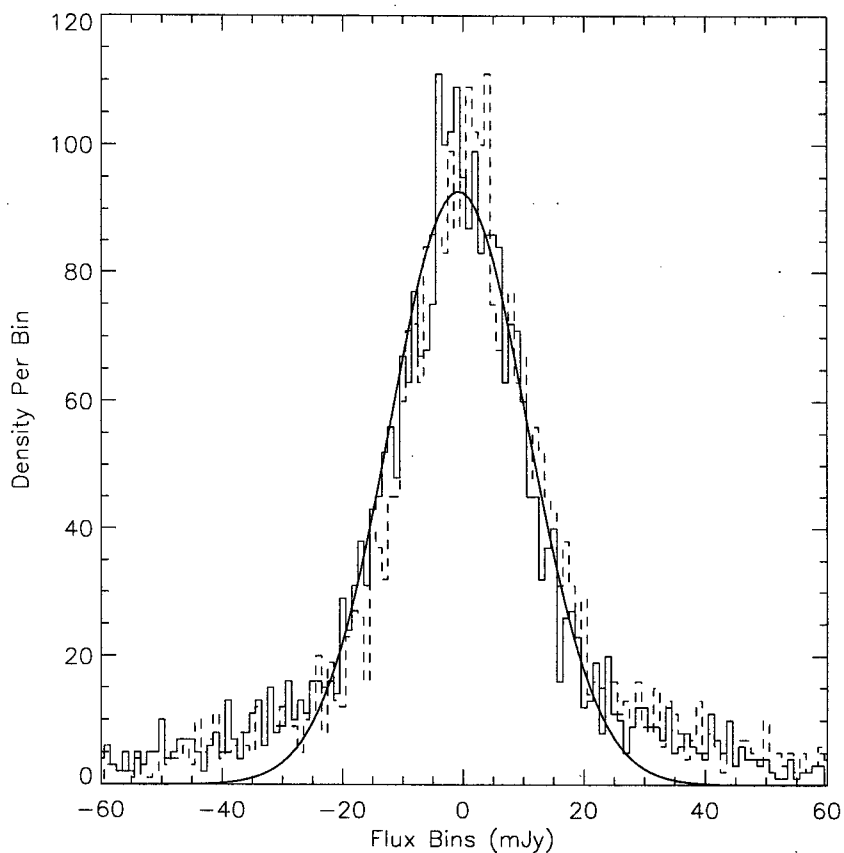


Figure 4.3: We plot the number of pixels at each brightness level in the $450\ \mu\text{m}$ map as a histogram with 120 bins of width 1.0 mJy (solid jagged line). The overlaid dashed histogram represents the flux bins reflected about 0 mJy, demonstrating that there is clearly more positive flux in the map than negative flux. The flux distribution is clearly non-Gaussian and has enhanced high and low flux tails when compared to the overlaid Gaussian. The Gaussian fit to the data (smooth solid line) has a height of 93 ± 0.27 , center of -0.73 ± 0.04 , and a half-width half-maximum of 11.4 ± 0.04 .

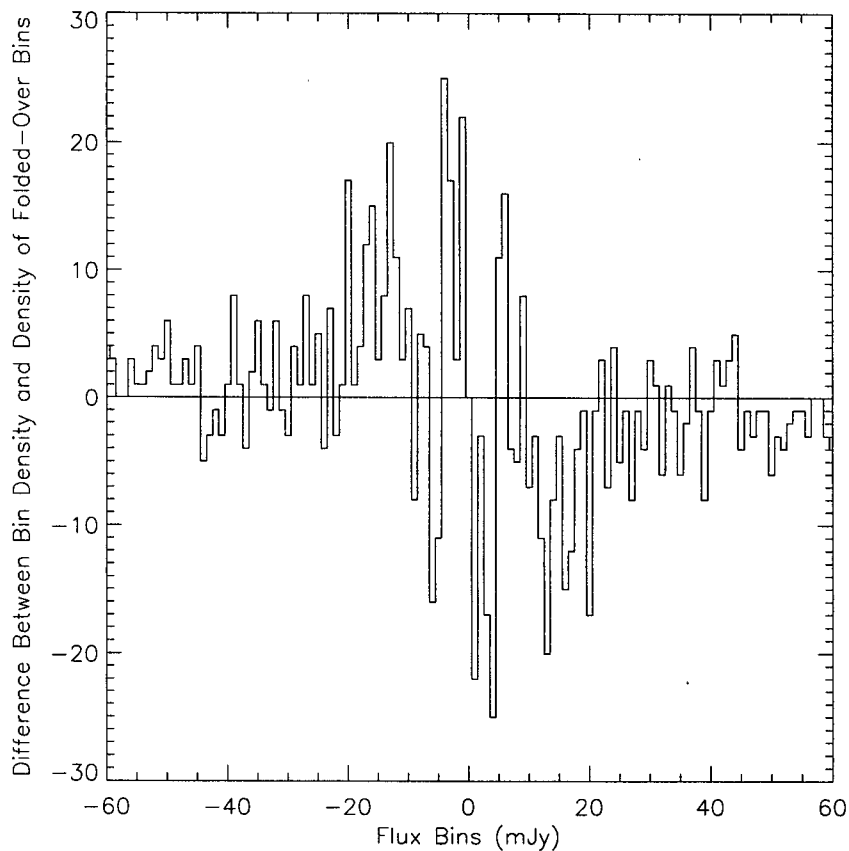


Figure 4.4: We plot the difference of the flux bins and the flux bins reflected about 0 mJy. If we take the difference between a positively skewed single peaked distribution and its reflection about 0 mJy, we reproduce this result. We can therefore infer a population of sources lying just below the confusion limit of the $450 \mu\text{m}$ map.

objects in redshift bins of 0.5 width¹, and observe that the faintest K' -band objects are also at the highest redshifts. It is interesting to investigate the measured submillimetre emission of the K' -selected galaxies as a function of redshift, since it can potentially reveal if amounts of hidden star formation evolve with redshift. Peacock et al. [48] have performed a similar analysis with ultraviolet positional information for the Hubble Deep Field and found little correlation at $z < 1$, but a definite positive signal spread out over higher redshift bins ($z > 2.5$). This demonstrates that their submillimetre map of the HDF receives emission from galaxies over a wide range of redshifts.

A K -band source which is very faint or undetected in optical data (i.e. J or I -band) holds a strong possibility of being SCUBA bright – or at least we know the converse to be true. We currently do not know how to predict which EROs will be SCUBA-bright. We would like to test if faint near-IR emission is correlated with submillimetre emission. We might expect higher redshifted near-IR objects to be stronger submillimetre sources, since the far-IR peak of the SED will be significantly shifted into the submillimetre regime. The best way to see if we are detecting IR-galaxy emission statistically in the $850\ \mu\text{m}$ map is to measure the flux density at the location of each galaxy and look for a correlation. We take the value from the map at the position of each IR source as the best estimate of its $850\ \mu\text{m}$ flux density. These flux densities are then averaged or “stacked” into redshift bins (see Fig. 4.6). We also perform the same analysis on the $450\ \mu\text{m}$ map (see Fig 4.7).

By dividing the maps up into redshift slices, we can now see if one redshift band tends to dominate more in the submillimetre than another. In order to quantify the degree of correlation we use the linear Pearson correlation coefficient, a number between -1 and $+1$ which measures the degree to which two variables are linearly related using a least-squares fit. A value of 0 indicates no correlation and values of -1 and $+1$ indicate a strong correlation (inverse proportionality and direct proportionality, respectively). We weight the mean fluxes by a factor of $1/\sigma^2$ (σ is the error bar on each bin) in order to take the error bars into account before computing the correlation coefficient. We obtain

¹We choose the number of bins and the bin occupancy based on the best compromise between noise reduction and a sensible number of points.

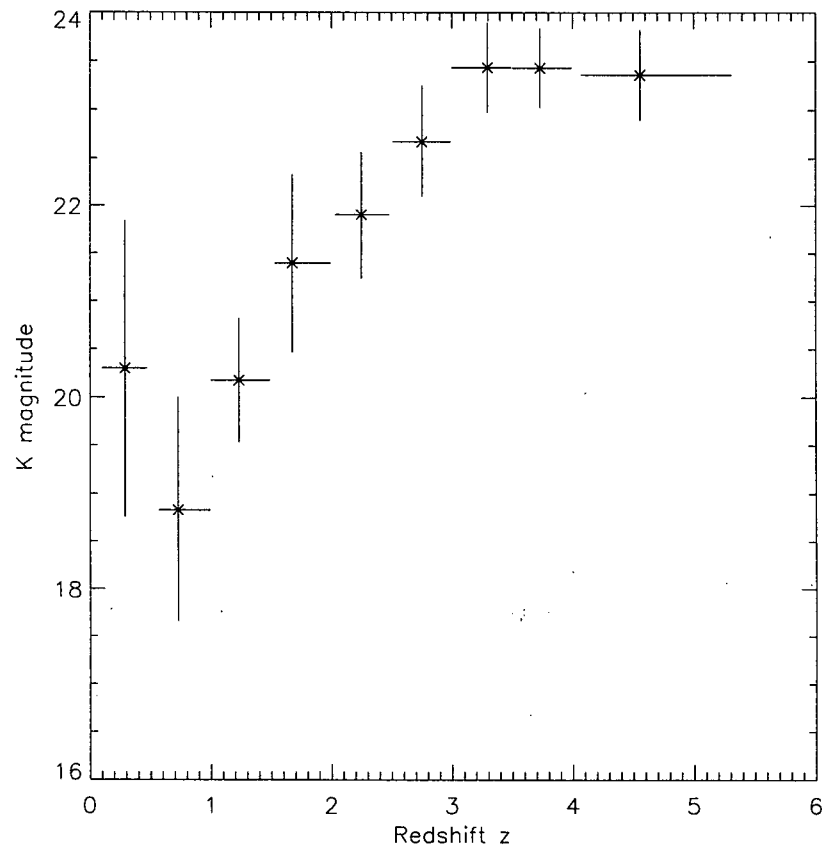


Figure 4.5: A plot of the 20 brightest K' -band objects per redshift bin. The vertical error bars show the 1σ standard deviation of the K' magnitudes in each redshift bin. The asterisks mark the mean redshift of each bin and the horizontal error bars represent the coverage of each redshift bin. The 7th bin only contains 14 objects due to the low number of objects in this redshift bin. We remark that the the faintest K' -band objects also have the highest photometric redshifts.

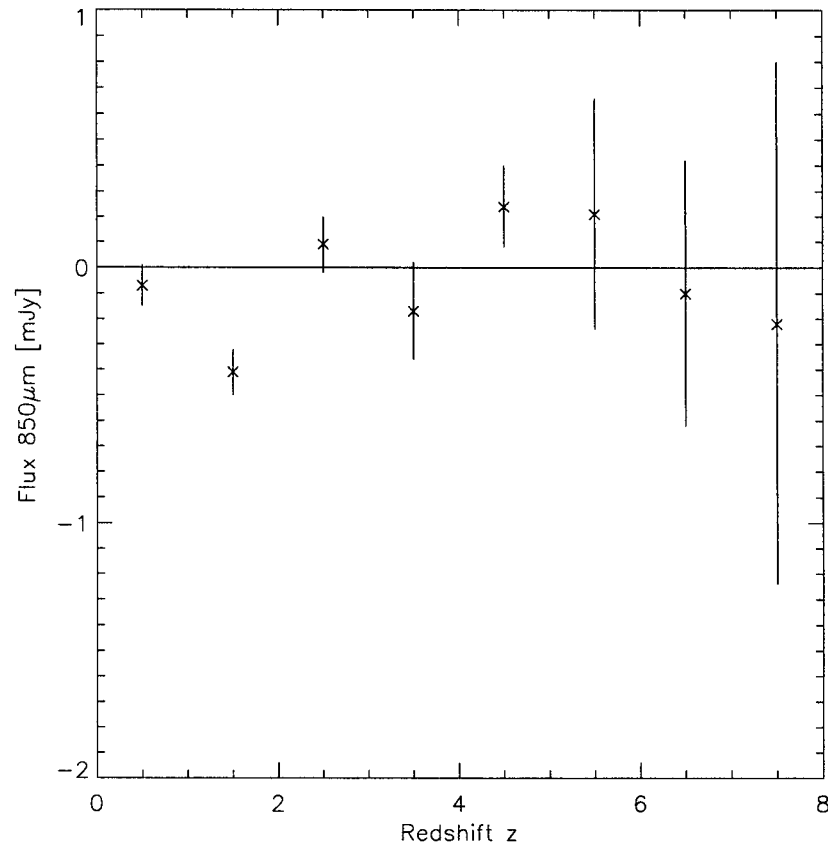


Figure 4.6: A plot of observed average $850\ \mu\text{m}$ flux per redshift bin ($\Delta z = 1$). Starting with the lowest redshift bin, the number of galaxies contained in each bin is 183, 150, 100, 36, 46, 6, 4, 1. It is evident that the highest redshift bins contain the smallest number of objects and so will have the largest error bars. The lowest redshift bins contain a large number of objects and so the average flux will tend to be closer to 0 mJy, since the measurement is beginning to be constrained by the map average.

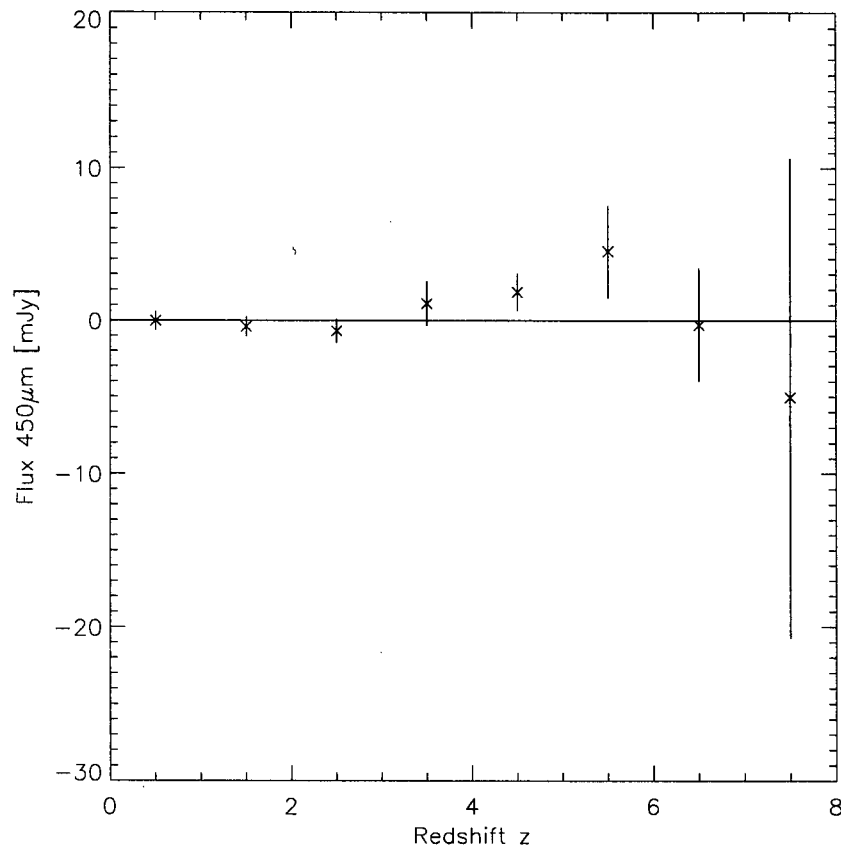


Figure 4.7: A plot of observed average $450 \mu\text{m}$ flux per redshift bin ($\Delta z = 1$). Starting with the lowest redshift bin, the number of galaxies contained in each bin is 183, 150, 100, 36, 46, 6, 4, 1. It is evident that the highest redshift bins contain the smallest number of objects and so will have the largest error bars. The lowest redshift bins contain a large number of objects and so the average flux will tend to be closer to 0 mJy, since the measurement is beginning to be constrained by the average of the map.

correlation coefficients of 0.49 and 0.38 at 850 and 450 μm respectively.

In order to see how likely it is to achieve these outcomes and correlation coefficients simply by chance, we perform 1000 statistical Monte Carlo simulations of this procedure (see Figs. 4.8, 4.9, 4.10, 4.11). The Monte Carlo simulation selects positions (the same number of times as there are objects in the bin) from the SDF map at random and measures the flux there. For each bin, we calculate the mean and error, again weighting the measurements by the corresponding value on the noise map. We calculate a correlation coefficient between the error-weighted ($1/\sigma^2$) mean flux and redshift bin for a complete set of redshift bins and repeat the whole procedure 1000 times in order to get a well-defined distribution of correlation coefficients. It is now possible to estimate how likely it is to obtain a certain correlation coefficient at random.

Looking at these plots, getting a correlation coefficient of 0.49 or higher by chance occurs about 80 per cent of the time for the 850 μm map and getting a coefficient of 0.38 or higher by chance occurs about 40 per cent of the time for the 450 μm map. From these results, there is no strong case for a correlation between the stacked submillimetre fluxes and redshift. Although there does seem to be a hint of positive flux spread over the redshift range $3 < z < 6$ in the 450 μm map (see Fig. 4.7), these results suggest that the flux we detect in the submillimetre is not well-described by the K' -band galaxy photometric redshifts.

Because the first few bins each contain a large number of objects, we are inherently just taking the average of the map, and we therefore expect a stacked flux close to 0 mJy. The bins with fewer objects will inherently possess very large error bars, as they suffer from small number statistics. It is therefore more useful to rebin the objects into bins with an equal number of objects. We redo the analysis for Figs. 4.6 and 4.7 but instead divide the objects into bins with equal numbers of objects to see if this makes a trend visible (see Figs. 4.12 and 4.13). We get correlation coefficients of 0.40 and 0.43 for the 850 and 450 μm data-sets, respectively. We perform 1000 Monte Carlo simulations again (see Figs. 4.14 and 4.16), but this time with an equal number of objects per bin²,

²All bins contain 40 objects except for the last bin which contains 46 objects, mimicking how the real

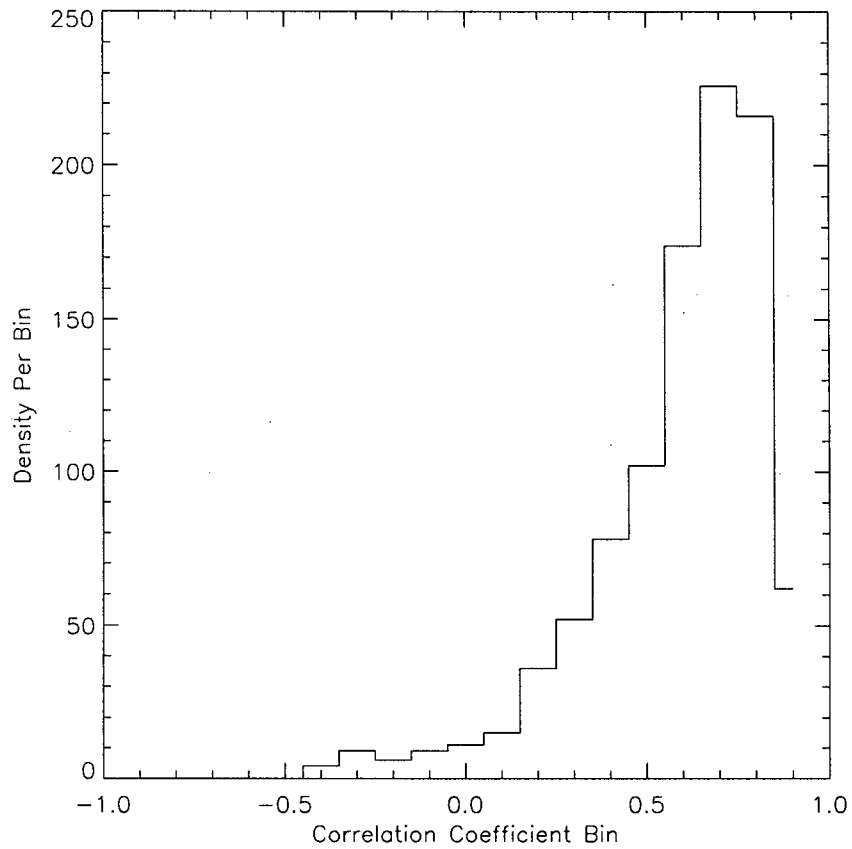


Figure 4.8: This plot shows the distribution of correlation coefficients obtained from $850\ \mu\text{m}$ stacked fluxes versus redshift for a set of Monte Carlo simulations of stacked $850\ \mu\text{m}$ flux in redshift bins of $\Delta z = 1$.

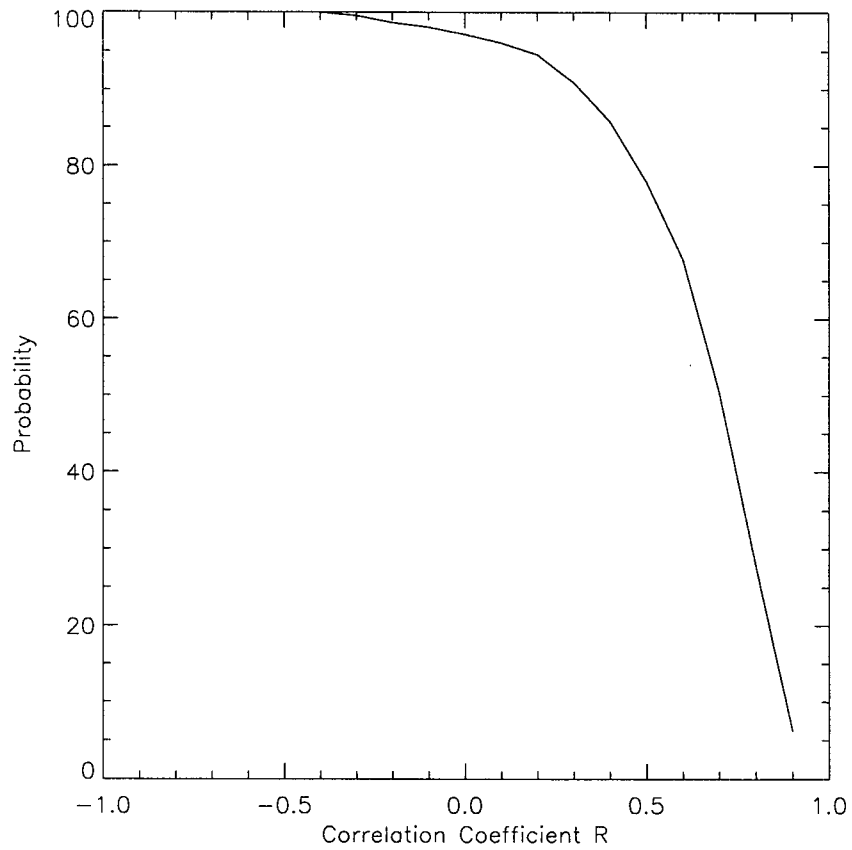


Figure 4.9: This plot shows how many times a correlation coefficient is obtained for the $850\ \mu\text{m}$ stacked fluxes versus redshift from a set of Monte Carlo simulations of stacked $850\ \mu\text{m}$ flux in redshift bins of $\Delta z = 1$.

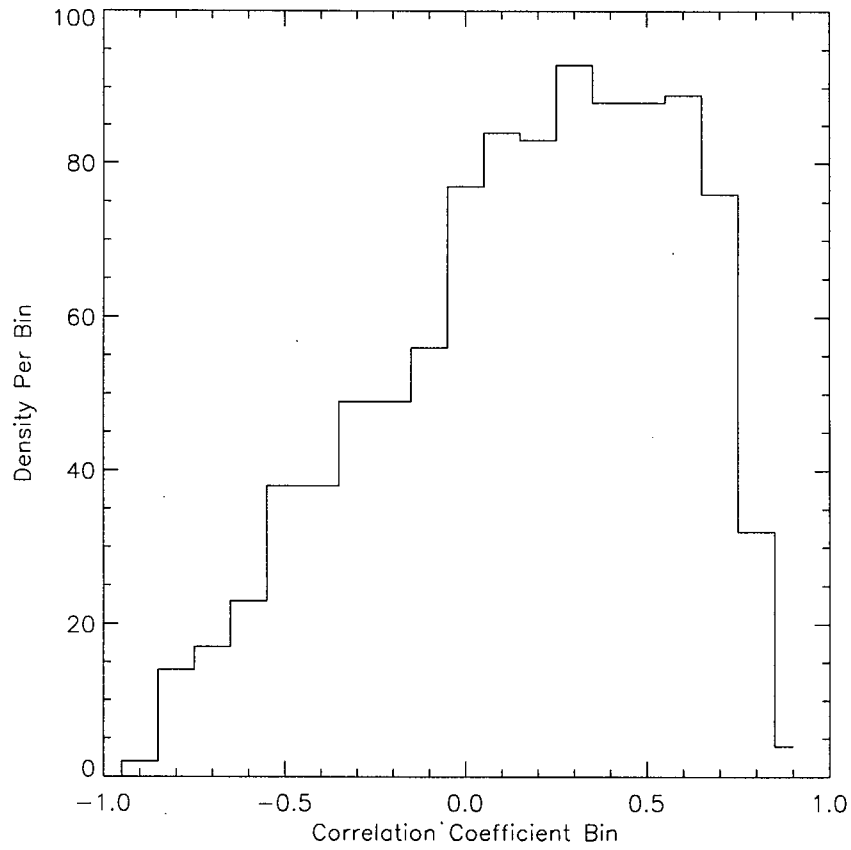


Figure 4.10: This plot shows the distribution of correlation coefficients obtained from $450\ \mu\text{m}$ stacked fluxes versus redshift for a set of Monte Carlo simulations of stacked $450\ \mu\text{m}$ flux in redshift bins of $\Delta z = 1$.

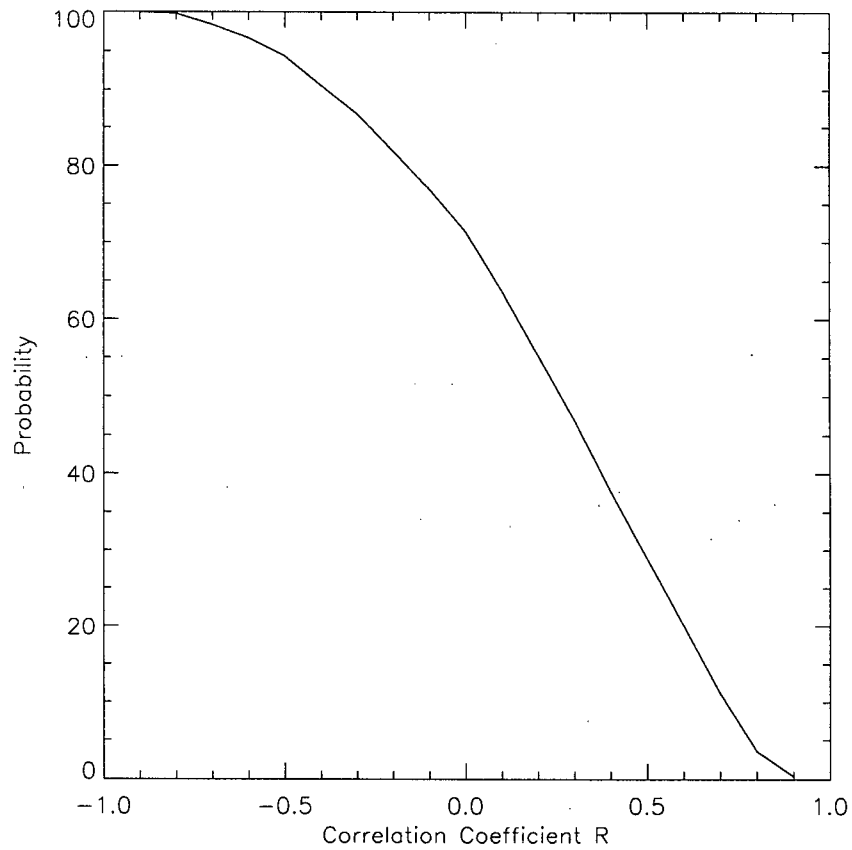


Figure 4.11: This plot shows how many times a correlation coefficient is obtained for the $450\ \mu\text{m}$ stacked fluxes versus redshift from a set of Monte Carlo simulations of stacked $450\ \mu\text{m}$ flux in redshift bins of $\Delta z = 1$.

in order to evaluate the likelihood of getting these correlation coefficients at random for both maps. Upon examination of the output of the simulations (see Figs. 4.15 and 4.17), obtaining a correlation coefficient of 0.40 or higher by chance occurs about 15 per cent of the time for the 850 μm map, and obtaining a coefficient of 0.43 or higher by chance occurs about 15 per cent of the time for the 450 μm map. These results seem more suggestive of a flux-redshift correlation, but we are not confident enough to reject the possibility that these correlation coefficients arose randomly. Therefore, we ascertain that the submillimetre flux we detect is not very well characterized by the photometric redshifts of the K' -band selected galaxies.

Using the table of IR positions, multi-colour magnitudes, and photometric redshift estimates, we investigate any other possible correlations of IR position with the flux at the corresponding position in our SCUBA map. We investigate possible correlations of stacked submillimetre flux with K' magnitude of an equal number of objects per bin (see Figs. 4.18 and 4.19). We get correlation coefficients of -0.08 (a null result) and -0.76 for 850 and 450 μm respectively. Fig. 4.18 shows no trend of increasing 850 μm flux with K' -band faintness. Fig. 4.19 does not show conclusive evidence for a connection between 450 μm flux and K' -band brightness but there is a slight hint that brighter K' -band objects have slightly higher (and more positive) 450 μm fluxes.

Finally, we investigate if there is any correlation of stacked submillimetre flux with absolute V magnitude (M_V) for different redshift cuts. We look to the V -band this time, as it is a measure of the absolute optical luminosity and galaxy mass if the galaxy is not too heavily enshrouded in dust, to see if there is a stronger submillimetre signal correlation with optically luminous objects. We use absolute magnitude because it removes the dimming effect of distance, resulting in a better representation of the power output of the galaxy. We calculate the absolute magnitude by using the well-known equation:

$$m_V - M_V = 5 \log D - 5, \quad (4.1)$$

where D is in parsecs. We note that since we do not know the shape of each galaxy's data was sampled and binned (see Figs. 4.12 and 4.13).

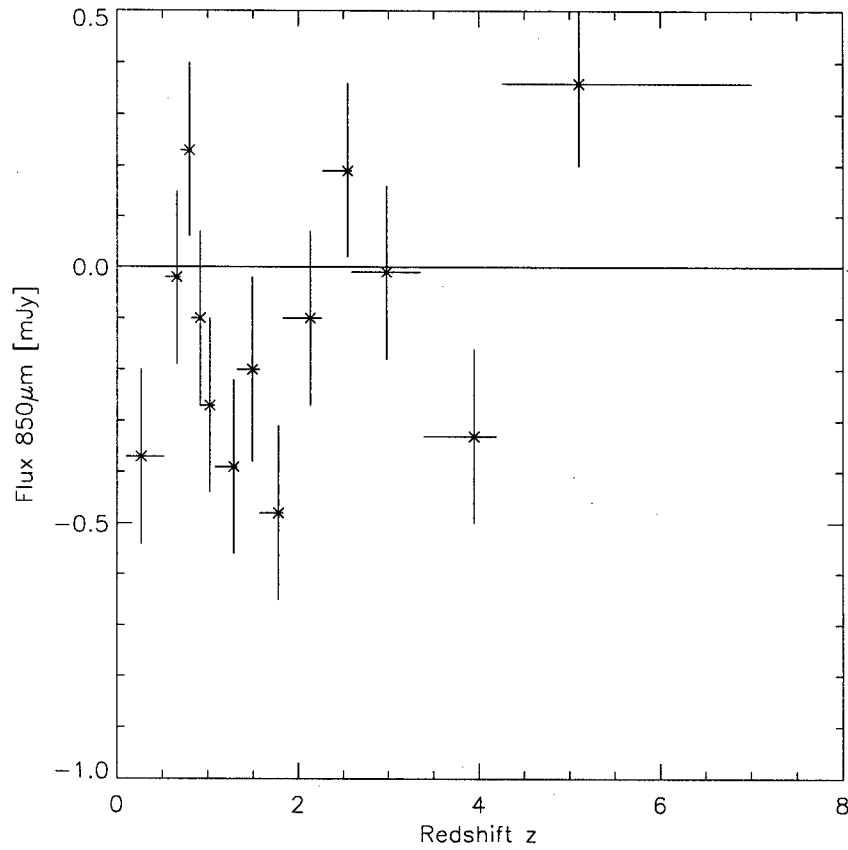


Figure 4.12: A plot of observed average $850 \mu\text{m}$ flux per redshift bin with an equal number of objects per bin. All bins contain 40 objects except for the last which contains 46 objects. The asterisks mark the mean redshift of each bin and the horizontal bars represent the extent of bin redshift coverage. The vertical error bars represent the flux errors in each redshift bin. A horizontal line through (0,0) is drawn to guide the eye to easily distinguish the number of redshift bins above and below a flux level of 0 mJy.

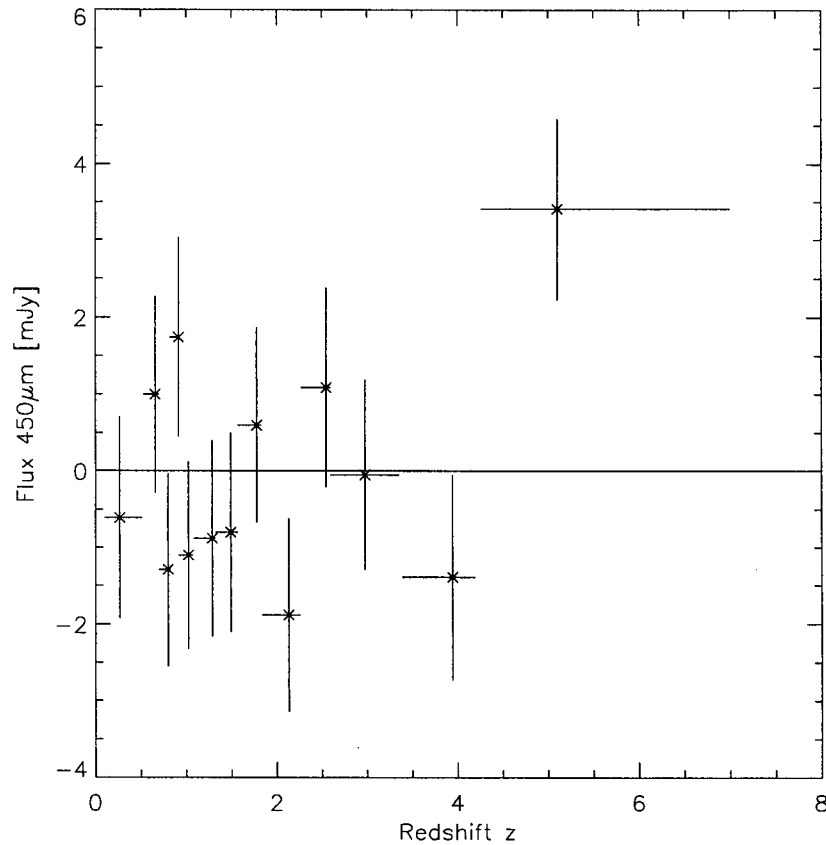


Figure 4.13: A plot of observed average $450 \mu\text{m}$ flux per redshift bin with an equal number of objects per bin. All bins contain 40 objects except for the last bin which contains 46 objects. The asterisks mark the mean redshift of each bin and the horizontal bars represent the extent of bin redshift coverage. The vertical error bars represent the flux errors in each redshift bin. A horizontal line through (0,0) is drawn to guide the eye to compare the number of redshift bins above and below a flux level of 0.

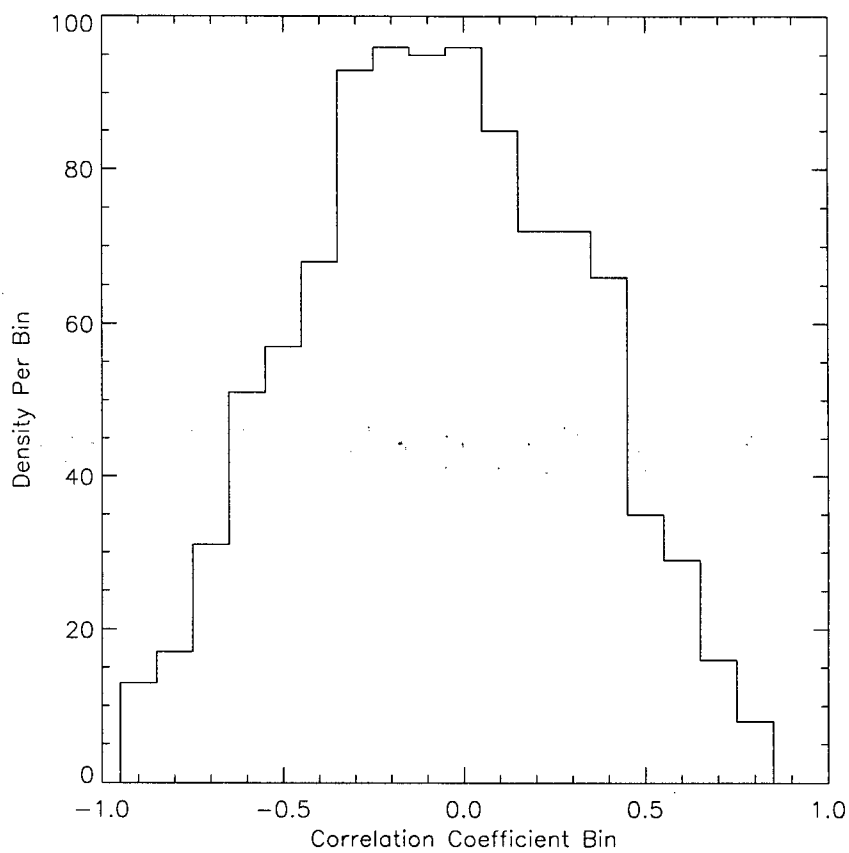


Figure 4.14: This plot shows the distribution of correlation coefficients obtained from $850\ \mu\text{m}$ stacked fluxes versus redshift for a set of Monte Carlo simulations of stacked $850\ \mu\text{m}$ flux with an equal number of objects per redshift bin.

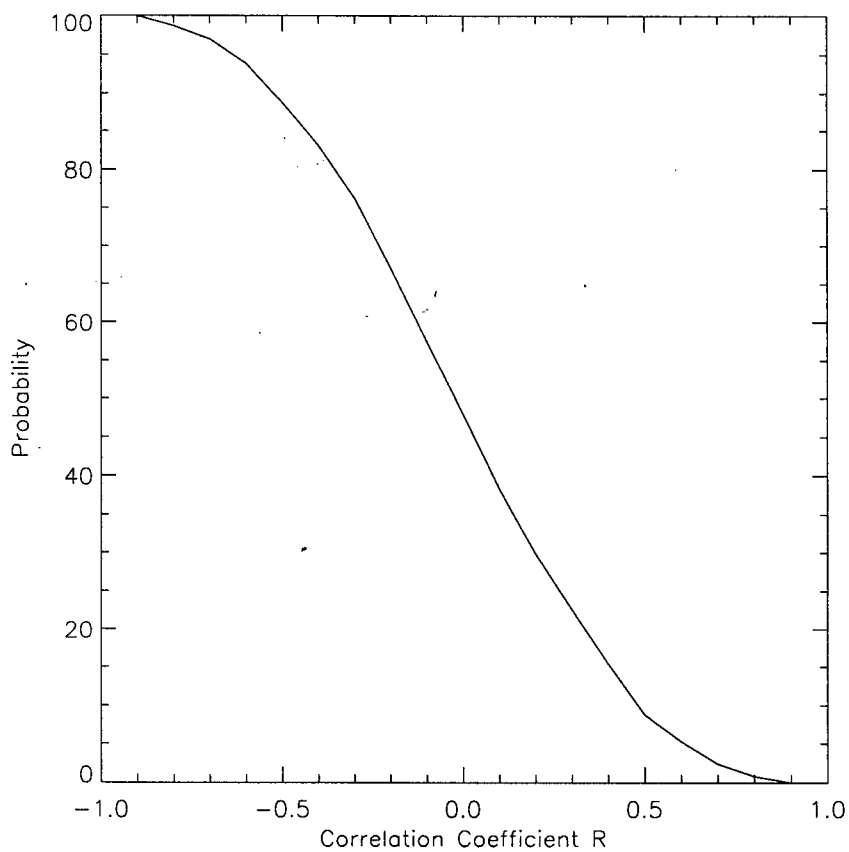


Figure 4.15: This plot shows how many times a correlation coefficient is obtained for the $850\ \mu\text{m}$ stacked fluxes versus redshift from a set of Monte Carlo simulations of stacked $850\ \mu\text{m}$ flux with an equal number of objects per redshift bin.

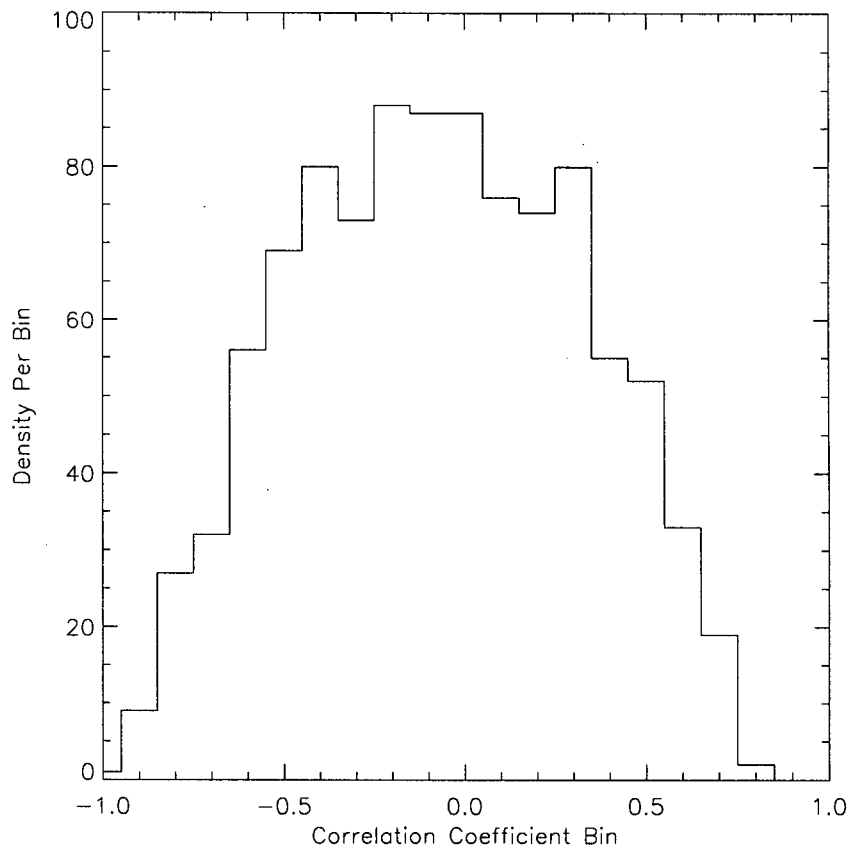


Figure 4.16: This plot shows the distribution of correlation coefficients obtained from $450\ \mu\text{m}$ stacked fluxes versus redshift for a set of Monte Carlo simulations of stacked $450\ \mu\text{m}$ flux with an equal number of objects per redshift bin.

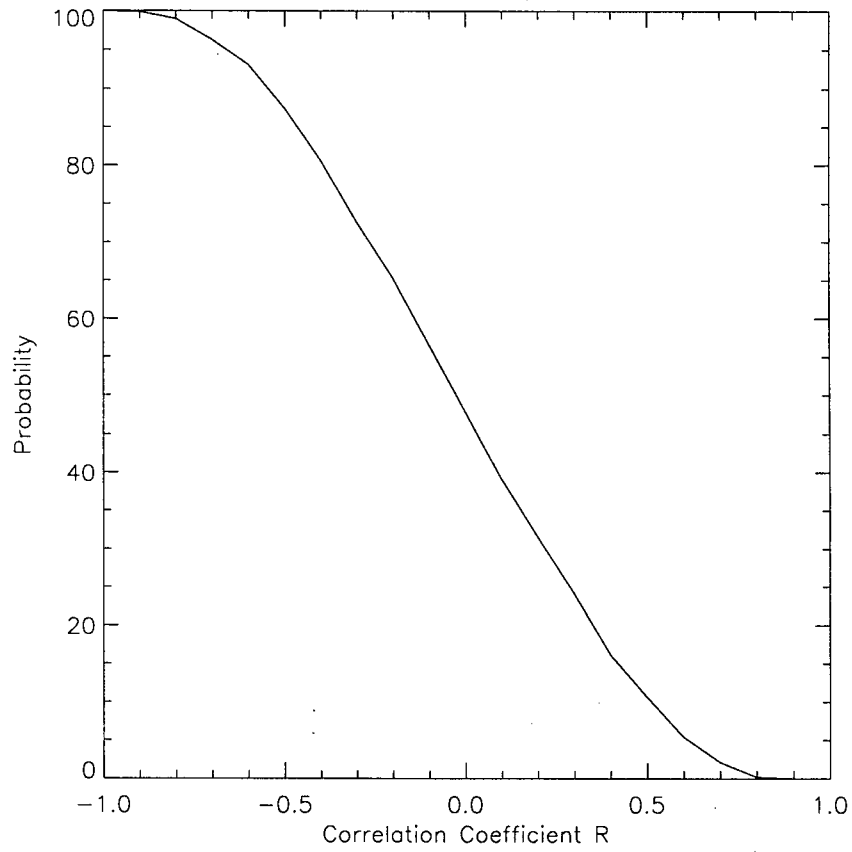


Figure 4.17: This plot shows how many times a correlation coefficient is obtained for the $450\ \mu\text{m}$ stacked fluxes versus redshift from a set of Monte Carlo simulations of stacked $450\ \mu\text{m}$ flux in bins with an equal number of objects per redshift bin.

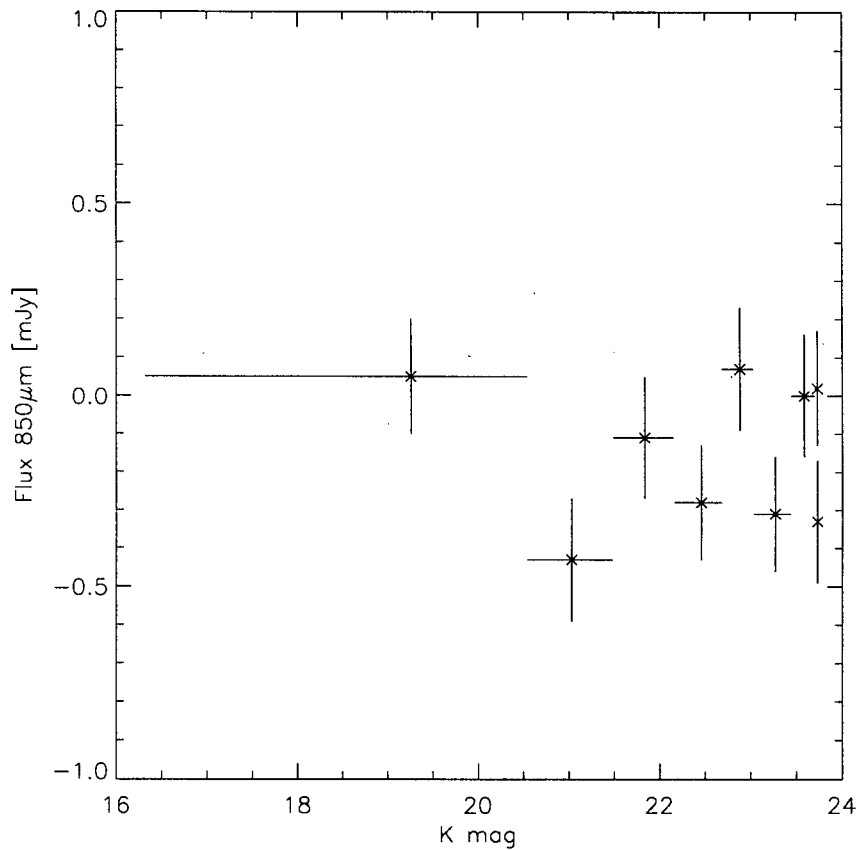


Figure 4.18: This is a plot of stacked $850\ \mu\text{m}$ flux measured in K magnitude bins containing 48 objects each (except for the last bin which contains 49 objects). The asterisks mark the mean K magnitude value of each bin and the horizontal bars represent the extent of bin K magnitude coverage. The vertical error bars represent the flux errors in each K magnitude bin. The correlation coefficient of -0.08 suggests a null result.

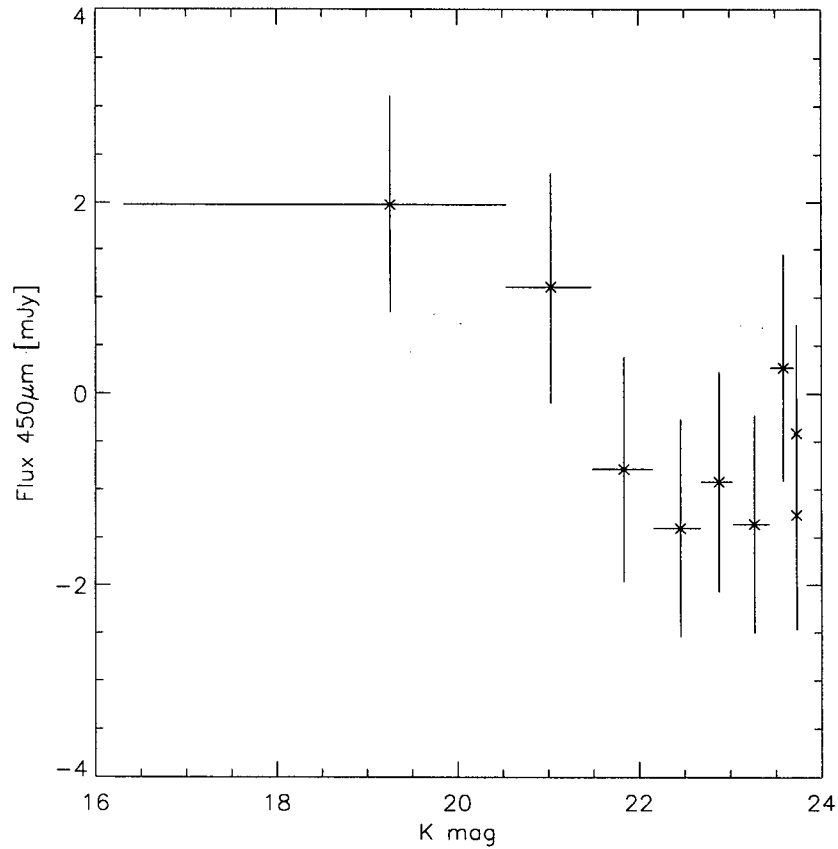


Figure 4.19: This is a plot of stacked $450\ \mu\text{m}$ flux measured in K magnitude bins containing 48 objects each (except for the last bin which contains 49 objects). The asterisks mark the mean K magnitude value of each bin and the horizontal bars represent the extent of bin K magnitude coverage. The vertical error bars represent the flux errors in each K magnitude bin. The correlation coefficient of -0.76 is slightly suggestive of a relation of increasing $450\ \mu\text{m}$ flux with brighter K magnitudes.

SED, we have not included a K-correction term that corrects for the effect of light in a wavelength band of interest being redshifted to longer wavelengths. This effect is obviously more pronounced at higher redshifts. We take D to be the luminosity distance, which can be easily found by using the redshift information. Fig. 4.20, shows a series of scatterplots of $850\ \mu\text{m}$ flux versus V -band absolute magnitude with different redshift cuts of $z > 0$ (all objects), $z > 2$, and $z > 4$. We notice that the mean $850\ \mu\text{m}$ flux does not vary with M_V , but this can be more clearly seen if we stack the submillimetre flux. The leftmost plots in Figs. 4.21 and 4.22 represent stacked $850\ \mu\text{m}$ flux for equal-size bins of M_V . These plots generally give null results, except for a hint of a correlation for objects with $z > 4$ of $850\ \mu\text{m}$ flux increasing with the faintness in M_V . This would be plausible considering that strong submillimetre detections are associated with a great deal of dust extinguishing the optical light. The rightmost plots in Figs. 4.21 and 4.22 represent stacked $850\ \mu\text{m}$ flux with an equal number of objects in each bin and all show no trends. We conclude that the lack of a strong trend of submillimetre flux with M_V indicates that the submillimetre emission in the SDF map is not well-described by the absolute V magnitudes of K' -band selected objects in the SDF.

4.1.1 Detections

We use Colin Borys' BS_FINDSOURCE program to pick out sources by fitting the point spread function (PSF) of the beam to each pixel on the map. Bright peaks in the convolved (i.e. smoothed) map are selected as "detected" sources when the PSF matches a source in the map (see Borys [6] for further details). We note detections of three $\text{SNR} > 3.0\sigma$ SCUBA sources at 450 and $850\ \mu\text{m}$ combined, but unfortunately they all lie outside of the region covered by this deep K' -band image (see Figs. 2.8 and 2.9 for the maps). Table 4.1 lists the detections in the 450 and $850\ \mu\text{m}$ maps. Using the source counts of $850\ \mu\text{m}$ submillimetre sources (c.f. Fig. 1.6), we expect to see ≈ 1 source detected at the 3.5σ level, given a map rms of $2\ \text{mJy}$. This estimate is consistent with the single 3.5σ detection we make. The number counts at $450\ \mu\text{m}$ are not as well known, however,

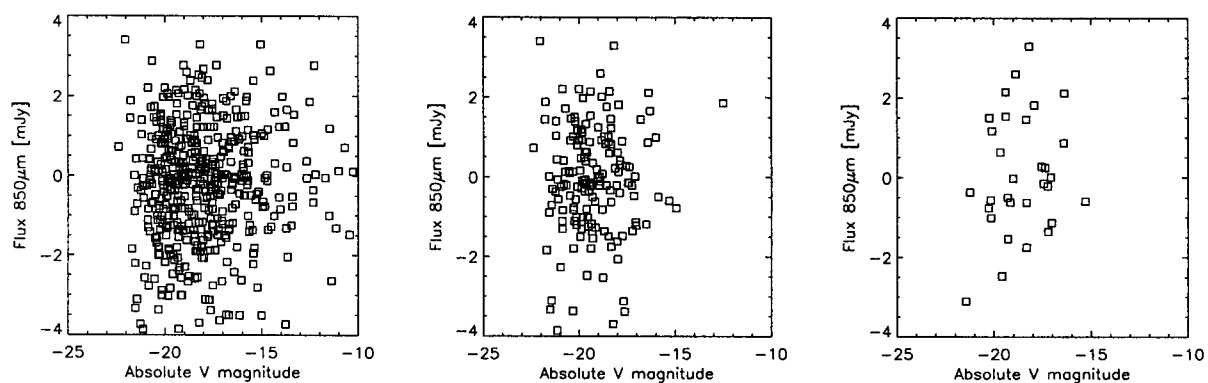


Figure 4.20: From left to right: these scatter-plots represent $850\ \mu\text{m}$ flux for every object detected in the V -band (488 objects total), for objects detected in the V -band with a photometric redshift higher than 2 (158 objects total), and for objects detected in the V -band with a photometric redshift higher than 4 (31 objects total).

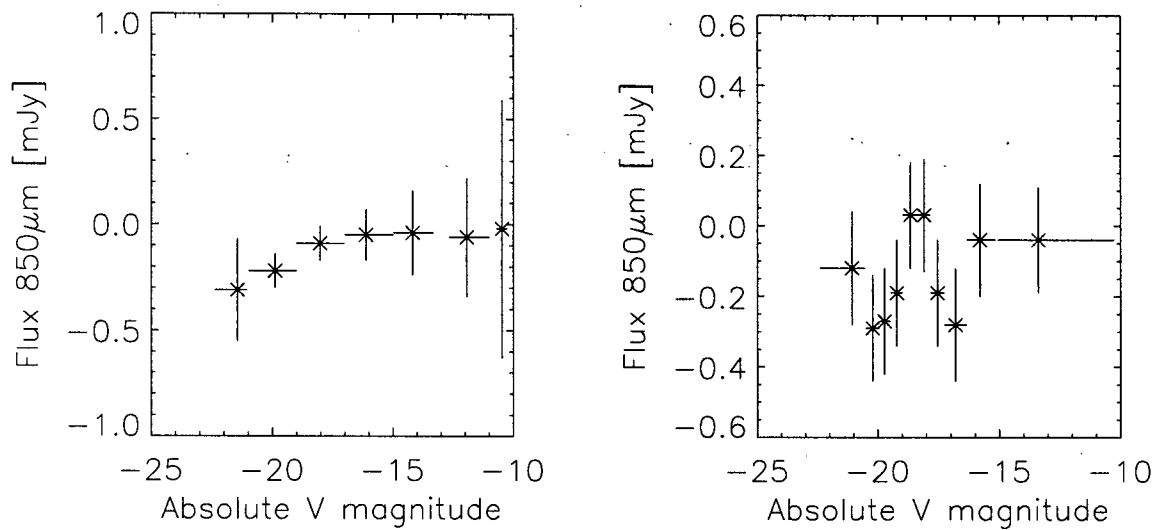


Figure 4.21: The leftmost plot represents stacked $850\ \mu\text{m}$ flux measured in M_V bins, two magnitudes in width, for all objects detected in the V -band (488 objects total). The rightmost plot represents $850\ \mu\text{m}$ flux measured in M_V bins, with an equal number of objects per bin (49), for all objects detected in the V -band. The horizontal bars represent the actual range of magnitudes in a bin and the vertical error bars show the standard deviation of the mean stacked flux in each bin.

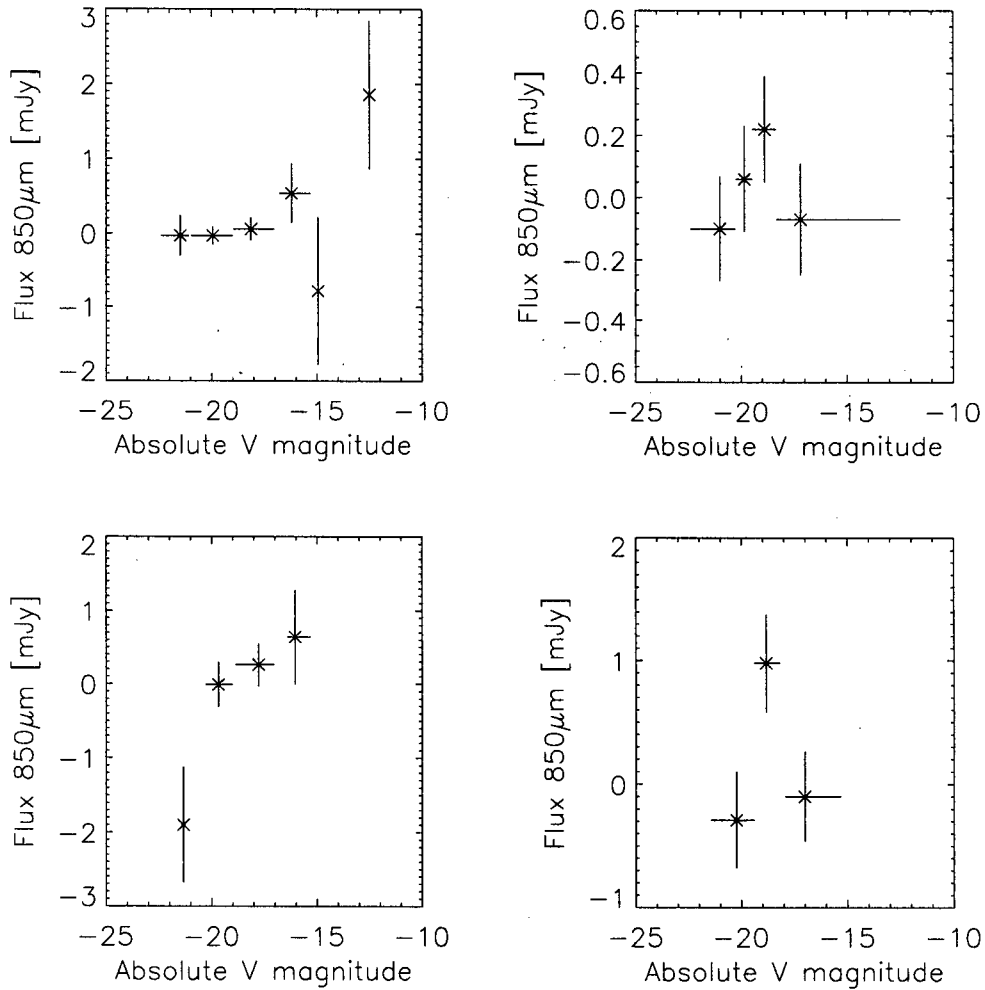


Figure 4.22: The leftmost plots represent stacked $850\ \mu\text{m}$ flux measured in M_V bins, two magnitudes in width, for all objects detected in the V -band with $z > 2$ (158 objects total) (top plot) and for all objects detected in the V -band with $z > 4$ (31 objects total) (bottom plot). The rightmost plots represent $850\ \mu\text{m}$ flux measured in M_V bins, with an equal number of objects per bin, for all objects detected in the V -band with $z > 2$ (40 objects per bin) (top plot) and for all objects detected in the V -band with $z > 4$ (10 objects per bin) (bottom plot). The horizontal bars represent the actual range of magnitudes in a bin and the vertical error bars show the standard deviation of the mean stacked flux in each bin.

and we make no attempt to estimate how many sources we expect to see at $450 \mu\text{m}$, given the depth of the map and the area surveyed.

ID	Position (2000.0)		Flux (mJy)	SNR
SDF 850.1	13 ^h 24 ^m 16 ^s 91	+27°29'46"01	$S_{850} = 4.40 (\pm 1.25)$	3.5σ
SDF 450.1	13 ^h 24 ^m 25 ^s 25	+27°30'37"01	$S_{450} = 75.45 (\pm 18.52)$	4.1σ
SDF 450.2	13 ^h 24 ^m 19 ^s 39	+27°30'37"01	$S_{450} = 50.29 (\pm 16.50)$	3.0σ

Table 4.1: The positions, fluxes and signal-to-noise ratios (SNR) of significant ($> 3 \sigma$) SCUBA detections in the SDF.

CHAPTER 5

CONCLUSIONS

We have mapped the 850 and 450 μm continuum emission of the Subaru Deep Field using SCUBA on the JCMT.

We found that the observed high $J - K'$ ($\approx 3 - 4$) sources produce an amount of SCUBA flux which is near to or below the $\simeq 1$ mJy confusion level, making their true flux difficult to estimate. The four HERO sources have an average 850 μm flux of 1.15 ± 0.46 mJy or a combined 95 per cent upper confidence limit of 1.76 mJy, a hint that they are dusty galaxies emitting a small amount of submillimetre flux.

Naively, the HEROs are most likely to be starburst galaxies based on their apparent irregular morphologies rather than compact regularly-shaped elliptical galaxies. Based on the assumption that HEROs are well-represented by an SED that fits Arp220, then they are at $z \leq 1.6$, consistent with known redshifts for SCUBA sources, but at the low redshift end¹. If we assume instead that the HEROs lie at average SCUBA redshifts ($z \approx 2 - 5$), then the typical elliptical galaxy model from Totani et al. [63] would also fit the data for at a redshift of $z = 2.3$.

Using an Arp220-like SED, we need to increase the brightness of the average HERO by a reasonable amount (about a factor of 1 – 1.5) and add a modest amount of dust (about 1 magnitude in J) in order to obtain an adequate fit. Thus, there is no reason to suspect that these objects are J -dropout galaxies at extraordinary redshifts. The HEROs are not well-represented by an NGC3938-like normal face-on spiral galaxy, given the flux constraints, since they would need to be brightened by about a factor of about 20 – 30,

¹At optical and near-IR wavelengths, deep images are crowded with galaxies with no more than a few percent of them lying at $z \gtrsim 3$ (see Guhathakurta, Tyson & Majewski [34]), as the galaxies do not benefit from the negative K-correction at near-IR wavelengths as they do in the submillimetre. We note that we may be only be picking up the low end of the redshift distribution by selecting objects in the K' -band.

a larger than acceptable amount for a galaxy of this nature.

Because the HEROs are faint in optical-IR-submillimetre wavebands with current instrument sensitivities, these objects may still play an important role in tracing the dust-enshrouded part of the early star formation picture. If the HEROs are dusty starbursts, as this work suggests, we see that the optically derived star formation rate (SFR) would be underestimated due to the presence of dust. Our strongest detection ($S_{850} = 2.15 \pm 0.92$ mJy, is the most convincing case for the HEROs being dusty starbursts. However, they could well be a mixed class of objects. Even for this object, its K' -band morphology looks superficially to be a merging pair of galaxies with $z \leq 1.6$, as determined from the Arp220 starburst template, consistent with a hierarchical formation scenario, where galaxies are made over a long period of time through successive mergers or through accretion of clumps of matter. Barger et al. [2] find that most of the submillimetre extragalactic background is emitted by $1 < z < 3$ sources, so the peak of the starburst activity lies at moderate redshifts. If there are many HEROs of this type at these redshifts then this has serious implications for the SFR as a function of redshift, since we may be missing more than was previously thought.

Our measurements of the HEROs do not support the prediction that HEROs should be SCUBA-bright. SCUBA galaxies are very often identified with EROs and we have tested if the inverse statement also holds true. Our results clearly demonstrate that measuring the submillimetre flux of HEROs will not necessarily select very bright SCUBA sources. SCUBA galaxies may just comprise one sub-set of a more diverse population of EROs.

From Figs. 4.1 and 4.3, we infer that we are detecting a population of sources just below the confusion limit of the maps. We correlate the IR K' -band selected galaxy positions with 450 and 850 μm flux and find that there is no correlation at the sensitivity limit of our measurements of the SDF. We conclude that the submillimetre flux we detect in our data is not characterized by the K' -band selected IR galaxies or by their photometric redshifts, and is presenting a view of the Universe different from that of the IR SDF. Although there is no apparent correlation with the IR SDF galaxies, the SCUBA map could still potentially be correlated with UV, optical, X-ray or radio data.

5.1 Future Work

Future SCUBA observations could provide even deeper limits (down to an rms of ≈ 1 mJy), but will be constrained by the confusion limit ($\simeq 0.5$ mJy). Deep VLA observations would allow us to obtain further redshift constraints through the well known radio/far-IR correlation ² (see Chapman et al. [13]). ALMA (submm), SIRTF and JWST (IR) will have the required sensitivities to detect these faint objects and possibly reveal their nature and redshifts with wide-band spectroscopy instruments. If the HEROs are at $z \leq 1.6$ then they should be detectable by BLAST (Balloon-borne Large Aperture Submillimetre Telescope) or with SCUBA at $450 \mu\text{m}$ in very good dry weather. Those data, in addition to CSO/SHARC-II $350 \mu\text{m}$ observations, could help to better constrain the assumed shape of the SED, thereby providing tighter constraints on the inferred redshift. A more complete study might include the use of a wider range of SEDs, rather than just the two templates that were employed here. In addition, without spectroscopic redshifts, substantial progress may also require model SEDs with a proper treatment of the dust at the same time as the stellar population evolution.

²The underlying power causing the emission originates from the same short-lived massive stars

BIBLIOGRAPHY

- [1] Archibald E.N., Wagg J.W., Jenness T., 2000, Calculating Sky Opacities: a re-analysis for SCUBA data, SCD system Note 2.2
- [2] Barger A.J., Cowie L.L., Smail I., Ivison R.J., Blain A.W., Kneib J.-P., 1999, AJ, 117, 2656
- [3] Blain A.W., Smail I., Ivison R.J., Kneib J.-P., Frayer D.T., 2002, preprint (astro-ph/0202228)
- [4] Blain A.W., Barnard V.E., Chapman S.C., 2003, MNRAS, 338, 733
- [5] Bolzonella, M.J., Miralles, M., Pello, R., 2000, A&A, 363, 476
- [6] Borys C., 2002, PhD. thesis, Univ. of British Columbia
- [7] Borys C., Chapman S.C., Halpern M., Scott D., 2000, preprint (astro-ph/0009143)
- [8] Borys C., Chapman S.C., Halpern M., Scott D., 2002, MNRAS, 330, L63
- [9] Calzetti D., Kinney A.L., Storchi-Bergmann T., 1994, ApJ, 429, 582
- [10] Cardelli J.A., Clayton G.C., Mathis J.S., 1989, ApJ, 345, 245
- [11] Carroll S.M., Press W.H., Turner E.L., 1992, ARA&A, 30, 499
- [12] Chapman S.C. et al., 2000, MNRAS, 319, 318
- [13] Chapman S.C., Lewis G.E., Scott D., Borys C., Richards E., 2002, ApJ, 570, 557
- [14] Chapman S.C., Scott D., Borys C., Fahlman G.G., 2002, MNRAS, 330, 92
- [15] Condon J.J., 1974, ApJ, 188, 279

- [16] Davis M., Efstathiou G., Frenk C.S., White S.D.M., 1985, ApJ, 292, 371
- [17] Dey A., Graham J.R., Ivison R.J., 1999, ApJ, 519, 610
- [18] Dickinson M.E. et al., 2000, ApJ, 531, 624
- [19] Dole H., 2000, PhD. thesis, Univ. of Paris-Sud XI, Orsay
- [20] Dole H. et al., 2001, A&A, 372, 364
- [21] Downes D. et al., 1999, A&A, 347, 809
- [22] Downes A.J.B., Peacock J.A., Savage A., Carrie D.R., 1986, MNRAS, 218, 31
- [23] Dunlop J.S., 2001, NewAR, 45, 609
- [24] Dunlop J.S. et al., 2002, preprint (astro-ph/0205480)
- [25] Dunne L., Eales S., Ivison R., Morgan H., Edmunds M., 2003, Nat, 424, 285
- [26] Eales S., Lilly S., Webb T., Dunne L., Gear W., Clements D., Yun M., 2000, AJ, 120, 2244
- [27] Eggen O.J., Lynden-Bell D., Sandage A.R., 1962, ApJ, 136, 748
- [28] Elbaz D., Flores H., Chantal P., Mirabel I.F., Sanders D., Duc P.-A., Cesarsky C.J., Aussel H., 2002, A&A, 381, L1
- [29] Ferguson H.C., Dickinson M., Williams R., 2000, ARA&A, 38, 667
- [30] Franceschini A., 2000, preprint (astro-ph/0009121)
- [31] Frayer D.T., Smail I., Ivison R.J., Scoville N.Z., 2000, AJ, 120, 166
- [32] Gear W.K., Lilly S.J., Stevens J.A., Clements D.L., Webb T.M., Eales S.A., Dunne L., 2000, MNRAS, 316, L51
- [33] Gispert R., Lagache G., Puget J.-L., 2000, A&A, 360, 1

- [34] Guhathakurta P., Tyson J.A., Majewski S.R., 1990, ApJ, 357, L9
- [35] Hildebrand R.H., 1983, QJRAS, 24, 267
- [36] Holland W.S. et al., 1999, MNRAS, 303, 659
- [37] Hu E.M., Ridgway S.E., 1994, AJ, 107, 1303
- [38] Hughes D.H. et al., 1998, Nat, 394, 241
- [39] Ibata R.A., Gilmore G., Irwin M.J., 1994, Nat, 370, 194
- [40] Jenness T., Lightfoot J.F., 1998, Starlink User Note 216, Starlink Project, CLRC
- [41] Jenness T., Stevens J.A., Archibald E.N., Economou F., Jessop N.E., Robson E.I., 2002, MNRAS, 336, 14
- [42] Johnstone D., Wilson C.D., Moriarty-Schieven G., Giannakopoulou-Creighton J., Gregersen E., 2000, ApJS, 131, 505
- [43] Kashikawa N., et al., 2003, AJ, 125, 53
- [44] Kauffmann G., 1996, MNRAS, 281, 487
- [45] Lagache G., Dole H., Puget J.-L., 2002, MNRAS, in press
- [46] Maihara T. et al., 2001, PASJ, 53, 25
- [47] O'Donnell J.E., 1994, ApJ, 422, 1580
- [48] Peacock J.A. et al., 2000, MNRAS, 318, 535
- [49] Rowan-Robinson M., 2001, ApJ, 549, 745
- [50] Sajina A., 2002, MSc. thesis, Univ. of British Columbia
- [51] Sanders D.B., Ap&SS, 266, 331
- [52] Sanders D.B., Mirabel F., 1996, ARA&A, 34, 749

- [53] Schlegel D.J., Finkbeiner D.P., Davis M., 1998, *ApJ*, 500, 525
- [54] Searle L., Zinn R., 1978, *ApJ*, 225, 357
- [55] Scott D. et al., *The Promise of the Herschel Space Observatory*. Eds. Philbratt G.L., Cernicharo J., Heras A.M., Prusti T., Harris R., 2001, *ESA-SP*, 460, 305
- [56] Scott S.E. et al., 2002, *MNRAS*, 331, 817
- [57] Skinner C.J., 1996, *Instrument Science Report NICMOS-014*
- [58] Smail I., Ivison R.J., Kneib J.-P., Cowie L.L., Blain A.W., Barger A.J., Owen F.N., Morrison G., 1999, *MNRAS*, 308, 1061
- [59] Smail I., Ivison R.J., Blain A.W., Kneib J.-P., 2002, *MNRAS*, 331, 495
- [60] Steidel C.C., 1999, *Proc. Natl. Acad. Sci. USA*, 96, 4232
- [61] Takeuchi T.T., Hirashita H., Ishii T.T., Hunt L.K., Ferrara A., 2003, *MNRAS*, 343, 839
- [62] Totani T., Takeuchi T.T., 2002, *ApJ*, 570, 470
- [63] Totani T., Yoshii Y., Iwamuro F., Maihara T., Motohara K., 2001, *ApJ*, 558, L87
- [64] Trentham N., Kormendy J., Sanders D.B., 1999, *AJ*, 117, 2152
- [65] Webb T.M.A., Lilly S.J., Clements D.L., Eales S., Yun M., Brodwin M., Dunne L., Gear W.K., 2003, preprint (astro-ph/0308439)
- [66] White S.D.M., Frenk C.S., 1991, *ApJ*, 379, 52
- [67] Wright E.L., Hinshaw G., Bennett C.L., 1996, *ApJ*, 458, L53
- [68] Yahata N., Lanzetta K.M., Chen H.-W., Fernandez-Soto A., Pascarella S.M., Yahil A., Puetter R.C., 2000, *ApJ*, 538, 493
- [69] Zheng Z., Wu H., Mao S., Xia X.-Y., Deng Z.-G., Zou Z.-L., 1999, *A&A*, 349, 737